The physics of droplet impact onto suspended and surface-attached metallic meshes: liquid penetration and spreading

Cristina Boscariol

A thesis submitted in partial fulfilment of the requirements of the University of Brighton for the degree of Doctor of Philosophy

2018

Abstract

The interaction between drops and porous matter has important applications in many fields such as painting, paper coating, filtration and biology, the latter considering for example reconstructive surgery processes, when blood impregnation of scaffolds is a very critical issue. Since the phenomenon of drop spreading onto a porous surface is particularly complex, a first step in developing our understanding of the underlying physics consists in analysing impacts on 2D deterministic structures, such as metallic meshes. The experiments are reproduced using three different liquids: water, acetone and a solution of water and glycerol. The meshes pore dimension and wire diameter have a range of respectively 25-400 μm and 25-220 μm. A combination of different surface porosities and liquids physical properties is needed to study how the impact outcome is influenced.

The present work shows the cases of drop impacts onto meshes attached to a solid substrate and of drop impacts onto the same meshes but suspended without a substrate.

Three main outcomes were observed for both cases: deposition, partial imbibition and penetration. The penetration into suspended meshes leads to a spectacular multiple jetting below the mesh.

In the first configuration of the attached meshes, the squared meshes were bonded to a flat, solid plate made of stainless steel in order to reduce the effect given by air entrapment. For the suspended meshes, even if the vertical micro-movements of the mesh are reduced as much as possible using heavy steel rings, the effect of the layer displacement may influence the impact outcome. Hence, in order to evaluate such effect, different ring diameters are considered which offered smaller and larger unclamped area for the suspended mesh compared to the original case.

A higher amount of liquid penetration is linked to a higher velocity impact v_i, lower viscosity and a larger dimension of the pore size. An estimation of the liquid penetration is given in order to evaluate the impregnation properties of the meshes. For the case of attached meshes a map of the regimes is proposed introducing two dimensionless numbers.

Contents

Table of figures

The experiments shown in Fig. 59 and in Fig. 60 were done using the same initial parameters in terms of impact velocity, liquid properties and mesh pore dimension. Nevertheless, a different outcome was observed. In the first sequence (Fig. 59), the droplet, after the impact, remains completely above the surface after the spreading and the recoiling. In Fig. 60 it is possible to observe that during the recoiling, part of the liquid penetrates below the surface. The penetration is possible due to the

Acknowledgments

I wish to thank the department of Computing, Engineering and Mathematics at the University of Brighton.

My most sincere gratitude goes to all my supervisors:

Professor Marco Marengo, for all the patience, and good advice. He has been an excellent guide during my PhD and a precious mentor.

Professor Cyril Crua, for all the support he gave me, in particularly for my laboratory experience. I can say after three years I learned to be more careful doing my experiments, but the road is still long, it is like running a marathon.

Dr Dipak Sarker, for all his kindness and support in guiding me through a different subject, and for all the nice talks we had during these three years.

A special thank goes also to Professor Sanjeev Chandra, who has been a wonderful example of passionate and motivated scientist and also helped to make possible my experience in Toronto.

A special thank goes to my lifelong friends Claudia and Linda, that I know will be able to share with me any experiences. Wherever we will go they will fill the distance and will be by my side.

I want to thank all the people that made all my years in Brighton so great.

Thanks to Luca, who started this experience with me and now is like my PhD big brother. He was extremely good in dealing with all my anxiety, since the very first skype call we did, in which we barely know each other. I will always miss the little window between our desks.

Thanks to Marco B., who is the best friend and listener I could ever hope to meet. Thanks for supporting me every time and always helping me to see the things from another prospective.

Thanks to Flavia, because she made Brighton life even more perfect. Our friendship started with an exchange of very polite and formal messages, but I always knew she was the kind of person to whom I could have confessed any details of my life.

Thanks to my amazing office buddies, Luke (skinny), Dan and Paul. had so much fun with them, they helped me to find my smile in the most hopeless days.

Thanks to Quentin, my first internship student and amazing friend and supporter.

Thanks to Maria, Valeria, Fra, Daiana, Pietro, Marco P., Marco R., Eugenio, Christian, Filippo, Céline, Pierre, Emanuele, Matteo, Danny, Anna Lisa, Ileana, Giorgio and all the other people who are still in Brighton or spent a few months in Brighton. I have learned something from all of them.

Thanks to all the students from ISAT that had the chance to do an internship year, thanks to Clement and Frey with whom I'm sure I'll be in contact for a long time.

Thanks to Guillaume, to be able to be part of all my different worlds and be the bridge that put everything together. He gave a sense to all my confusions even when it was too hard to go on.

Declaration

I declare that the research contained in this thesis, unless otherwise formally indicated within the text, is the original wok o the author. The thesis has not been previously submitted to this or any other university for a degree and does not incorporate any material already submitted for a degree.

Signed 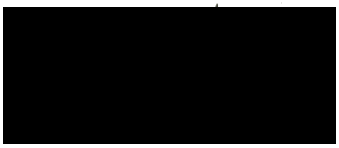

Dated Brighton 25/06/2019

1 Introduction

The aim of the research is analysing droplet impact on metallic porous meshes, to understand in which way the combination of different initial parameters can lead to a different outcome. This kind of surfaces find a main application in process like filtration but can also be linked to a medical application considering for example reconstructive surgery.

In the first part of the experiments, the meshes were carefully attached on a stainless-steel surface, to isolate the effect of porosity and roughness without taking in account the influence of elasticity and surface displacement.

In the second part of the experiments, a portion of the mesh was suspended to better quantify the impregnation properties of the surface and remark how it is influenced by mesh topology, liquid properties and impact velocity.

To generate droplets, needles of different sizes were used with liquids of different physical properties. Each experiment was recorded with a high-speed camera connected to a light source. The videos were consequently analysed to get critical information such as impact velocity and droplet diameter.

Summarising, the thesis aims to:

- Analyse the effect of porosity on droplet impact understanding in which way the outcome is influenced by the initial parameters.
- Obtain a map characterised by dimensionless numbers to separate the different regimes and predict the impact outcome.
- Estimate the impregnation properties of the mesh and point out if the air the elasticity, can influence the outcome.

1.1 Main application

The phenomenon concerning the behaviour and outcome of droplets impact can be linked to different applications in nature and industries [1][2][3].
By remarking the principal fields in which the phenomenon finds a function, we can list the following categories of physics and engineering:

- Physics of fluid and physics of chemistry
- Interfaces science
- Medical technology
- Processing of advanced materials

Droplets impact analysis can be also linked to fields concerning applications not directly connected to the engineering disciplines.

We can consider for example aerosol droplets, air conditioning mist, sun-spray, sunscreen and mosquito repellent product, pesticide crop spray, oil slick dispersal, cosmetic, industrial surface clinic formulas and drug inhalers. Depending on the kind of application, the outcome of droplets impact must be different to obtain a specific result.
For example, in the case of painting application, in which having a repeatable droplets generation is one of the most critical requirements [4], the main purpose is to transfer the ink from the stamp to the paper, so a stick outcome on the first surface would be negative for the transfer on the second surface. On the other hand, in case of agricultural applications, the goal is to obtain a stick outcome and avoid the dispersion of the droplets in the air However, problems arise since leaves are hydro-repellent to prevent bacterial colonization. By adding specific polymers (or a mixture of them) to agricultural products it is possible to partially avoid this situation. Another problem is that water can wash the agricultural product off the plants. To avoid this, a water insoluble gel is used, by adding hydroxide groups like Borate ions and titanium dioxides. The components are a polymer, a binding agent and a solvent that will evaporate after the deposition.

Because of the evaporation the concentration of the other two components will increase in time and allow the formation of a water insoluble gel.

By considering the case of a car windscreen, the desirable outcome is rebound. In this case one possible solution is to apply a hydro-repellent substance to the substrate like for example fluorinated alkyls lanes [5].

Referring again to an environmental application, A.C. Wright [6] developed a model to analyse the soil erosion phenomenon due to the dispersion of splash droplets. His model points out at many experimentally observed features which involved raindrops splash and aims at predicting the effect of slope, wind raindrops size and soil properties on the droplets dispersion. The main factor determining the degree and the direction of the splash droplet dispersion is the component of the raindrop velocity parallel to the surface of the slope. The model can predict the dispersion of soil particles by raindrop impact, which is the basis of a model of soil erosion by rain-splash.

Droplet impact has an important role also in the dynamics of filtration efficiency, where solid particles deposited inside a filter may affect the efficiency of liquid aerosol. There is also the influence of droplets deposition on filtration fibres inside the filter which can influence the efficiency of the solid particles removal [7].

Another interesting application is the 3-D printing process, which is a versatile digital manufactory technology used in several applications such as printing of flexible circuits, advanced electronic components, wax parts and metal parts. In this kind of application, to obtain a uniform metal traces the optimization of the printing step and ejection/deposition temperature is extremely important [8].

Droplet impact analysis can also be used to study phenomena in various fields, for example to model cancer invasion by considering an analogy between droplet and cancer cells diffusion on the tissue [9] or the spread of respiratory disease in which the cough of droplets concentration changes with the size into a peak rule [10][11].

2 Literature review

2.1 Basic concepts

Considering the importance of the droplet impact phenomenon, in the last years, various researches and studies were dedicated to define and analyse the influence of all the parameters that can affect the droplet behaviour. In fact, despite its apparent simplicity, the interaction between droplet and solid surface can lead to several fluidics processes that combine phenomena characterised by multiple temporal and spatial scales [5], [12],[13],[14].

The dynamic of droplet impact is very complex. Once a drop impacts on a surface, on the point of contact with the surface there will be an increase of the pressure. The impact energy is dissipated creating a new surface area and overcoming the viscous forces. Once the depletion of the energy is reached, the droplet will reach the maximum spreading diameter and will start to recoil. If the energy of the recoil is sufficient enough, the droplet may rebound from the surface and fall back again due to the gravity force [15].

The outcome of the droplet impact is influenced by the properties of the liquid, surface condition and kinematic parameters such as velocity and momentum [16][17][18]. For this reason, it is important to remark all the variables that characterise this kind of phenomenon:

Substrate characteristics → roughness, elasticity, porosity, wettability.

Liquid Characteristics → Newtonian liquid properties, non-Newtonian liquid properties.

Initial Parameter → impact velocity, droplet dimension, droplet shape.

2.1.1 Dimensionless numbers

The principal dimensionless numbers used to analyse the droplet impact are given by Reynolds number and Weber number

$$Re = \frac{\rho v_i d}{\mu} \qquad 2.1$$

$$We = \frac{\rho v_i^2 d}{\sigma} \qquad 2.2$$

where ρ, d, v_i are respectively liquid density, droplet initial diameter and droplet initial velocity and σ and μ are respectively liquid surface tension and viscosity.

The Reynolds number refers to the ratio between inertia and viscous dissipation and the Weber number remarks the importance of inertia forces against capillary forces. To take account of viscous dissipation we can refer to the Ohnesorge number, which combines the Reynolds and Weber numbers

$$Oh = \frac{\sqrt{We}}{Re} \qquad 2.3$$

Finally, the capillary number considers the reaction phase in which capillary forces play an important role

$$Ca = \frac{U_R \mu}{\sigma} = \frac{We}{Re} \qquad 2.4$$

where U_R is the retraction velocity of the lamella. If the initial kinetic energy of the droplet is high enough, the capillary force will be not sufficient to maintain the integrity of the droplet which will form smaller satellite droplets [5].

2.1.2 Spreading dynamics

Focusing on the physics of the spreading phenomenon, if the Reynolds and Weber numbers are high enough, the spreading droplet can be characterised by two different regions. During the first few milliseconds, the droplet makes contact with the substrate. It is forced to spread, forming a disc-shaped layer called lamella and a rim which appears due to capillary forces.

In the case of spreading and receding, the motion of the rim will be influenced by the wall friction and by the forces associated with wettability. The evolution of the spreading is strictly linked to the evolution of the rim [2]. Fig. 1 shows a schematic of the droplet spreading on a solid surface.

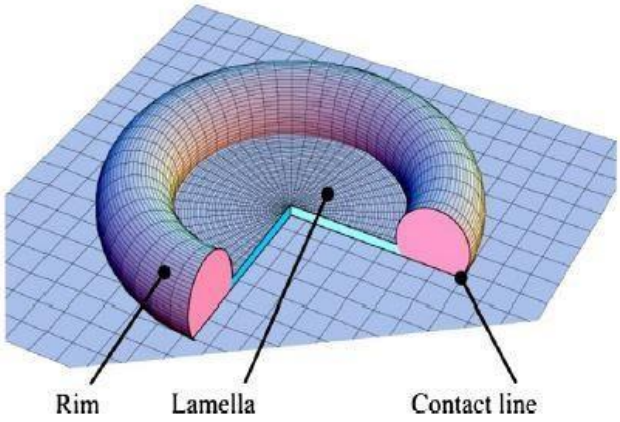

Fig. 1 Droplet spreading evolution [2]

As said the study of the spreading of liquid droplets during impact on a solid surface is extremely important for industrial applications such as spray coating, herbicide spraying and ink-jet printing in which the main outcomes parameters to control the process are wetting area and speed. Most studies of drop impact have focused on Newtonian fluids but also the impact of non-Newtonian fluid is receiving more and more attention considering there are several industrial applications [19][20].

The evolution of the spreading in time is analysed with two dimensionless numbers: the spread factor and the dimensionless time. The spread factor $d(t)^*$ is described by the ratio of the lamella diameter in time over the initial droplet diameter.

$$d(t)^* = \frac{d(t)}{d} \qquad 2.5$$

Where d (t) indicates the evolution of the droplet diameter in time, once that the droplet impacted on the surface. The dimensionless time is given by

$$t^* = \frac{tv_i}{d(t)} \qquad 2.6$$

where v_i is the impact velocity. The evolution of the droplet during the spreading can be divided in four phases: the kinematic phase, the spreading phase, the relaxation phase and the wetting/equilibrium phase. The maximum spreading diameter reached by the droplet is influenced not only by liquid properties such as viscosity μ and surface tension σ, but also by the impact velocity v_i A higher viscosity of the liquid will lead to a smaller maximum spreading diameter, whereas a higher impact velocity will lead to a larger maximum spreading diameter [5]. Fig. 2 shows a schematic of the spreading factor evolution in time.

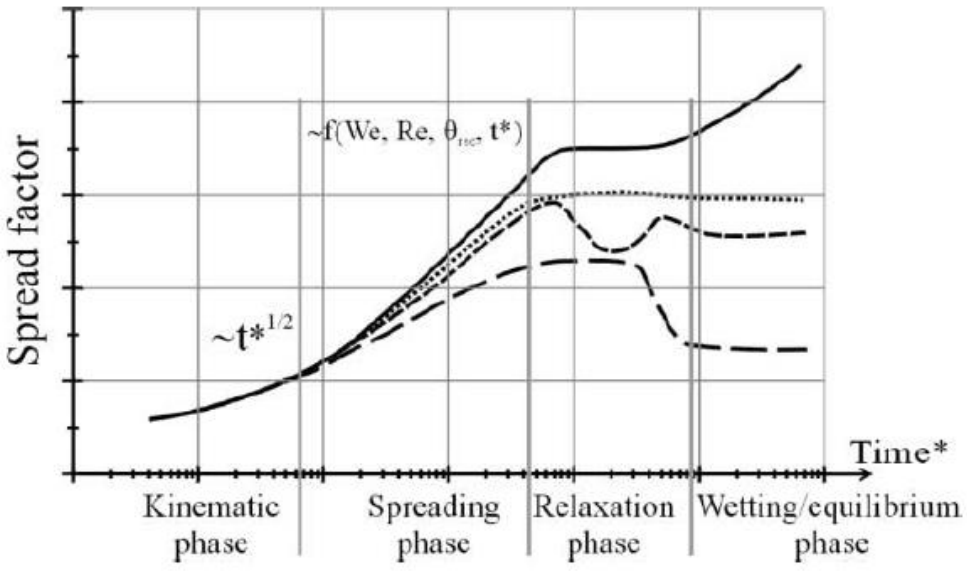

Fig. 2 Spread factor with time: Schematic representation of the spread factor with time. The different lines correspond to an arbitrary choice of possible spreading histories, depending on the parameters of the impact [21]

Lee at al. [22], observing the impact of water drops on oil infused nanostructured surfaces, investigated the effect of physical properties of the oil and impact velocity on the droplet dynamic. They found out that the low viscosity of the oil does not significantly affect the dimension of the spreading but affect the retraction dynamics. Most of the studies aim to estimate the maximal spreading diameter reached by droplet after the impact. Werner et al. [23] analysed the impact of 2.8 mm droplets containing maltodextrin DE5 at 20 and 40 wt% in water on a smooth anhydrous milkfat surface. They noticed that the greater maximum spread diameter is achieved with higher impact velocity and lower viscosity of the droplet. Fig. 3 shows the evolution of the spreading as a function of viscosity. They compared their results to the equation of Pasandideh-Fard et al.[24] which is given by

$$D_{max} = \frac{\sqrt{We+12}}{3(1-\cos\theta_a)+4(\frac{We}{\sqrt{Re}})} \qquad 2.7$$

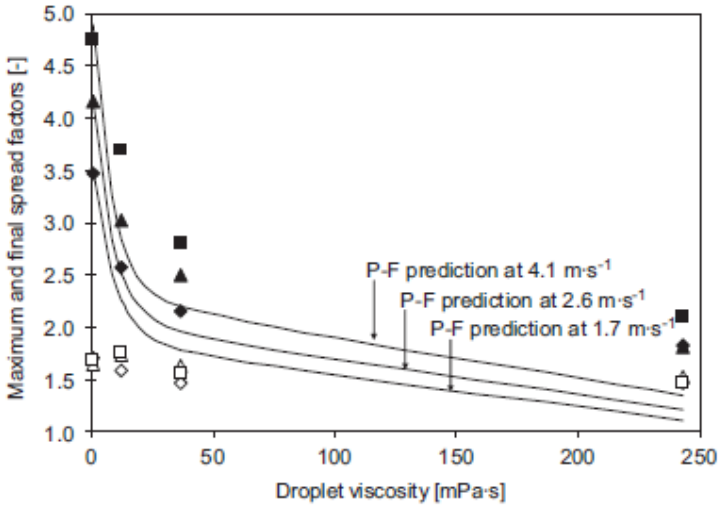

Fig. 3 Spread factor as a function of viscosity and impact velocity. The full symbols refer to the maximum spreading factor whereas the open symbols refer to the final spreading factor. The squares refer to $v_i = 4.1\frac{m}{s}$, the triangles to $v_i = 2.6\frac{m}{s}$ and the rhombus to $v_i = 1.7.\frac{m}{s}$. [23] The results are compared to Pasandideh-Fard et al. prediction [24]

Roux et al.[25] analysed the spreading of water on glass surfaces. They observed that at low impact velocity drops spread without being expelled liquid from the glass surface whereas at higher impact velocity part of the liquid is expelled. Fig. 4 shows the evolution of water impact on a glass surface.

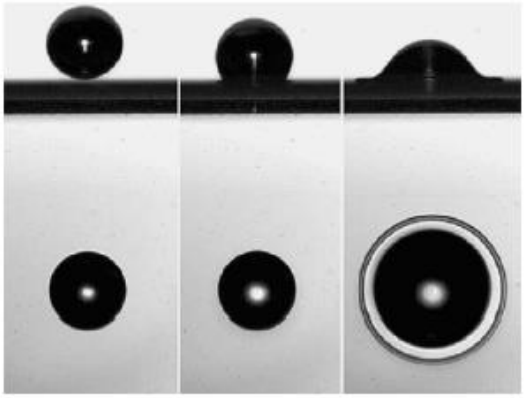

Fig. 4 Water impact on glass: $v_i = 1.56\frac{m}{s}$; d=1.198 mm, Re= 3740; We= 80 [25]

Toivakka [26], focused on the impact spreading of the droplet, considering mainly the influence of the kinetic energy. When a droplet impacts on a surface, its initial spherical shape is forced into a pancake-like form. The spreading ratio is determined by the balance of driving forces: the kinetic energy and resisting forces: viscosity and surface tension of the liquid. A larger contact angle will resist the spreading, on the opposite a smaller contact angle will promote it.

For large values of Weber number, the kinetic energy of the droplet is able to overcome the surface tension of the liquid and spreading takes place. For low values of Weber number, low impact velocity, the droplet tends to keep an almost spherical shape on the surface provided: no wetting takes place. Toivakka [26] analysed the evolution of the spreading parameter $\mathrm{d(t)}^* = \frac{\mathrm{d(t)}}{\mathrm{d}}$, by varying impact velocity and other parameters of interest, obtaining a correlation formula to predict the maximum spreading diameter given by

$$\mathrm{d_{max}} = 1 + 15.4\mathrm{We}^{0.5}\exp(-4.28\mathrm{We}^{0.072}\mathrm{Re}^{-0.043}) \qquad 2.8$$

2.1.3 Impact outcome on a dry surface

As mentioned previously the desired behaviour of droplet impingement greatly varies on the kind of application. For example, in the case of coating or painting and spray cooling, the entire mass of the droplet must remain attached to the surface. On the opposite for spray dryers and IC engine the droplet must rebound from the wall minimising any stick, in order to ensure a complete evaporation. An incomplete evaporation would result in a lower efficiency [27],[28]. The main outcome of droplet impact can be listed as follows:

- Rebound (full or partial): the droplet reaches the surface and is subjected to deformation, reaching a maximum diameter. During this process the kinetic energy is converted into surface energy. The deformation is followed by a contraction in which the droplet tends to return to its previous shape. The maximum extent to which a droplet spreads it is a crucial parameter to predict a rebound [29].

- Corona Splash: it mainly occurs for higher impact velocity and it takes place on a smooth surface. The secondary droplets are formed around the rim of a corona, remote from the solid surface. It is also characteristic in the case of droplet impact on a liquid film [29].

- Prompt splash: it takes place on a rough surface. The secondary droplets are generated at the beginning of the spreading phase. The difference from corona and prompt splash is given by the fact that in the case of prompt splash is not possible to observe a lamella detaching from the surface before secondary droplets are observed [30].

- Rolling: after the impact the drop rolls reducing the contact area [31].

- Deposition, stick: It consists of two phases, the kinematic stage and the actual deposition [32]. The droplet remains attached to the substrate and forms a film. The momentum is totally lost, and it is not possible to observe any break up.

- Break up/ Receding Break up: The impact allows the formation of smaller droplets that remain attached to the wall [29].

The splash output can be analysed by using the principle of energy conservation before and after impact, considering the energy dissipation due to the process.

$$E_k + E_p + E_s = E_{0k} + E_{0p} + E_{0s} + E_d \qquad 2.9$$

Where E_k, E_p, E_s and E_d are the kinetic, potential, surface and dissipated energies A combination of initial parameters will influence the final outcome. For example, a higher velocity on a rough surface will promote the prompt splash. A higher velocity will also lead to a larger spreading diameter. On the other hand a smaller initial droplet diameter will lead to a more probable deposition and a higher viscosity will reduce the probability of a break up. A lower surface tension will lead to a corona splash [30]. Fig. 5 shows some sequences of the main outcomes of the droplet impact.

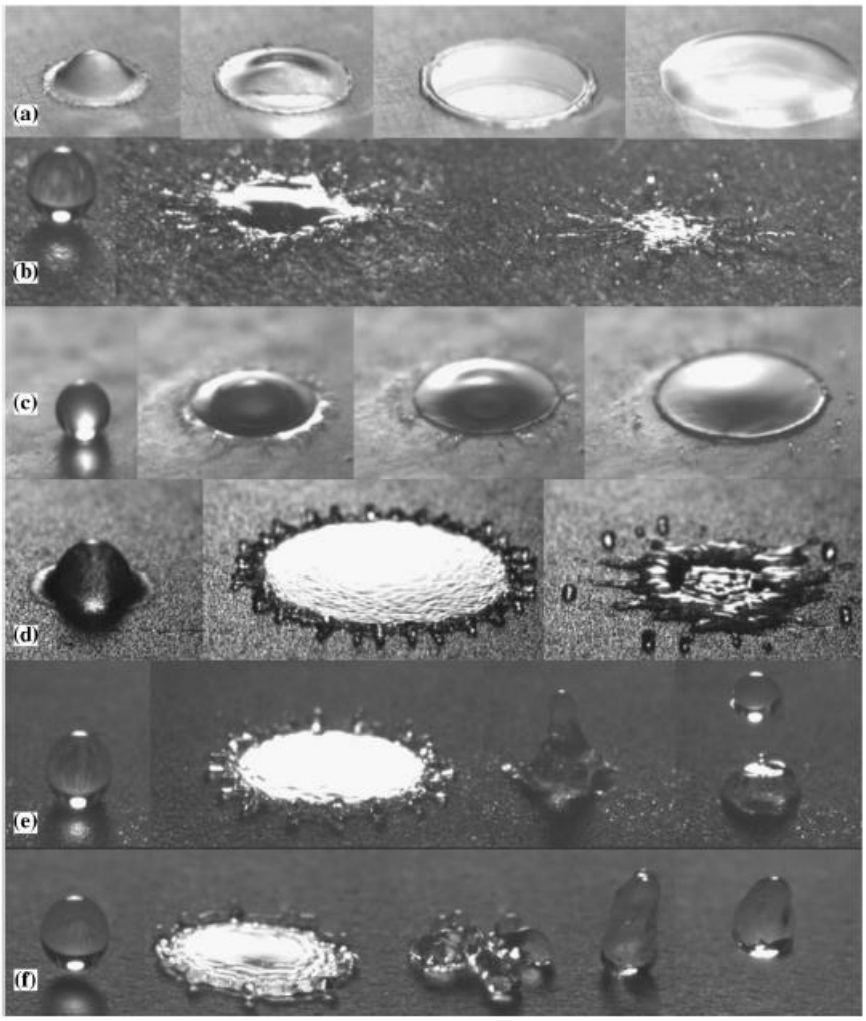

Fig. 5 Outcome of droplet impact (a) Deposition (b) Prompt Splash (c) Corona Splash (d) Recedeing Break up (d) Partial Rebound (e) Rebound [2]

2.1.4 Splash threshold

To define a splashing threshold Mundo et al. [16], conducted a study of liquid droplets impinging on a flat surface. They found out that the splashing occurs due to the decay of the cylindrical sheet ('corona'). The transition between the deposition outcome and the splash outcome is given by a number which is the combination of Re and We number that represent the fluid properties and kinematic impact parameter. The number is given by

$$k = We^{\frac{1}{2}} \cdot Re^{\frac{1}{4}} \qquad 2.10$$

Palacios et al. [33] conducted an experimental study onto a smooth, dry glass surfaces, to analyse the splash/deposition threshold, focusing on the influence of the Reynolds number. To measure the droplet diameter in case of a not spherical droplet, they defined an equivalent diameter

$$D_{eq} = (D_v D_h^2) \qquad 2.11$$

where v and h are referring to vertical and horizontal direction. Analysing the different results obtained for different parameters combination, they derived the following formula:

$$We_{crit} = 1.886Re^{0.637} + 1.068856Re^{-1.4} \qquad 2.12$$

where We_{crit} is the critical Weber number for which splashing occurs. They presented different correlations to fit their data (Fig. 6)

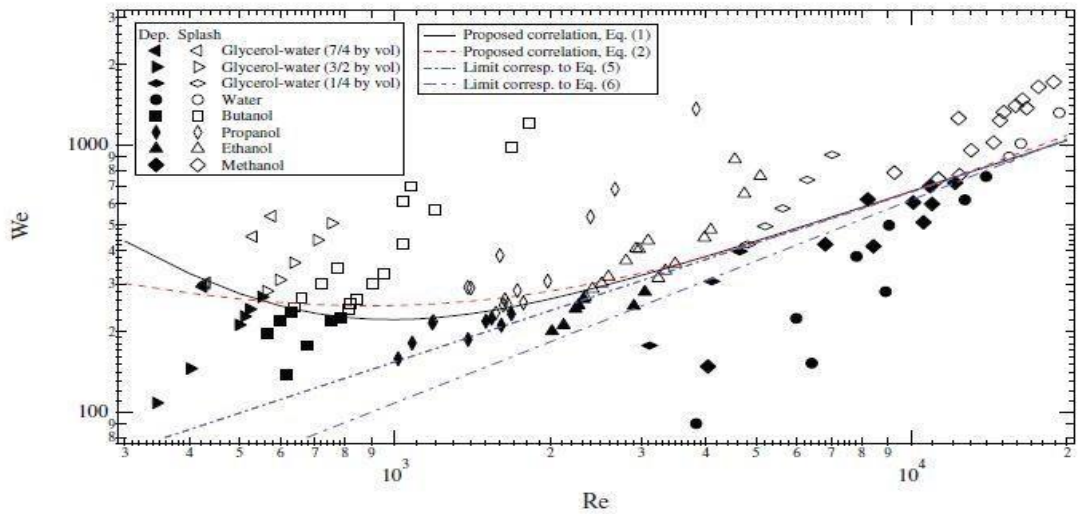

Fig. 6 Splash/deposition behaviour of drop of different liquids.

Eq. (1): $We_{crit} = 1.886Re^{0.637} + 1068856Re^{-1.40}$; Eq. (2):$We_{crit} = 0.566Re^{0.760} + 4484Re^{-0.5}$; Eq. (3): $Oh_{crit} = \frac{1.373}{Re^{0.681}}$; Eq. (4): $Oh_{crit} = \frac{0.752}{Re^{0.620}}$ [33]

Always focusing on the principal parameter to describe the splashing threshold, Gipperich et al. [34] analysed the splash threshold by varying surface properties

like roughness and porosity, using two different kind of liquids: water and isopropanol. The Porosity of a medium can be defined as the fraction of the volumes of voids, over the total volume. They observed the different output that can occur in the case of a structured substrate or an unstructured substrate by varying pores size and distribution. They characterised the roughness of the substrate by two different variables: R_z the maximum height of the profile and the standardized number of peaks RP_c. Consequently, the dimensionless parameter used to describe the splash output is given by $R_z \cdot RP_c$.

To define a splashing threshold, a specific Weber number is introduced:

$$\mathrm{We_s} = \frac{\rho \mathrm{D U_s^2}}{\sigma} \qquad 2.13$$

where $\mathrm{U_s}$ is the impact velocity for which splash occurs.

Consequently if

$We < Wes$ → No splash occurs

$We > We_s$ → Breakup of the lamella

Comparing the two fluids they noticed that the prompt splash threshold for rough surfaces of isopropanol falls in to the same range of distilled water and concluded that viscosity plays a minor role for the two fluids. In the case of porous surface, they obtained a different result. In fact, the distilled water splashing threshold is equal or higher for all investigated porous targets compared to the rough targets.

If We>200, the characteristics of the substrate and his wettability does not influence the phenomenon anymore and for higher value of We, the crown splash becomes more evident.

Roisman et al. [35] developed a model to describe the different regimes of splash thresholds by analysing substrate roughness and porosity. They concluded that it is not possible to find a boundary of the transition region between splash and deposition for the irregularity of the surface morphology. It is possible to delimit a region, near the splashing boundary, in which the splash probability varies from one to zero and distinguish two different areas:

- **Lower splash thresholds**: below which the probability of prompt splash is negligibly small.
- **Upper deposition thresholds**: above which the probability of deposition is negligibly small.

The lower splash threshold from the experimental data on the rough surfaces is given by

$$\mathrm{We}_{\mathrm{splash}} = 10.5\left(\frac{\mathrm{Rpk}}{\mathrm{Rsm}}\right)^{-0.7} \qquad 2.14$$

where Rpk is the average height of protruding peaks above roughness core profile and Rsm the mean width of a profile element. Fig. 7 reports the result they obtained for different kind of substrates.

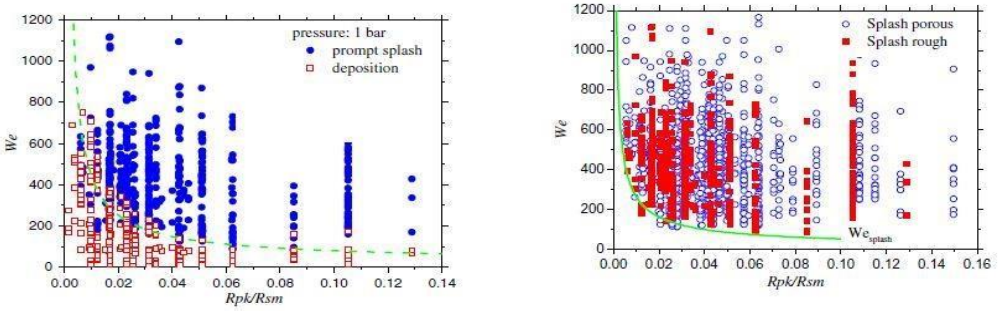

Fig. 7 Map of prompt splash for rough and porous surfaces [35]

Porosity does not influence too much the impact behaviour in the case of lower splash thresholds but influences the upper deposition limit because of the penetration of the drops inside the substrate, due to the presence of pores. In the case of a porous substrates, drops deposition without splash is more probable. Taking into account the effect of porosity, they defined a modified Reynolds number given by

$$\chi = \frac{\rho \mathrm{R_{pk}} \mathrm{v_i}}{\mu}\Phi \qquad 2.15$$

where Φ indicates the concentration of pores distribution on the substrate, it is given by:

$$\Phi = \frac{V_v}{V_T} \qquad 2.16$$

where V_V and V_T refer respectively to the fraction of the volume of void and the total volume of the media. This way, the upper deposition limit takes into account also the effect of porosity. Considering a porous substrate, due to the partial penetration of the liquid inside the pores, deposition without splash is more probable, this is why the curve of the upper deposition limit will be influenced as it is shown in **Fig.** 8. By fitting the experimental data shown in **Fig.** 8, they obtained the following equation to describe the upper deposition threshold:

$$\frac{We}{1+0.24\cdot\chi^{0.5}} = 29\left(\frac{Rpk}{Rsm}\right)^{-0.68} \qquad 2.17$$

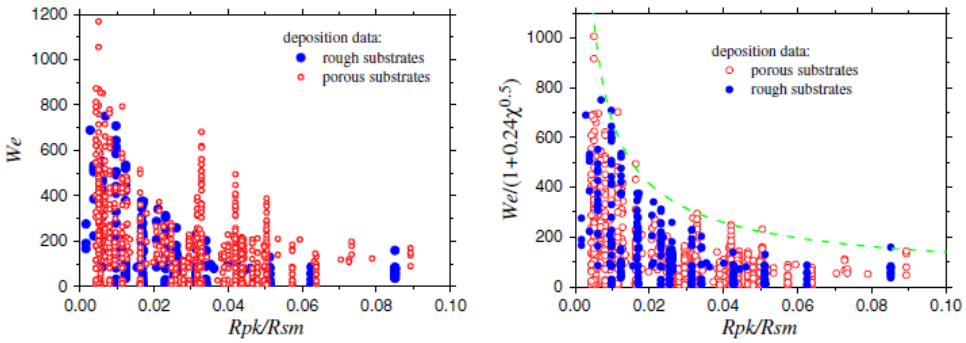

Fig. 8 Map of deposition on rough and porous substrates . Plot of the Weber number (left) and the empirical term $\frac{We}{1+0.24\cdot\chi^{0.5}} = 29\left(\frac{Rpk}{Rsm}\right)^{-0.68}$ (right) as a function of Rpk/Rsm. [35]

Fig. 9 shows the sequence of a droplet impact and penetration in a porous surface.

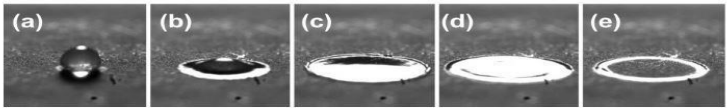

Fig. 9 Experiment sequence and results about droplet penetrating a porous medium. The sequence shows the droplet before the collision, the initial deformation, the spreading and the penetration into the target. [35]

2.1.4.1 Droplet impact on a wet surface

The impact of liquid drops on solid surfaces and films is an important and fundamental process in a large variety of natural and technical applications such as the erosion of soil, atomisation of liquids, atomisation of the fuel after a plane crash or surface cooling by water spraying in which case porous surface can enhance the cooling performance[36][37] [38].

Cossali et al [39] used a photographic technique to analyse the behaviour of a drop impacting on a liquid film to focus on corona evolution, depending on different parameters like viscosity, density, surface tension. By fitting the data, they found the following function to analyse the evolution of the second droplet diameter:

$$d_{sec} = a\left(bt^* + ct^{*-0.5}\right)^{0.5} \qquad 2.18$$

where a,b,c generally depends on Weber and Ohnesorge numbers and t^* is the dimensionless time. The greater the Weber number is, the smaller the diameter of the second droplets will be. The duration of the crown evolution depends on the thickness of the initial film and on the Ohnesorge number, whereas the dimension of the secondary droplets is not affected by film thickness. They compared their results regarding the velocity of the secondary droplet with the most used empirical models and observed that the model of Marengo and Tropea [37] gives the most similar prediction. Considering this model, the secondary droplet parameters are fitted in the following form:

$$\pi_k = (a + b\delta) + (c + d\delta)(K_r - K_0) \qquad 2.19$$

Where $k_r = \frac{K}{1000}$, $k_0 = \frac{K_{cr}}{1000}$ where the critical value of K, K_{cr}, between deposition and splash, depends on the roughness and film thickness δ and a, b, c, d which determine the secondary droplets parameters, are listed in Fig. 10.

	a	*b*	*c*	*d*
u*	0.056	0.057	0.038	0.000
v*	0.311	-0.077	-0.009	-0.024
d_{10}*	0.209	0.100	-0.096	0.005
d_{32}*	0.250	0.238	-0.022	-0.128

Fig. 10 Fitting coefficient for the empirical model of Marengo and Tropea. u* and v* are dimensionless velocities of the second droplets and d_{10}^*, d_{32}^* dimensionless mean diameters [37]

Fig. 11 shows a schematic of the increasing of secondary droplet diameter in time.

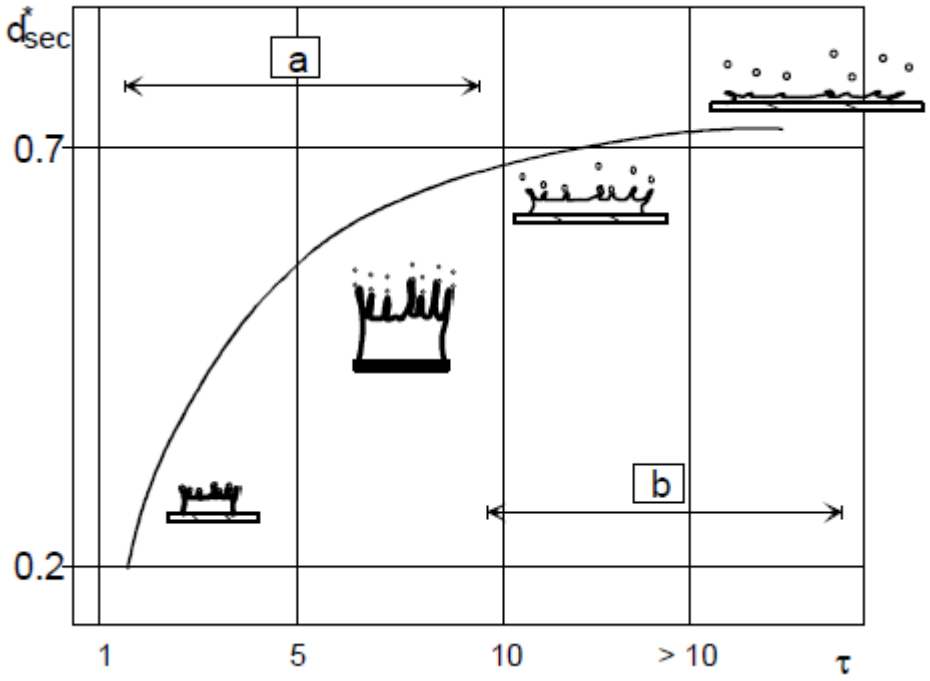

Fig. 11 Secondary droplet diameter evolution in time [39]

Cheng et al. [40] analysed the dynamics of oblique impacts of droplet on a solid wall covered by a thin liquid. They observed the evolution of drop shape after impact for different value of the angle of impact, θ and by varying the value of $u_{wall.}$ They adopted a numerical code based on a two phases flow lattice

Boltzmann model and observed that for $u_{wall} = 0$ and $\theta = 0$ splashing becomes asymmetric and the lamella bottom elliptical whereas for $u_{wall} > 0$ and $\theta = 0$ the splash is attenuated in the direction of the wall motion.

2.2 Surface characteristics and droplet-wall interaction

Depending on the application, some surfaces characteristic will be more desirable then others. In the specific a hydrophobic or hydrorepellent surface will enhance rebound outcome which is fundamental for application such as car windscreen, for example to remove the water due to heavy rainfalls. On the opposite, a hydrophilic surface will enhance the deposition.

2.2.1 Surface wettability

The wettability of a surface can be defined as the ability of the liquid to maintain contact with the solid surface. The characterization of the wettability of a material requires the measurement of the contact angle (CA) which plays a major role to point out the interaction between the droplet and the surface. The contact angle is defined as the angle formed between the free surface of a drop deposited on a given substrate and the substrate itself, which is determined by the thermodynamic equilibrium of the three phases: gas, liquid and solid. Fig. 12 shows a schematic of the contact angle.

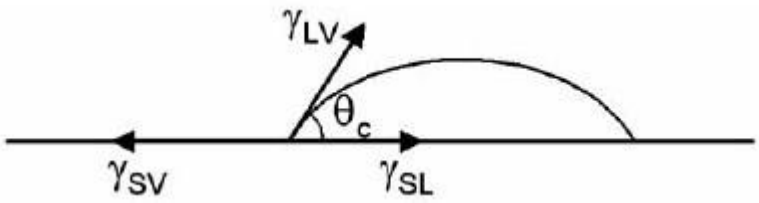

Fig. 12 Schematic of contact angle [5]

To estimate the value of the contact angle, it is important to consider the interaction between solid-liquid-gas that are gathered in the contact line. The surface properties influence deeply the drop shape and spreading rate.[41]

The contact angle can be calculated from the Young-Laplace equation given by

$$\sigma_{SV} = \sigma_{Sl} + \sigma_{LV}\cos(\theta_c) \qquad 2.20$$

where $\sigma_{SV}, \sigma_{SL}, \sigma_{LV}$ are respectively the solid-vapour, solid-liquid and liquid vapour interfacial energy. It is necessary to differentiate static CA and dynamic CA. In the specifics, given the time span of the considered physical phenomena, in the first case, the three phase contact line is moving (dynamic) in the second case is not (static).

If the surface is ideally homogeneous, the static CA is unique and reproducible[42], If the surface is nonideal, a hysteresis appears, characterised by an advancing and a receding contact angle, respectively θ_a and θ_r.

A possible method to determine this hysteresis for a static CA, is the sessile drop method. Practically, small amounts of liquid are injected into the sessile drop as slowly as possible while the contact line is not moving. The difference between the advancing contact angle and the receding contact angle defines the hysteresis (CAH). Repeated experiments on different locations of the solid surface provide a reliable measure of the wettability of the macroscopically apparently homogeneous surface [42].

For smaller contact angles, the liquid adhesion is stronger whereas a larger contact angle will lead to a weaker adhesion.

If the advancing contact angle is large and the hysteresis is small, the surface can be defined as hydrophobic[5]. The contact angle can be increased by higher: surface heterogeneity, surface roughness and liquid-substrate interaction. A very large advancing contact angle, $\theta_a > 150°$, and a hysteresis smaller than 10 °, lead to a superhydrophobic substrate [43] [44].

Numerical and experimental studies were done to observe the influence of CA and the CA hysteresis.

An interesting numerical study was developed by Malgarinos et al. [45] which introduced a novel numerical implementation for the adhesion of droplets impacting on a dry surface. Compared to previous model, the information of the dynamic contact angle is not given as a boundary condition but is derived because of the acting wetting forces at the droplet rim under dynamic conditions. The

model is valid mainly for lower Weber number for which capillary force influence the spreading dynamics.

Zhang et al. [46] focused on the impact of microscopic liquid droplets on solid surfaces considering a variety of surface characteristics using both molecular dynamics and lattice Boltzmann simulation techniques. By considering droplet impact on a surface with a cross-shaped region of one wettability superposed on a background with a different wettability value, they found out that spreading is quicker as wettability decreases. Consequently the final drops shapes is characterised by various indentations and protuberances and different degrees of spreading. This is due to the fact that different regions of the edge of a drop on a cross pattern have different contact angles, consequently the motion of the spreading droplet will no longer be radially symmetric.

2.2.2 Hydrophobic and hydrophilic surfaces.

The wettability of solid surface is governed by the chemical composition as well as the geometric structure of the surface. A material is hydrophilic when the intrinsic water contact angle (on its flat surface) is smaller than 90◦, and a material is hydrophobic when the intrinsic contact angle (CA) is greater than 90◦ [47] [48]. A hydrophobic substrate is defined as a surface capable to prevent the adhesion of the drops. The mobility of the liquid can be linked to the contact angle hysteresis which is influenced by the substrate characteristics. To fabricate super liquid-repellent layers, there are two necessary conditions: The surfaces must be of low energy and their microstructure has to be designed to lead to the entrapment of air [49]. For example, Xu et al. [48] fabricated a low surface energy superhydrophobic metallic mesh with a simple spray method by a reaction between metal salts and alkanethiols. They found out that the largest loading capacity appeared with meshes having pore size of $90\mu m$.

The introduction of surface roughness is mandatory to obtain a superhydrophobic surface. Two different superhydrophobic states may occur on a rough surface: Wenzel's state and Cassie's state. The first case is characterised by a high CA hysteresis, the water droplets pin the surface in a wet-contact mode. In the second case the water droplets have a non-wet contact mode on the solid surface and can

roll off easily due to the low adhesive fore. An example is given by Lotus leaves which are superhydrophobic surfaces with a high CA and very low CA hysteresis. Thanks to their properties, surfaces that could mimic the hydrorepellency of lotus leaves have been the topic of an intensive research due to the several number of applications such as self-cleaning or anti-sticking applications[50]. The Lotus case, is a special state of the super-hydrophobic Cassie state [51].

In some situations in which a transition occurs between the Wenzel and Cassie state the water droplets can slide when the surface is tilted at a certain angle. The CA hysteresis can be determined in this case as the sliding angle. Fig. 13 shows a schematic of Wenzel, Cassie and Lotus state.

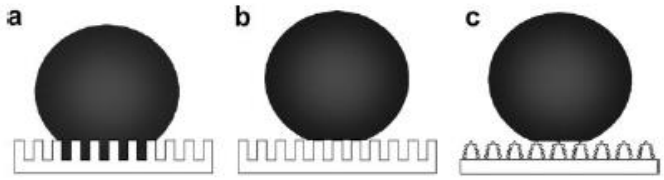

Fig. 13 (a) Wenzel state, (b) Cassie state, (c) Lotus state [51]

Summarising, a rough surface can be wet in one of two modes:

- Cassie state: the interface under the droplet is liquid-gas due to gas remaining beneath the drop in the troughs of the rough surface.
- Wenzel state: The entire solid surface under the drop is wetted by the drop. [52]

The work of Cassie, Cassie-Bexter allowed the definition of an equation that helps to describe the phenomenon of hydrophobicity on surfaces. There are many different references to the Cassie equation in the literature but in many cases, they lead to imprecisions. One of the most common formula is given by

$$cos\theta_c = f \cdot cos\,\theta - (1 - f) \qquad 2.21$$

Where f referred to the fractional projected area of a material with smooth surface contact angle θ, $(1 - f)$ indicates the contribution of remaining air under the

droplet and θ_c is the predicted Cassie Bexter contact angle. This equation can lead to several errors such as the interpretation and prediction of contact angle data on a surface and the transition criteria between Cassie and Wenzel state. The original equation is given by

$$cos\theta_c = f_1 \cdot cos\,\theta_1 - \mathrm{f}_2 \qquad 2.22$$

where f_1 is defined as material 1, the total area of solid under the drop per unit projected area under the drop, θ_1 is defined as the contact angle on a smooth surface of the material 1 and f_2 is defined in a similar way considering air as material 2 ($\theta_2 = 180°$).

Fig. 14 shows a schematic of three rough 2-D surfaces. In the schematic, material 1 (solid) is in blue, material 2 (air) is in white, and the liquid is the cross-hatched area above the surface. Liquid–vapor and solid–liquid interfaces of drop are denoted by the black line [52].

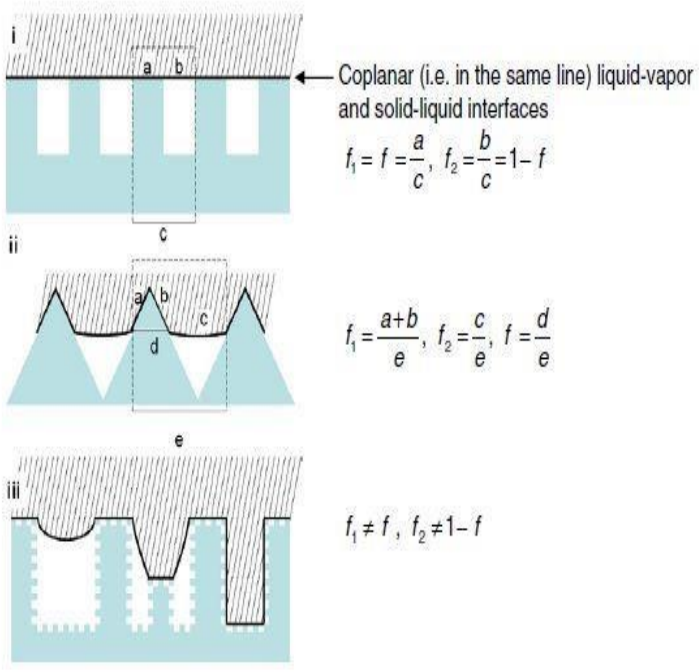

Fig. 14 Schematic of rough surfaces: (i)Smooth -topped rough surface, no penetration of the liquid occurs. This leads to $f_1 = f$ and $f_2 = (1 - f)$ (ii) arbitrary rough surface with $f_1 \neq f$; $f_2 \neq (1 - f)$(iii) dual scale rough surface [52]

Several studies were done to analyse the properties of superhydrophobic and superhydrophilic surface and their effect on droplet impact and spreading.

Tsai et al. [53] focused on the drop impact dynamics on superhydrophobic substrates. They compared drops impact onto super hydrophobic surfaces of controlled roughness and on CNF (carbon nanofiber). The CNF Carbon filaments were formed catalytically in metallic catalysts. They explored different roughness characteristics for different impact velocities (low and high Weber numbers). They observed that the impact evolution is similar in the case of small We for which a complete bouncing, partial rebouncing, trapping of an air bubble, jetting and sticky vibrating water balls occurs. Fig. 15 shows the results in the case of low Weber number. On the opposite, for large Weber number, a splashing outcome occurs, characterised by the formation of satellite droplets which are more pronounced in the case of the multiscale rough carbon nanofiber. Their results imply that the multiscale surface roughness at nanoscale plays a minor role in the impact events for We smaller than 120 but an important one for We larger than 120.

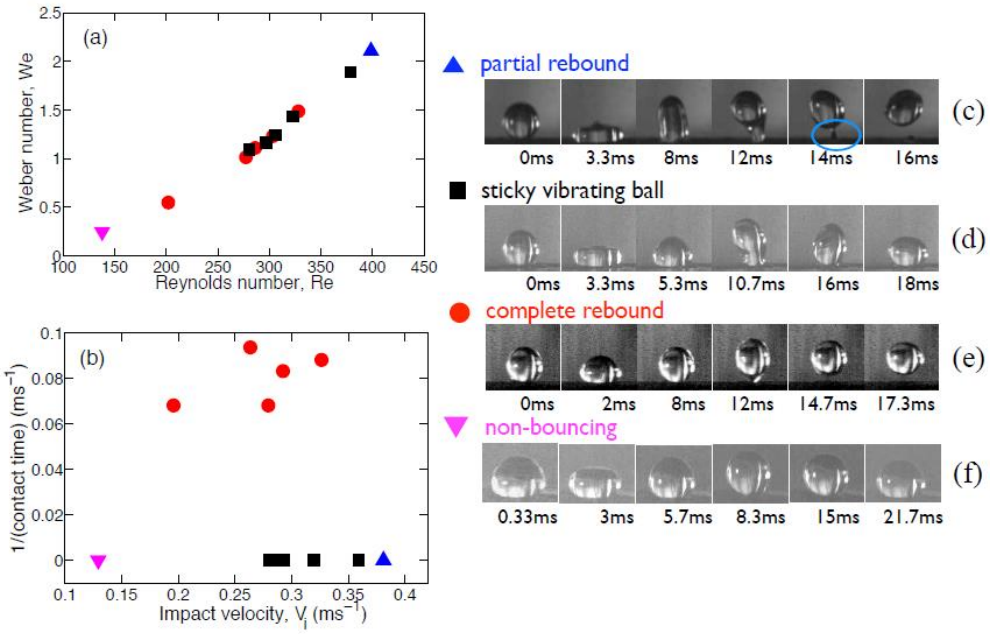

Fig. 15 Droplets impact on Carbon nanofiber substrate at low Weber number [53]

Antonini et al. [54] investigated the spreading of millimetre water droplets on dry surface with hydrophilic and superhydrophobic surfaces. They identified two different regimes of spreading for the investigated droplets impact. For moderate Weber number, We<200, the drop maximum spread factor and spreading time are influenced by wettability whereas for We>200 the effect of wettability is negligible as the inertial effect is predominant on the capillary effect. In another similar research, Antonini et al. [55] performed an experimental study on oblique impacts of water droplets to analyse the outcome in case of hydrophobic and super-hydrophobic substrates, varying the substrate tilt angle. They observed six different outcomes which are reported in Fig. 16, no break up was observed that's why it was possible to analyse the evolution of the fluid neglecting the presence of secondary droplets.

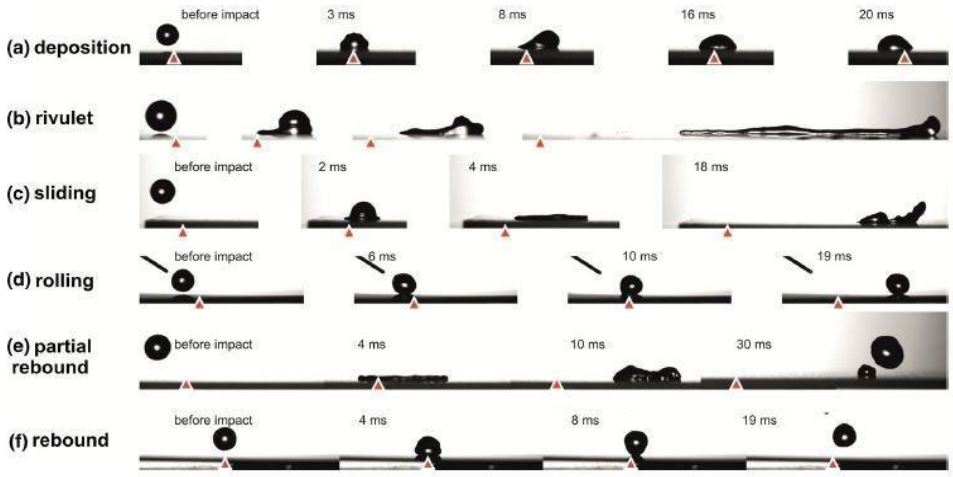

Fig. 16 Impact of water on tilted substrates [55]

They compared the different outcome obtained for the hydrophobic substrate and the super-hydrophobic substrate as a function of Weber number and tilt angle (Fig. 17)

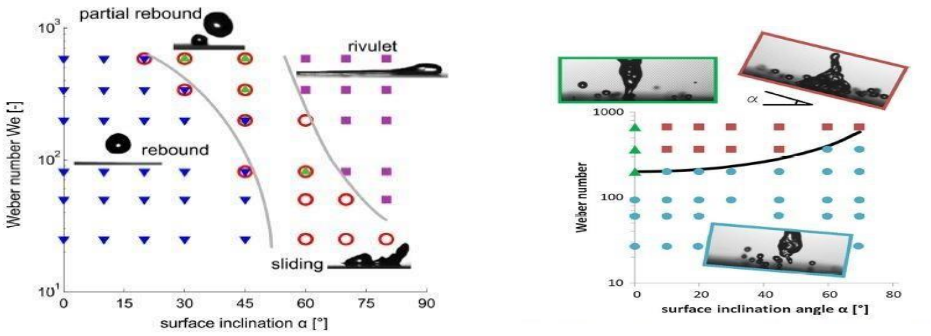

Fig. 17 Drop impact outcome map for different of substrate [55]

They pointed out that that surface tilting had a positive effect on drop shedding from the surface, allowing an easier de-wetting.

Mazloomi Moqaddam et al. [56] focused on the regime of bouncing on macro-textured superhydrophobic surfaces using the entropic lattice Boltzman model for multiphase flows. Focusing on pancake bouncing phenomenon, which occurs when the droplet after the impact leaves the surface in a pancake shape without retracting [57], they accurately estimated the transformation of kinetic energy in surface tension and vice versa. They presented numerical evidences for which the reduction in contact time occurs exclusively to the increase of droplet surfase area acting as a storage of kinetic energy during the process. This energy balance analysis, allowed them to acurately design and optimize surfaces. The assumption behind the analysis was that the kinetic energy is completely converted into surface energy at the maximal penetration into the texture. Considering also the viscous dissipation the energy balance is given by

$$K + S + \Xi = 1 \qquad 2.23$$

where K, S, Ξ are respectively the kinetic energy, the surface energy and the viscous dissipation normalized respect to E_0 which is equal to the sum of kinetic and surface energy at t=0

$$E_0 = K_0 + S_0 \qquad 2.24$$

An interesting study about surface wettability was done by Milionis et al. [58] who compared the behaviour of droplets impact in the case of water and haemolymph. Haemolymph is a substance which characterises insects, composed by a mixture of water (90%) and inorganic ions, carbohydrates, nitrogenous wastes, lipids, proteins and enzymes, pigments and hormones. Considering that haemolymph is principally composed by water, they first investigated the possibility of finding an analogy between water and haemolymph behaviour by using four different kinds of substrates: hydrophilic, super-hydrophilic, hydrophobic and super hydrophobic. They observed that the contact angle of water and haemolymph follows a similar value for the same surfaces. In the case of the superhydrophobic substrate which presents strong water and haemolymph repellent characteristic, by increasing the impact velocity and changing the tilt angle of the substrate, a few types of impact are observed (deposition partial rebound and splash with partial rebound). For all the other substrates the only observable outcome is the drop deposition. Fig. 18 shows the regimes map they obtained and the droplet impact outcomes.

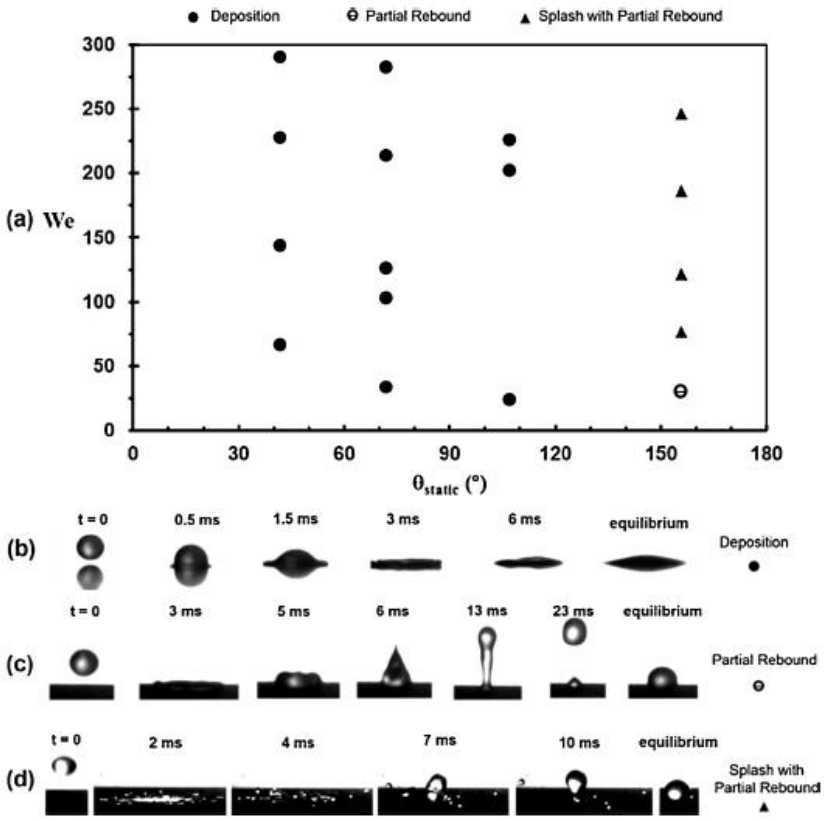

Fig. 18 Haemolymph droplet impact regimes map (a) and outcome (b-c-d) [58]

2.3 Droplet impact on porous surfaces

The phenomenon linked to the behaviour and outcome of droplets impact can be described in great detail for smooth surfaces. Many practical applications involve impacts onto surfaces of higher complexity, either morphologically or chemically, involving textured or porous surfaces or surfaces with non-uniform wettability [2] In this case the effect of surface topology on the phenomenon of droplet impact and evolution is not still fully understood.

It is possible to classify porous media and layers considering the penetration of the liquid inside the pores. In dry porous medias the pore volume is filled with air, in saturated porous medias the pores are filled with liquid and in partially saturated porous media just part of the pores is filled with liquid. To understand the transport process on the macroscopic scale it is necessary to have detailed information of the micro- and nano-scopic processes taking place on the scale of single elements [59]. Fig. 19 shows a schematic of the dynamic of a droplet impacting on a porous surface.

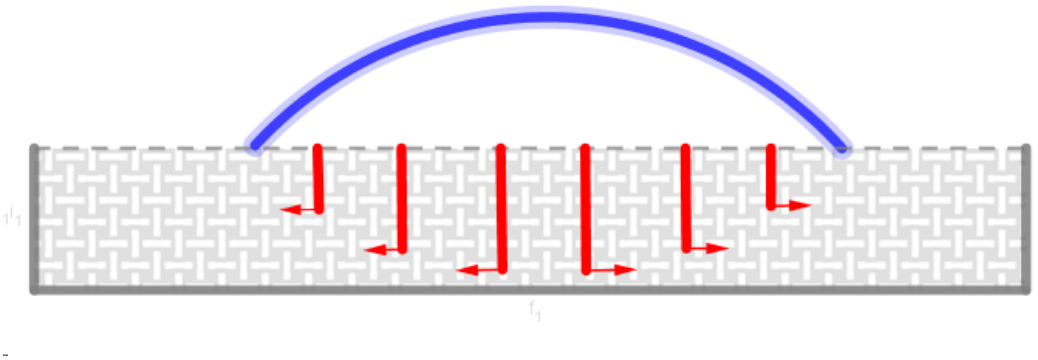

Fig. 19 Schematic of droplet impacting on a porous surface.

The understanding of the parameters that play the most important role in the evolution of the droplet inside the pore is still an open question. Depending on the droplet size, the spreading will be affected by pores dimension and distribution. For example, plant leaves are characterised by stomal pores that can have different dimension and distribution depending on the species [60]. Fig. 20 shows a schematic of stomal size and distribution.

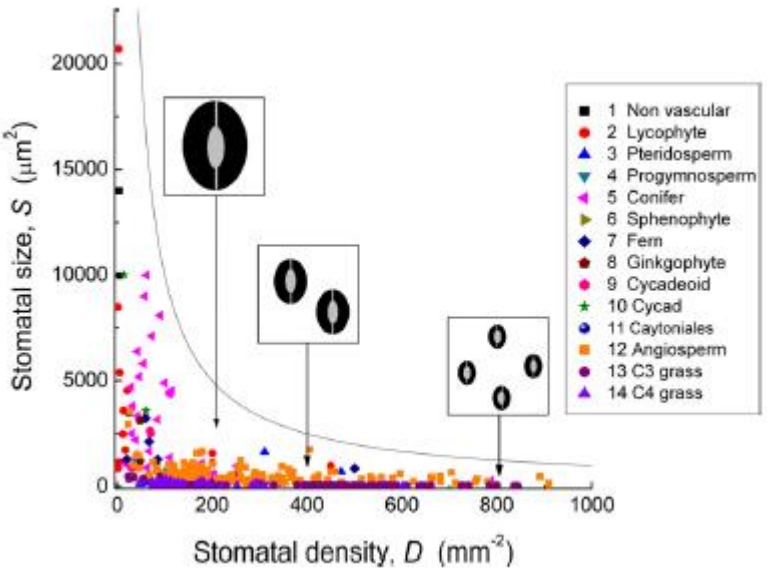

Fig. 20 Stomal size and density for different species [60]

In the spraying of agrochemicals, droplets are distributed as aqueous solutions [5]. To maximize the effectiveness of the treatment in the case of spray retention process, drops should stick to the surface, it is a critical step of the pesticides applications since non-retained drops lead to a lower efficiency of the pesticide performance. The performance of the treatment can be enhanced with an accurate analysis of the size and distribution of the droplets [61], [62].

As said porous surfaces find an application also in internal combustion engines in which the use of a porous medium (PM) enhances the performance of combustion [63]. PM burners can operate in two different modes. In the first mode, called matrix stabilized combustion, the combustion occurs within the pores of the PM and any un-reacted fuel reacts on or above the radiating surface of the medium. Basically, the radiating surface receives heat energy by convection from within the matrix and conduction from both inside and outside the radiating surface. The second mode is called stabilized mode and the combustion takes place just above the porous surface while the radiate surface is heated by hot gases above the surface.

Substantially, by using a layer with a specific porosity in cylinder-process, it is possible to obtain homogeneous and low emission combustion by enhancing fuel vaporization and distribution in space [64]. The porous structure provides the fuel a path through a homogeneously radiant field which ensures droplet vaporization

and leads to a complete reaction[65]. Fig. 21 shows a sample of a porous surface, referring to all the possible applications in the combustion process.

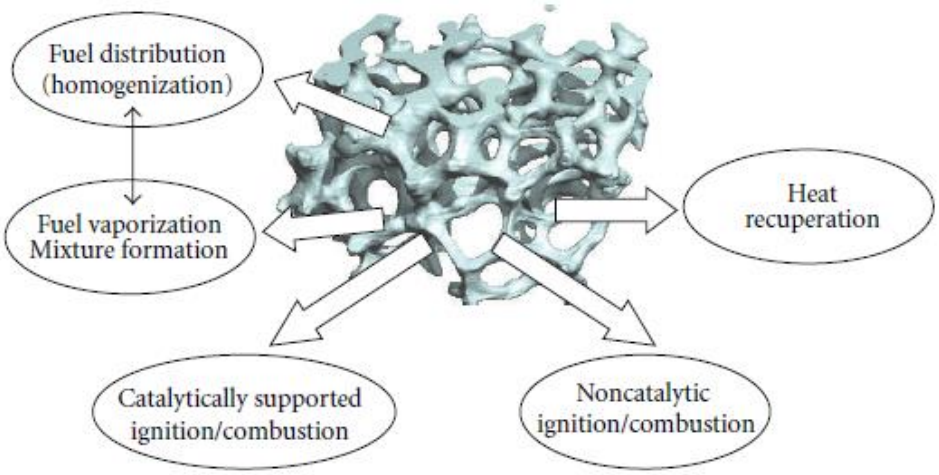

Fig. 21 Porous structure application in the combustion process [64].

Another application is given by the deposition of dyes on papers in the ink-jet printing process [38] and droplet impact in cell printing [66]. Droplet impact on porous surfaces also finds an application in fire suppression [67] considering that fires generally involve burning porous material, as in the case of the splash dynamics of droplets of suppressant liquid generated by using sprinklers on burning surfaces.

In the case of a filtration application, the separation of liquid droplets from a vapour phase in the mist systems is a process of crucial importance in several industrial processes such as natural gas cleaning and crank case ventilation. The most efficient devices are fibrous filters which must be designed with a specific spatial distribution of the local porosity and fibre diameter [68].

Considering the sheer number of practical applications that involve surfaces of this level of complexity, we have to underline the fact that the number of parameters that can affect the impact outcome is vast. For this reason, a range of numerical and experimental investigations is still required, for example, to quantify the imbibition due to porosity and identify the outcome of the impacts.

2.4 Droplet impact on porous surfaces: experimental studies

To quantify the effect of liquid penetration in porous media, Sahu et al. [69] analysed the impact of nanoparticle suspension into porous filter membranes focusing on penetration given by the hydrodynamic effect. The hydrodynamic effect occurs when the penetration of the droplet into the pore is due to a larger dimension of the droplet diameter, respect to the pore diameter. They observed that, the penetration of the droplet into the pore is enhanced if the dynamic pressure is higher than the capillary pressure, but also when hydrodynamic focusing, is observed. Kumar et al. [70] pointed out that the imbibition is influenced both by the material of the porous media and by capillary forces due to the capillaries formed by the porous bed. They observed that the time required for the droplet imbibition increases with the droplet diameter.

Analysing the spreading behaviour of a droplet on a porous surface, Marston et al [71] presented results from an experimental study of impact of liquid drops onto powder beds pre-wetted with the impacting liquid. They based the analysis on a numerical study carried out by Clark et al. [72]. They found out that the maximum spread is a function of the moisture content in the powder bed which means that there is an optimum moisture content that can leads to a faster penetration. Fig. 22 shows an example of the impact of a droplet on a porous dry surface compared to the impact of a droplet on a partially saturated powder.

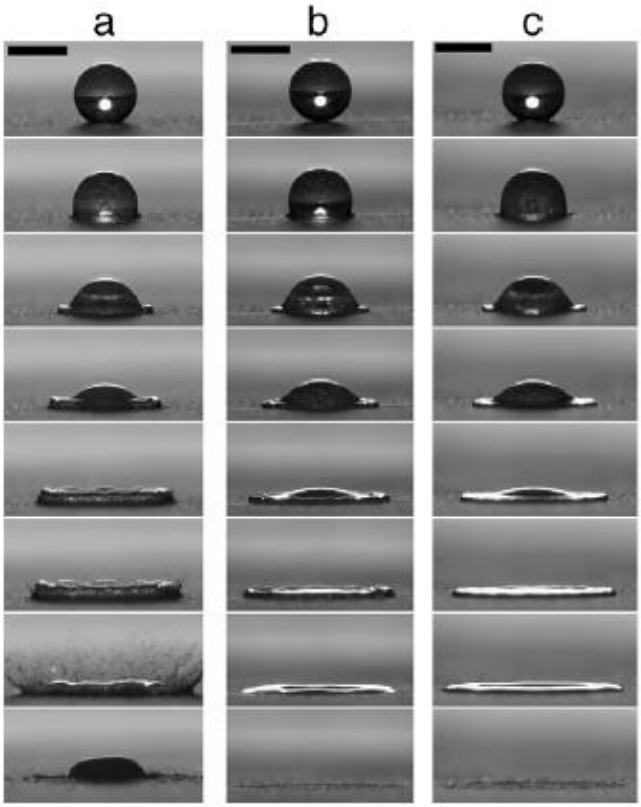

Fig. 22 (a) Impact of droplet on a dry surface (b), (c) Impact of droplet on partially saturated powder. [71]

Lorenceau et al. [73] analysed the impact of droplet against thin plates pierced with small holes. They focused on analysing the threshold velocity limit for which the liquid is captured by the surface or is ejected below it. Fig. 23 and Fig. 24 show respectively an example of droplet impact in which the droplet is captured by the surface and one in which is it can penetrate below it.

Fig. 23 Impact of droplet captured by the surface [73]

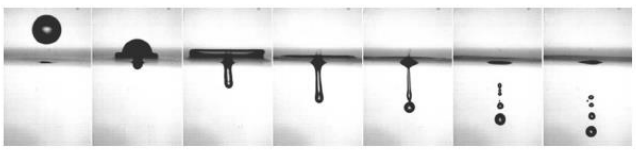

Fig. 24 Impact of droplet ejected below the surface [73]

They identified a critical speed for which the droplet is not entirely captured by the plate but is ejected below the surface after the impact. They defined a critical Weber number and Reynold number based on the dimension of the pore.

$$We^* = \frac{\rho R_p v_i^{*2}}{\sigma} \qquad 2.25$$

$$Re^* = \frac{\rho R_p v_i^*}{\mu} \qquad 2.26$$

Comparing the effect of the viscous and capillary force, they observed that in the limit of small Re, the viscous force is dominant and should be responsible for the capture of the drop. Increasing the Reynold number, Re> 100, the critical Weber number is found to be constant. In this regime, the critical speed does not depend on viscosity and is set by a balance between inertia and capillarity. Fig. 25 shows the graph pointing at the threshold velocity limit for which the droplet is captured by the surface or partially ejected. The thin line representing the velocity threshold for the droplet capture is given by the equation

$$Re^* = \frac{5.1We^*}{We^* - 3.6} \qquad 2.27$$

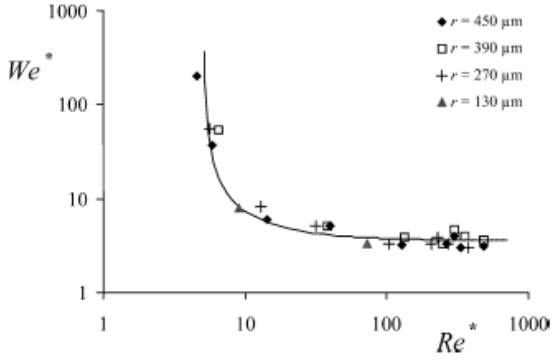

Fig. 25 Threshold velocity for capture [73]

Piroird et al.[74] analysed droplet impacts on inclined fibers which are used to capture liquid droplet in the case of filers or fog's net. In this kind of application, it

is mandatory to optimise the efficiency of capture. They observed that the capture efficiency depends on the impact velocity. At low impact speed, the droplet runs down along the fiber, leaving a film behind, whereas at higher impact speed the droplet crosses the fiber and get deflected. The process is shown in Fig. 26.

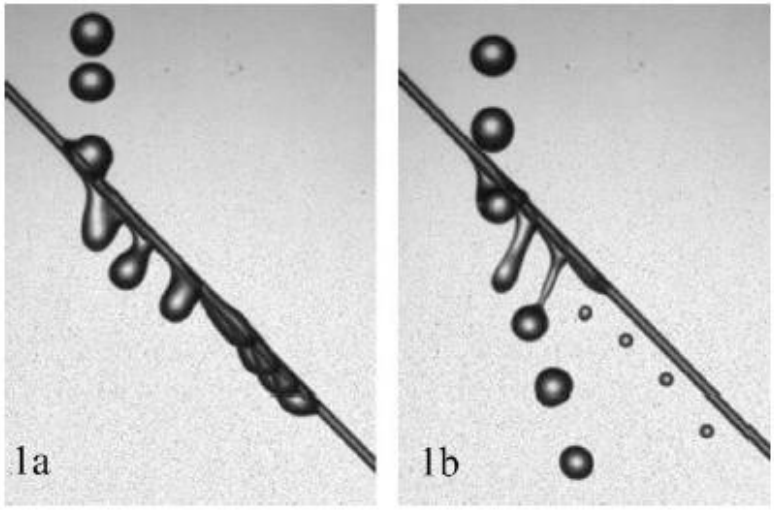

Fig. 26 Droplet impact on a fiber (a) $v = 30\frac{cm}{s}$(b) $v = 45\frac{cm}{s}$ [74]

They found out that the capture efficiency increases by tilting the fibre. If the tilt angle increases from 25° to 80° the velocity threshold below which a droplet is fully captured increases of a factor larger than 5.

In a similar study, Yamamoto et al. [75], investigated droplets impact on textured stainless-steel surfaces fabricated by aligning steel razor blade in parallel. They observed a mechanism of partial penetration in interval of Weber number between 5 and 10 because of the collapse of the air cavity at the centre portion of the recoiling droplet. Fig. 27 shows a picture of the set-up used for their experiments.

Fig. 27 Droplet impact on a razor blade [75]

Delbos et al [76] investigated how the impregnation of porous media can be forced using the initial kinetic energy of a drop. Focusing on the scale of a single pore (either hydrophilic or hydrophobic), they observed a rich variety of regimes for different combinations of impact velocity, tube radius and wetting condition quantifing the velocity thresholds for the different regimes. At low impact velocities impregnation occurs. At high impact velocities, the drop breaks in two parts. One part of the droplet spreads at the top of the surface whereas the other part is trapped inside the pore. They determined a diagram with a critical speed to separate this regime which is shown in Fig. 27. The circles correspond to the regime where the liquid inside the tube is still connected to the liquid outside , the squares to regime where no liquid is in the tube and the triangles to the formation of a slug. The critical velocity for slug formation is represented by the plain line and the dashed line is for the critical impact velocity for penetration of liquid into the tube. The equations for the threshold velocity are respectively

$$\frac{1}{2}\rho(v_1)^2 = -\frac{2\gamma\cos(\theta)}{r_t} - \frac{2\gamma}{r_d} \qquad 2.28$$

$$\frac{1}{2}\rho(v_2)^2 = -\frac{2\gamma\cos(\theta)}{r_t} + \frac{2\gamma}{r_d} \qquad 2.29$$

where r_d and r_t are respectively droplet and tube radius, γ and ρ liquid surface tension and density and θ the contact angle.

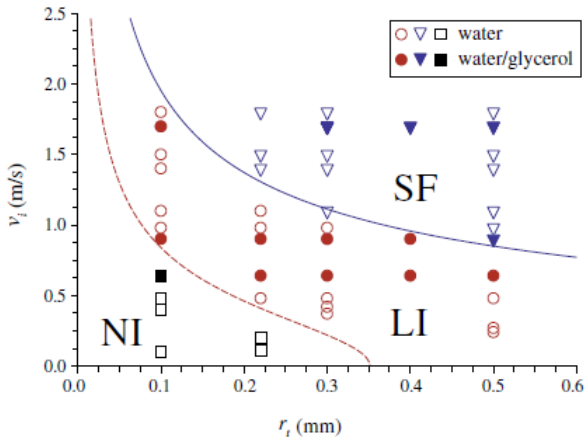

Fig. 28 Phase-diagram of the different regimes observed for water (open symbol) and water and glycerol mixtures (plain symbols). Drops impacting on hydrophobic tubes {Formatting Citation}

Xu et al. [77] performed a study of droplet impact on mesh membranes which are a functionl material for gas-water or oil-water separation. As in the study of Lorenceau et al.[73], they determined a critical velocity for which after the impact, a daughter droplet will be generated below the pore. Their analysis shows that the liquid penetration is related to the number of mesh pores within drop project area, N. They defined N as

$$N = \frac{A_s}{A_u} = \frac{\pi D^2}{4} \cdot \frac{1}{(D_p + D_w)^2} \qquad 2.30$$

Wehre A_s and A_u are respectively the projected area of the droplet on the surface before the impact and the unit area on the mesh, including a pore. A higher value of N will lead to a smaller critical velocity for which the penetration occurs. Fig. 29 and Fig. 30 show an example of droplet impact on the same mesh but with a different initial diameter. In the case of Fig. 29, a intial diameter of 1.84 mm leads to a N equal to 269 and a critical velocity equal to 1.56 m/s, whereas in the second example of Fig. 30, a initial diameter equal to 4.17 mm leads to a N equal to 1319 and to a critical velocity equal to 1.107 m/s.

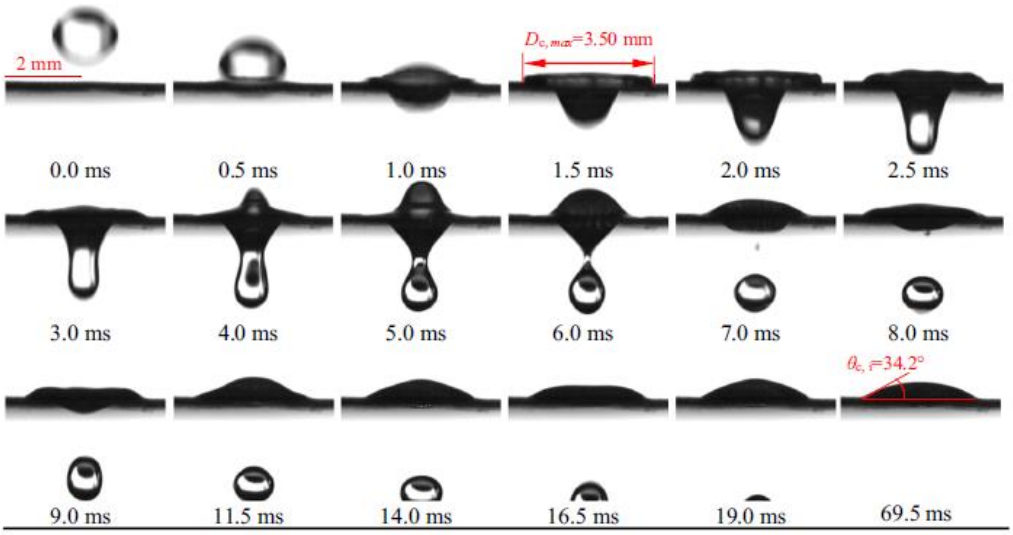

Fig. 29 Impact of droplet on a mesh surface with N=269 [77]

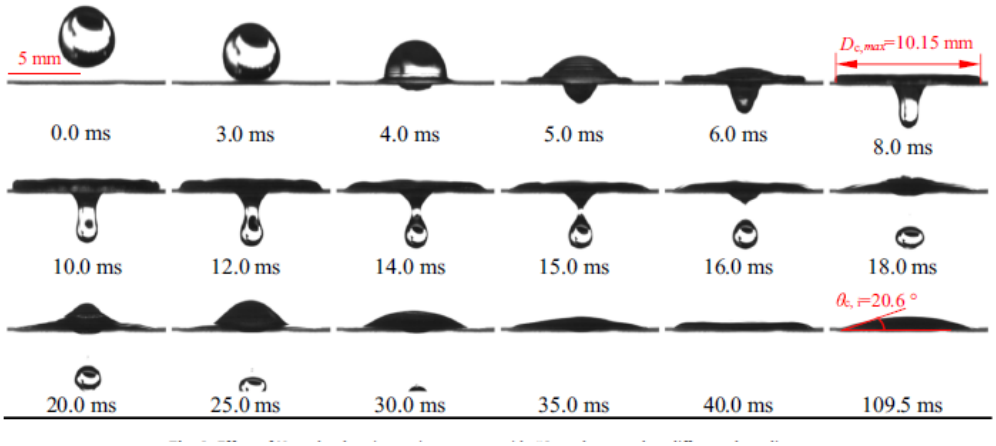

Fig. 30 Impact of droplet on a mesh surface with N=1319 [77]

In determining the critical velocity for which after the impact, a daughter droplet will be generated below the pore, they pointed out that drop impact on the membrane yields significant liquid compression resulting in an additional effect given by water hammer pressure which enhances droplet penetration. Hence the penetration occurs if the dynamic and water hammer pressure overcomes the capillary pressure.

$$p_d + p_{WH} > p_c \qquad 2.31$$

defining a coefficient, k given by the ratio of the dynamic pressure and the water hammer pressure, the same equation can be written as

$$\frac{(1+k)\rho v_i^2}{2} > -\frac{4\sigma cos\theta_A}{D_w} \qquad 2.32$$

where ρ and σ are density and surface tension, θ_A is the advancing contact angle measured on the mesh and D_w is the wire diameter. The coefficient k identifies the importance of the water hammer pressure and is correlated to N

$$k = \frac{8}{1.1+\frac{466}{N}} - 1 \qquad 2.33$$

combining the previous equations yields to

$$-\frac{We_w}{\cos(\theta_A)} = 1.1 + \frac{466}{N} \qquad 2.34$$

where the left side of the equation is defined as modified Weber number and includes the effect of the advancing contact angle. The modified Weber number reaches a minimum value of 1.1 if N is very large. The maximum value of the coefficient k is given by 6.27. The correlation of k and modified We number with N are shown in Fig. 31.

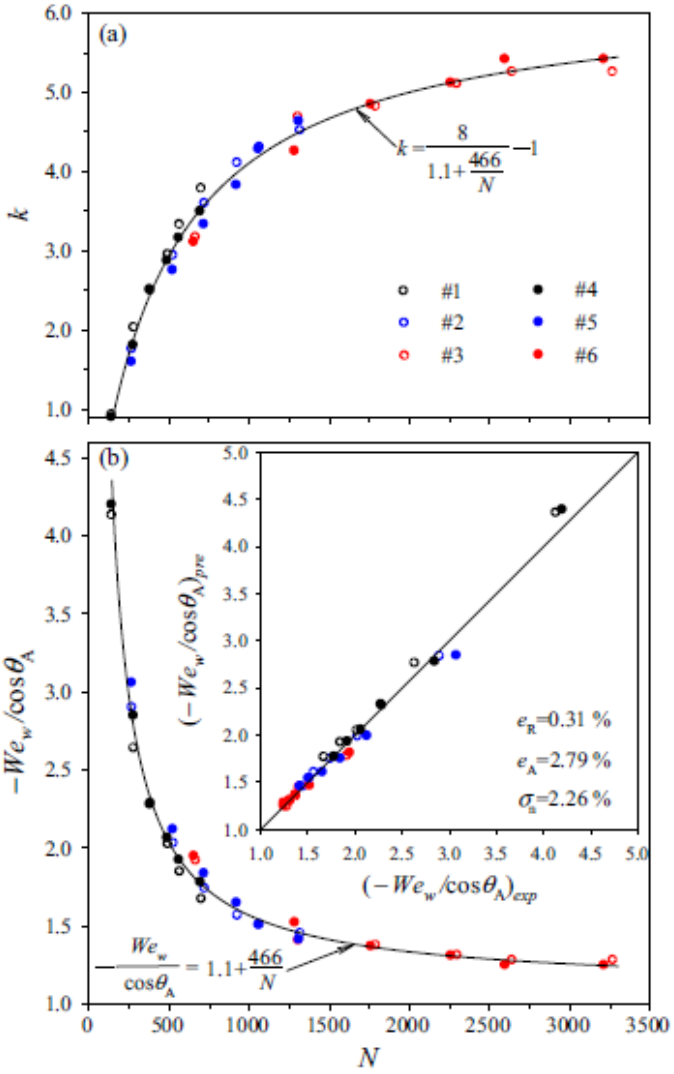

Fig. 31 Correlation of k and modified Weber number to N [77]

Ryu et al. [78] analysed droplet water impact on meshes with submillimetre pores, focusing on different surface wettability, hydrophobicity and super hydrophobicity. They observed that a higher impact velocity is required in order to enhance the

penetration in the case of the hydrophobic surface, whereas in the case of the super-hydrophobic meshes, penetration may occur during the recoiling stage, at a lower velocity respect to the velocity limit for penetration. They proposed that this effect can be attributed to the hydrodynamic focusing or to the momentum transfer from the drop when it is about to bounce from the surface. They defined different cases of penetration base on is timing: IP (impact penetration), RP (recoil penetration), N (no penetration), I (incomplete penetration), C (complete penetration).
The cases are shown in Fig. 32.

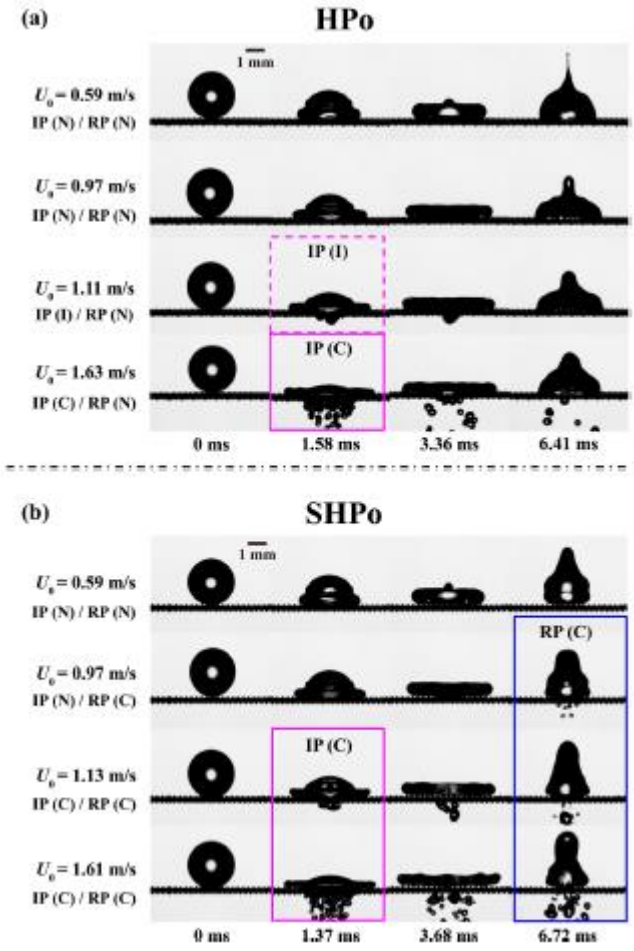

Fig. 32 Sequential images of droplet dynamics (a) hydrophobic meshes (b) super hydrophobic meshes [78]

Fig. 33 shows the penetration diagram in function of the impact velocity and the anti-penetration capillary pressure for hydrophobic meshes. In the diagram equations (1) is obtained considering the balance between dynamic pressure and capillary pressure by

$$C_0 \rho U_{IP}^2 = p_c \qquad 2.35$$

$$U_{IP} = \frac{\sqrt{p_c}}{\sqrt{\rho}} \qquad 2.36$$

where C_0 is a constant equal to 2.78.

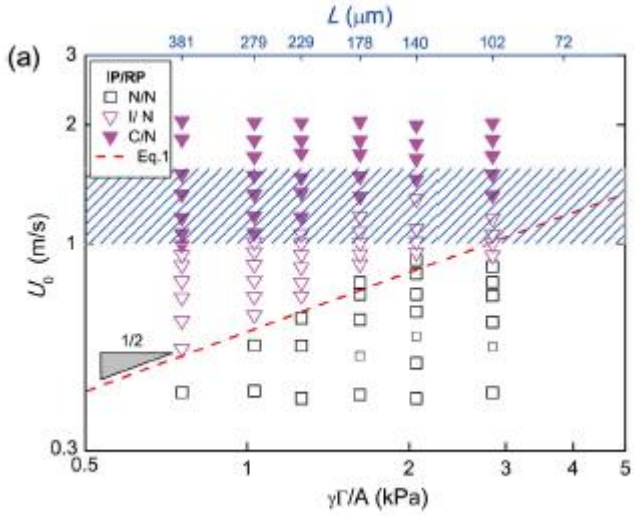

Fig. 33 Penetration diagram as a function of velocity and capillary anti-penetration pressure; hydrophobic meshes ; IP=impact penetration, RP=recoil penetration, N= no penetration, C= complete penetration [78]

Brunet et al. [79], analysed droplet impact on hydrophobic micro-grids. They pointed out that above a threshold speed, liquid emerges on the other side of the grid forming microdroplets and proposed a model to produce monodisperse spray. Fig. 34 and Fig. 35 indicate respectively the dimensions of the different grids and the diagram of the number of the emerging droplet versus Weber number. The general trend shows an increase of droplets number at larger We.

Grid number	Thickness t (μm)	d_{min} (μm)	d_{max} (μm)	b (μm)	a (μm)
1	49	22	93	117	36.5
2	47	49	117	120	97.5
3	38.5	38	91	121	69
4	56.5	35	117	118	65
5	56	10	93	119	16.5

Fig. 34 Dimension of different grids, b indicates the space between the holes and a is the diameter of the emitted droplet. The grids are characterised by pores with a trapezoidal shape in which dmax and dmin are respectively the largest and the smallest dimension of the trapezoidal hole. [79]

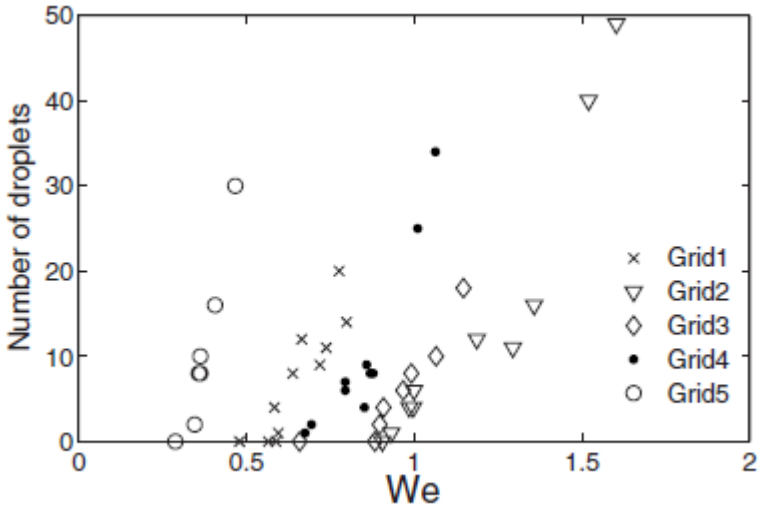

Fig. 35 Number of emerging droplets for different grids [79]

2.5 Numerical studies

Several numerical studies were done to analyse the dynamics and physics of droplet impact on complex surfaces.

Clarke et al.[80], combined a model linked to the droplet spreading with an equation to describe the imbibition process on a porous surface, developing a new model to describe the spreading and imbibition of droplet on porous membranes. The equations are respectively given by

$$\frac{\partial r}{\partial t} = \frac{2k_s^0 h\lambda}{\mu\nu}\sinh(\gamma(\cos(\theta_0) - \frac{\cos(\theta)}{2nk_b T}) \quad 2.37$$

$$r = \left[\frac{3V}{\pi} \cdot \sin^3(\theta)/(2 - 3\cos(\theta) + \cos^3(\theta))\right]^{\frac{1}{3}} \quad 2.38$$

The first equation results from the molecular-kinetic theory. k_s^0 is a molecular jump frequency at n sites of solid/liquid interaction per unit area of the substrate, h is Planck's constant, ν is the molecular volume, λ is the molecular jump length, r is the base radius of the drop, μ is the viscosity, σ is the liquid surface tension, θ_0 is the equilibrium contact angle, θ is the instantaneous dynamic contact angle, k_b is Boltzmann's constant, and T is the temperature.

The second equation describes the relaxation of the drop and V is the volume of the drop.

Varying the liquids properties, they observed that the imbibition process is highly influenced by the magnitude of the surface tension. In fact, for higher surface tensions the imbibition process occurs in a time of more than 2 orders of magnitude longer respect to low surface tension liquids. This can be explained considering that liquids with a higher surface tension have a larger contact angle. Moreover, considering the porous structure, the complex internal geometry of real porous systems inhibits penetration by poorly wetting liquids. With a large contact angle, not all pores are filled.

Lee at al. [81] presented an experimental investigation and numerical analysis of the absorption of water droplets impacting porous stones, capturing the full penetration process of the impinging droplet. They observed that for a short time after the impact, before the absorption phase, the droplet spreads without any mass penetration into the substrate showing a non-wetting dynamic behaviour, due to the presence of an air layer between the droplet and the porous substrate. Once the maximum spreading is reached, the layer between droplet and surface is broken at the contact line. This leads to capillary contact and a change of the contact angle form a non - wetting to wetting behaviour. The absorption phase is initially hindered by the presence of the entrapped air, but once the air disappears the absorption process starts and is faster in highly capillary active stones. Once the absorption process is over, the evaporation phase begins. Spreading and absorption are influenced by droplet initial velocity. They developed a finite-element numerical

model for isothermal moisture transport in unsaturated porous media, capable to capture properly the mass absorption. The model finds a good agreement with experimental data. Fig. 36 shows a schematic of droplet impact on a porous stone.

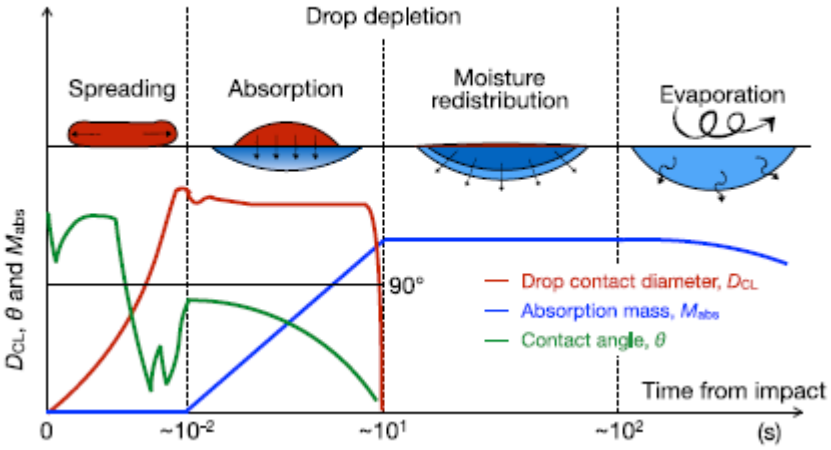

Fig. 36 Schematic of droplet impact and penetration into a porous stone [81]

Karepetsas et al.[82], investigated droplet interaction, considering both smooth and structured surfaces. Specifically, they focused on the droplet sliding on an inclined surface. They pointed out how dynamic hysteresis, given by the droplet motion along the inclined solid surface can be linked to the topography of the substrate and in the case of a structured surface, they predicted the effect of static hysteresis by observing that the droplet slides only beyond a certain critical inclination angle.

Hicks et al. [83] compared droplet impacts on a porous substrate with a rough impermeable surface as an approximation for a textured surface. They found out that the change from a flat rigid impermeable plate to a porous substrate reduces the initial horizontal extent of the trapped air pocket, as the porosity structure provides additional pathways through which the gas can escape.

They also investigated the effect of surface tension on gas-cushioned droplet impacts with porous surfaces and noticed that in contrast to the numerical predictions given for a droplet impacting above flat plate, when a porous substrate is included, the droplet free-surface touches down in finite time. This phenomenon leads to the physical explanation that the level of surface roughness is a critical parameter in determining the initial touchdown characteristics. To study the phenomenon, they defined an effective permeability k, depending on droplet radius

and initial velocity, liquid properties and actual substrate permeability. Fig. 37 show the evolution of the droplet free-surface (top) and gas film pressure (bottom) in time. Here h refers to the pillar size, α is a coefficient which depends on the material and pore properties and $\delta = 1$ indicates that slip is allowed.

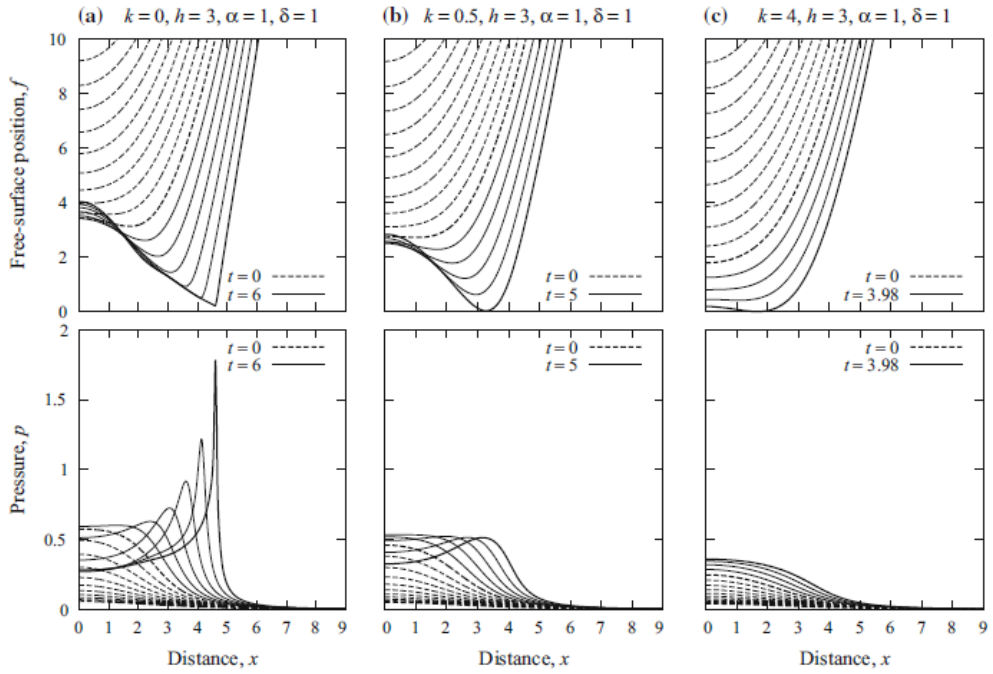

Fig. 37 Evolution of droplet free surface (top) and gas film pressure (bottom) in time. [81]

Choi et al [84] developed a sharp-interface LS method to analyse droplet impact and penetration into a porous medium. They demonstrated the dependence of the droplet penetration width and depth on the initial droplet radius, impact velocity, contact angles, particles size and porosity. Fig. 38 and Fig. 39 show respectively the influence of droplet initial diameter and impact velocity on the droplet penetration.

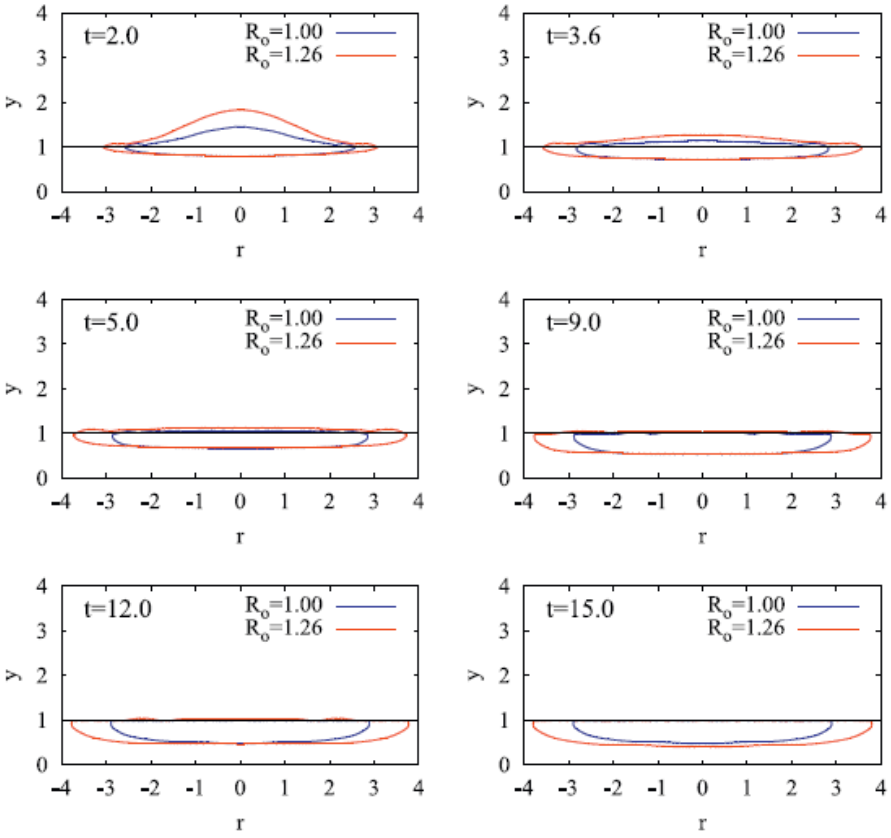

Fig. 38 Effect of initial droplet radius on droplet penetration [84]

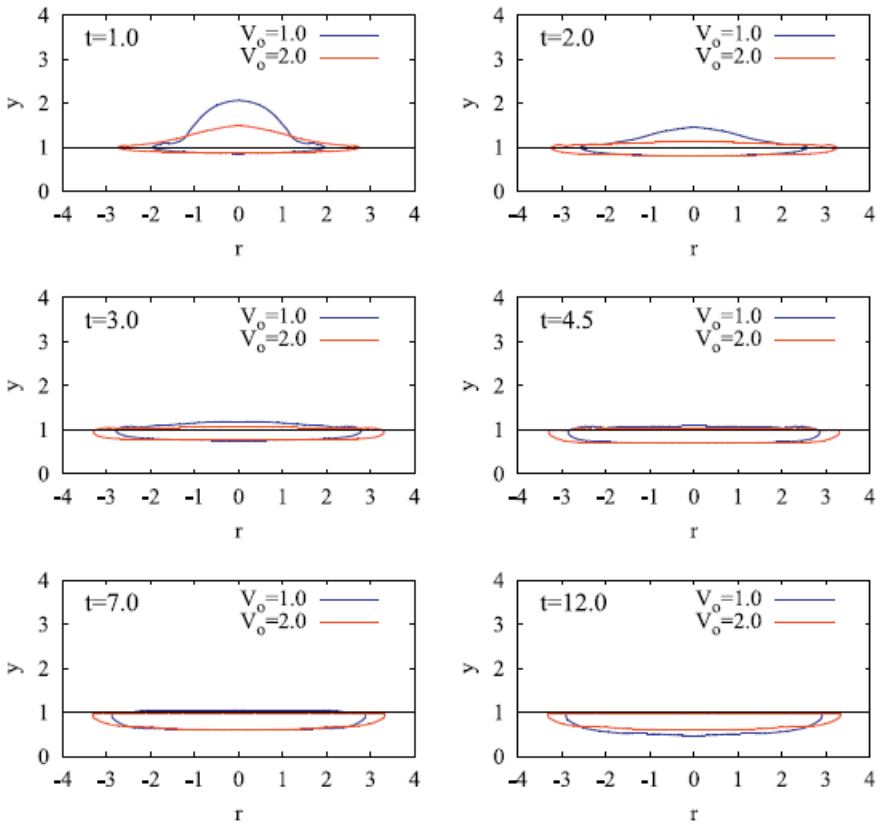

Fig. 39 Effect of impact velocity on droplet penetration [84]

2.6 Medical applications

Droplet impact on complex surface can also be linked to medical applications. In fact, thinking about a complex surface it is relevant consider characteristics such as elasticity, roughness and porosity for which reason it represents a good description of the human skin.

The skin is defined as the largest human organ and 'protective envelope', which covers between 1.6 and 2 m^2 surface area of the human body in adults and accounts for approximately 16% of a person's weight.

The main duty of the skin is to protect the human body from the surrounding environment as an interface. In fact, skin mainly acts as a wall which protect human body from infections.

Underlying organs are protected by the skin from pathogens and microorganisms, whereas the skin is exposed to potentially harmful microbial, thermal, mechanical, and chemical influences. Skin health also has a great importance and is a major concern for people which normally invest in skin product which efficiency can be enhance by a deeper knowledge of skin structure [85].

The skin is composed by multiple layers: Stratum Corneum, Epidermis and Dermis [85]. The tribology of the skin is of great importance in different fields like sports, medicine and cosmetics. The complexity of his evaluation is due to its layered morphology and the viscoelastic plastic nature. The stratum corneum, top layer of the skin with a thickness of circa 20 μm, has a Young module of 1-3 GPa. This value may decrease of a factor of 100-1000 with increasing water content [86]. Fig. 40 and Fig. 41 show a schematic of the skin structure.

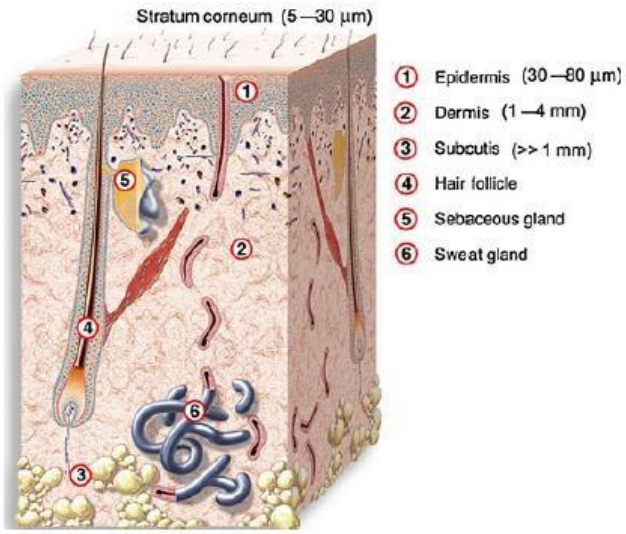

Fig. 40 Structure of Human skin, functional layers . [85]

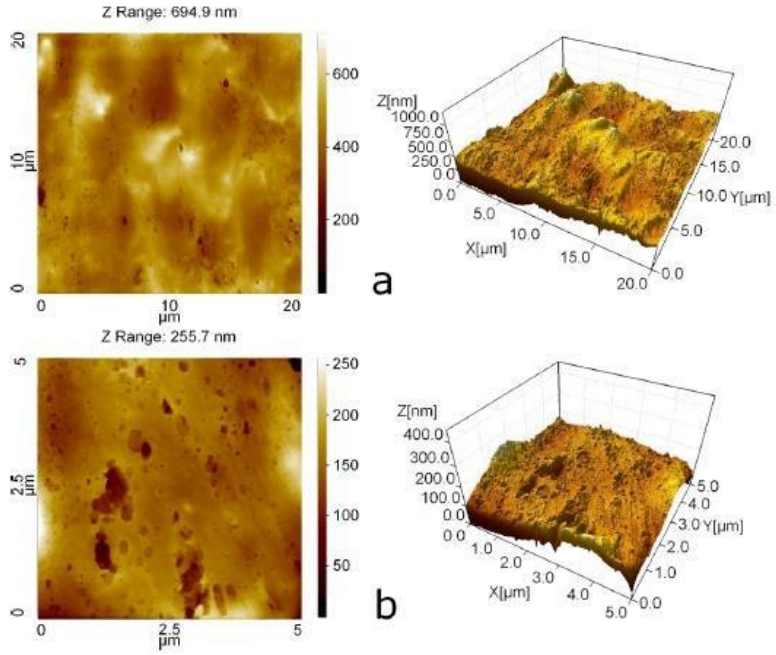

Fig. 41 Atomic Force Microscope Images of wet human skin [86]

Depending on the different kind of tissues that constitute human body, pore size can cover a different ranges. One of the most common theory which describes skin porosity is the aqueous pore pathway hypothesis which describes the transdermal transport of hydrophilic solutes into the skin. It states that the

transport of solutes across the skin is due to the presence of aqueous channel or pores with a cylindrical morphology, which crosses the skin barrier [35].

Several studies were done to deeply understand the human skin morphology and structure, in order to define its elastic properties and pores dimension. For example, a possible way to estimate the pore size on human skin is given by an analysis of its electro kinetic phenomena which can be applied on a human cadaver. In fact, iontophoresis, which applies voltage gradient on the skin, is recognised as an effective method which aims to enhance the transdermal delivery of drug [87], [88].

A deeper understanding of the skin morphology allows an improvement of the drug delivery and absorption. Actually, if the key formulation features contributing to the drug penetration are determined, the optimization of the formulation becomes feasible [89].

Aguilella et al. [87] analysing the Stratum Corneum by using a microscopic model found a mean radius distribution of the pores of 20 nm.

Lee et al. [90] by using a cosmetic cleanser composed by Diospyros kaki folium, observed that face skin pores size can decrease from 70 to 20 nm.

Goswami et al. [91] analysed the oral mucosa for the delivery of hydrophilic macromolecules. To increase the penetration of the molecules that may occur via the aqueous route, it is essential to know the dimension of the route. They found out that the pores size is in a range between 1.8-5.3 Å.

Considering the human skin, another physical characteristic that plays an important role is elasticity. The impact of droplets on membranes or elastic surfaces is linked as well to the concept of complex surfaces.

Considering for example a membrane, it is possible to refer to the elastocapillary effect that occurs due to the double effect of capillary and elastic forces, i.e. substrate deformation. This kind of phenomenon can be easily observed in nature thinking about wetting of leaves, animal wings, bacteria adhesion on surfaces, self-organization of cell tissues and spreading of cells [92].

Referring to how elasticity can affect droplet impact, in the work of Weisensee et al. [93] we can observe that, considering two different surfaces, both super-hydrophobic but one elastic and the other rigid, the presence of elasticity will bring to a spread-boarding and will reduce the contact time of the droplet on the surface. Fig. 42 shows an example of the results they obtained.

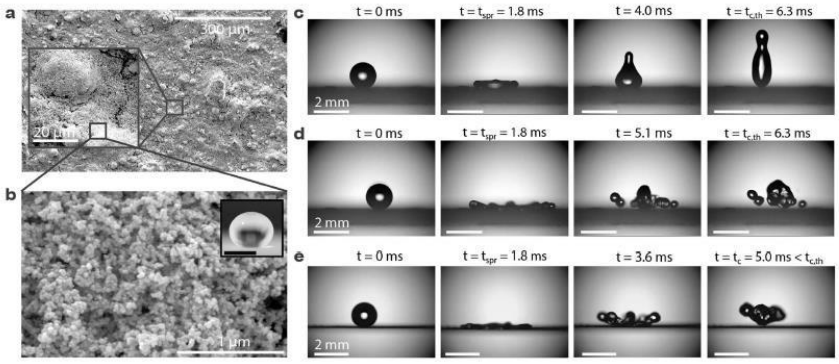

Fig. 42 Surface characterization and dynamic behaviour of water droplet impact on rigid and elastic superhydrophobic surfaces [93]

Considering again a medical application, by evaluating the kind of impact it is possible to estimate the elasticity of a certain tissue, as in the study of Dias et al.[94], that analysed elasticity and viscoelasticity in the anterior and deeper stromal regions of the cornea in order to halt the progression of specific corneal disorders such as keratoconus and post-LASIK corneal ectasia. An increase of corneal stiffness enhances the effects of the disorders.

Great efforts have also been made to create a human skin Equivalent (HSE), that reproduce human skin [95].

In fact, considering that if the skin is damaged it becomes difficult to transplant, it is better to recur to an artificial skin which is becoming dramatically important in tissue market and texture engineering [96],[97],[98].

In order to reproduce human skin, Zhao et al. [99] successfully prepared a Porous dermal scaffold membrane (PDSM) by using a so-called sol–gel freeze-drying method. The tissue engineered dermal scaffold, plays an important role in tissue engineering technology of repairing damaged dermis. The biodegradable scaffold provides three-dimensional space and suitable environment which are beneficial for dermal cells' growth, adhesion and proliferation. They obtained a very well distributed pore size, between 100 µm and 200 µm and a tensile strength was above 0.09 MPa. Fig. 43 shows a sample of the PDSM scaffold.

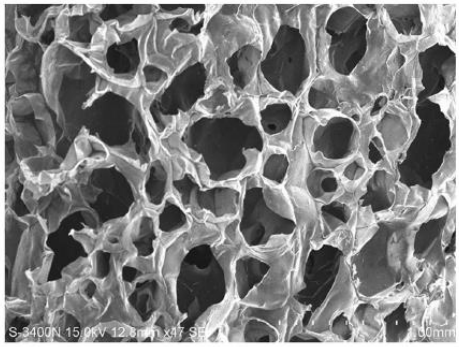

Fig. 43 Sem Image of PDSM scaffold [99]

Lake et al. [100] analysed 5 prototype meshes composed of flat, monofilament polyethylene terephthalate. They did not observe a significant difference respect to mesh density, but they noticed that mechanical strength of tissue ingrown occurred as pore size increases. Hexagonal pores lead to a stronger tissue ingrowth.

Zhang et al.[46], prepared porous composite scaffolds by combining polygrlycerol-sebacate (PGS) with silk fibroin microfibers and chitosan. They evaluated the biocompatibility of the PGS base composites scaffold for a tissue engineering application by doing cell culture experiments. They observed a good proliferation and penetration of the cells into the composite.

3 Materials and Method

3.1 Surface and Liquid Properties

The target surfaces used in the present research, were selected from a set of stainless steel metal meshes mainly used for filtration applications, with pore equivalent diameter varying from 25 to 400 μm (Plastok® Meshes and Filtration Ltd., Birkenhead, Merseyside, UK). This represents a kind of structured porous surface that can be characterised by two parameters, mesh wire diameter and pore width, both of which were varied. The surfaces are characterised by a woven structure with cross sectional areas. Table 1 lists the properties of the meshes used in experiments. Fig. 44 shows a sample scanning electron microscope (SEM) image of the stainless steel meshes with the corresponding static contact angle and advancing contact angle.

Table 1 Meshes properties

Sample Number	Pore Equivalent Diameter (μm)	Wire Diameter (μm)
1	25	25
2	50	36
3	80	65
4	100	65
5	150	100
6	200	125
7	250	100
8	400	220

Three liquids were used: water, acetone and a glycerol-in-water solution, G&W, composed of 20% of water and 80% of glycerol (by volume), to analyse the effect of viscosity and surface tension of liquid. The properties of the liquids are listed in Table 2.

A combination of different surface porosities and liquids is needed to study how the impact outcome is influenced by liquid physical properties and mesh geometry.

Table 2 Liquid Properties

Liquid	Density (kg/m^3)	Viscosity (mPa s)	Surface Tension (N/m)
Water	996	1	0.073
Acetone	793	0.30	0.023
Water & Glycerol	1118.6	10	0.067

The value of density, viscosity and surface tension for the solution of water & glycerol are given considering the average of 3 different measurements done on the same mixture. The viscosity and the surface tension were calculated respectively with a viscosimeter and a rheometer. The rheometer was calibrated on distilled water with a surface tension of 0.073 N/m.

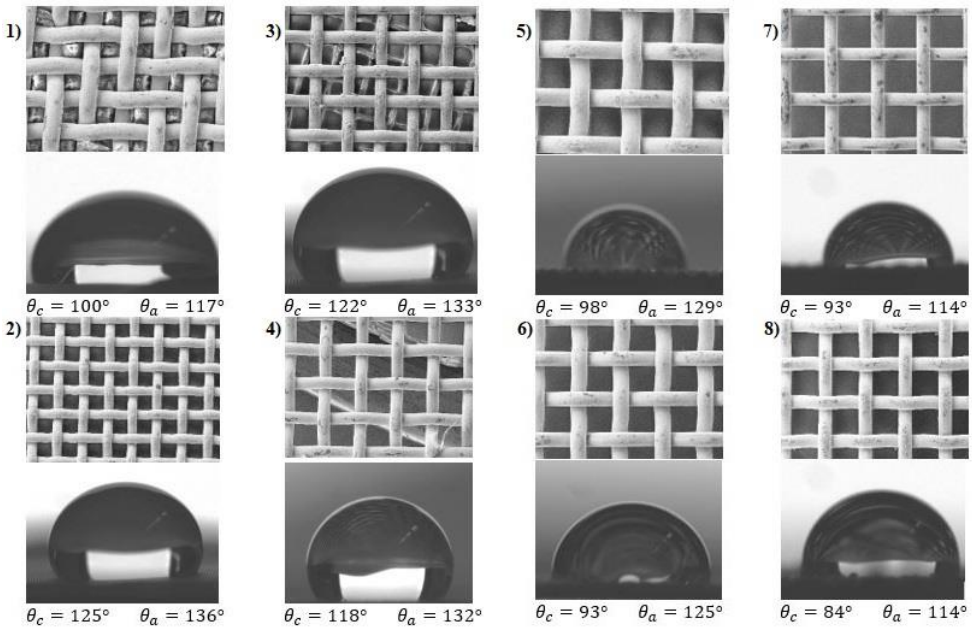

Fig. 44 SEM images of the stainless steel meshes and measures of static and advancing contact angle.

The reported static contact angle of water on stainless steel is usually of 71° whereas in the case of the meshes used for the experiments it falls in a ranges between 84°&125 °. This can be explained considering the fact that the woven structure of

the mesh can also affect the wettability properties enhancing the roughness of the surface. To confirm the average pore dimension for each mesh, an analysis was done on the SEM pictures with the Smart TIFF software, checking the dimension of 5 pores for each case. Table 3 confirms that the average measure is accurate enough. Subsequently it was observed from the experimental analysis that the slight difference in the pore dimension does not affect the final outcome.

Table 3 Pore dimension measured with the smart TIFF software

Mesh N°	Measure 1 (μm)	Measure 2 (μm)	Measure 3 (μm)	Measure 4 (μm)	Measure 5 (μm)	Average (μm)	σ(μm)
1	24.94	25.23	28.80	29.69	22.86	26.3	2.85
2	84.11	82.14	83.13	78.14	77.19	80.9	3.09
3	106.9	107.9	110.8	112.8	110.8	109.8	2.40
4	127.7	127.7	124.7	130.6	125.7	127.3	2.27
5	158.3	158.3	156.4	159.3	158.3	158.1	1.05
6	204.9	203.4	203.4	206.3	207.8	205.1	1.91
7	253.8	247.9	246.4	249.4	245.8	248.6	3.19
8	410.3	405.2	400.3	400.3	404.3	404.0	4.14

3.2 Experiment groups and set-up

The experiments were organised in different groups characterised by a different combination of initial parameters such as impact velocity, droplet diameter and liquid physical properties. To obtain a range of impact velocity between 2 m/s and 4 m/s, the height of release was varied between 20 cm and 80 cm. The droplet is manually released from the needle exclusively thanks to gravity force. Two different needle sizes, 21 gauge, (0.82 mm OD, 0.51 mm ID) and 26s gauge (0.47 mm OD, 0.13 mm ID) were used to vary drop diameter. The 26s gauge was filed to make droplets fall vertically and with a better repeatability. (Fig. 2a-b). It is important to observe the effect of a different drop size on the surface to evaluate in which way the ratio between the pore size and the droplet size can affect the final outcome.

Fig. 45 (a) Needle size 21-gauge (b) Needle size 26s-gauge

To confirm repeatability, the droplet impact was recorded at least 5 times under each set of impact conditions.

The optical setup included a Photron Fastcam SA4 high speed camera with a resolution of 1024x800 pixels (Fig. 46). The lens used to record each video is a Sigma 24-70mm F 2.8 EX DG.

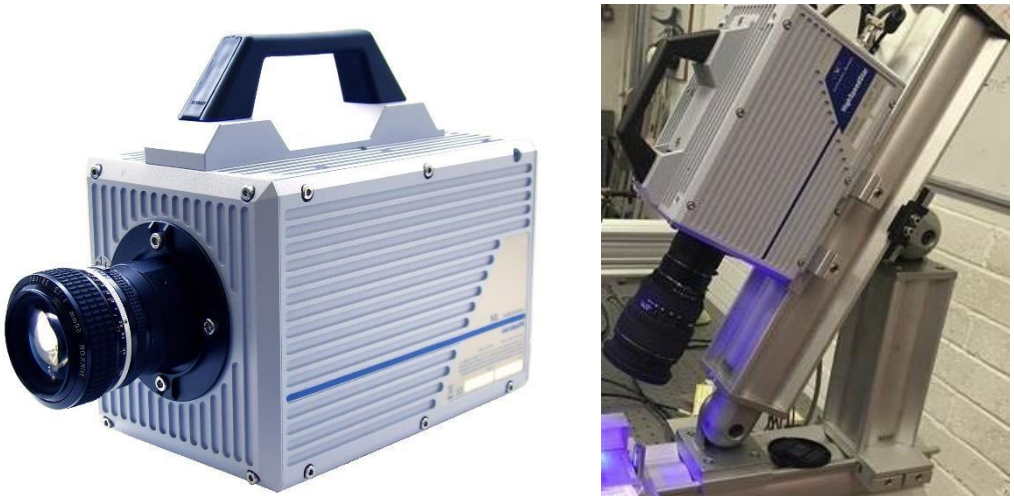

Fig. 46 Photron Fastcam

The test area was illuminated using a custom-built high-speed LED light source, synchronised to the high-speed camera and spatially homogenised by lenses and a glass diffuser (Fig. 47 a-b).

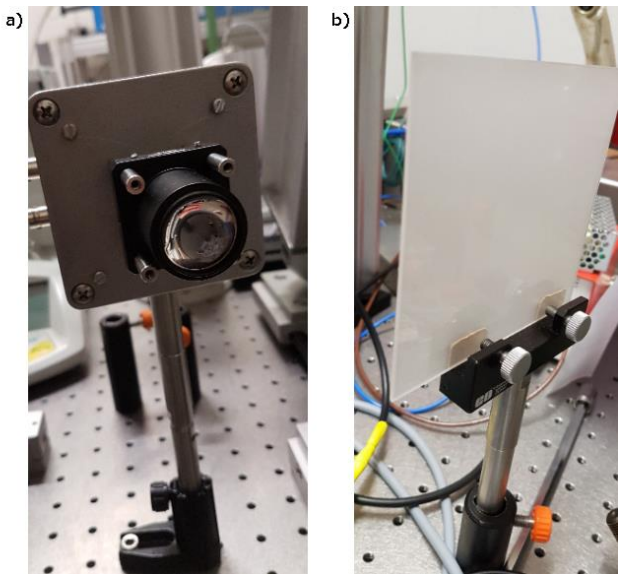

Fig. 47 (a) LED light source (b) Diffuser

3.2.1 Attached meshes

In the first set-up in order to focus mainly on the meshes woven structure characterised by porosity and roughness, they were carefully attached on a flat surface made of stainless steel, pressed by means of a steel ring with a diameter of 3 cm , side dimensions of 5x5 cm and thickness of 5 mm (Fig. 48). This allows to avoid flexing during droplet impact and air entrapment effect. The camera was angled at 60° with respect to the horizontal plane. Fig. 49 shows a picture of the first set-up.

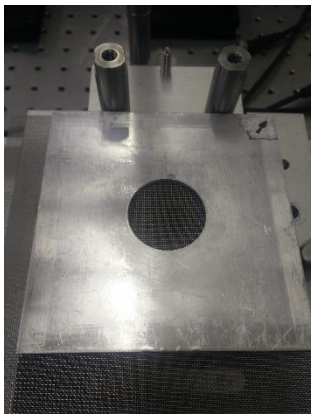

Fig. 48 Steel ring

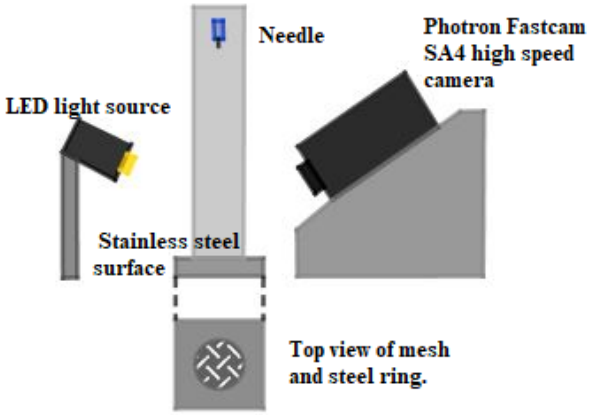

Fig. 49 Optical set-up schematic for the flat meshes configuration

Table 4, shows in detail the combination of parameters that was chosen for each experiment. Exploring different combinations of impact velocity, pore size and liquid properties, allows to achieve a better understanding of the distribution of the different outcomes.

Table 4 Experiments group - attached meshes

Test Group N°	Liquid	Height of Release (cm)	We	Oh	Needle Gauge	Mesh sample
1	Water	20.3	140.8	0.002	21	1-2-4-6-7-8
2	Water	44.3	330.1	0.002	26s	1-2-3-4-5-7
3	Water	80.3	628.2	0.002	21	1-2-4-6-7-8
4	Water	20.3	92.1	0.003	26s	1-2-3-4-5-7
5	Water	44.3	217.4	0.003	21	1-2-4-6-7-8
6	Water	80.3	400.8	0.003	26s	1-2-3-4-5-7
7	Acetone	20.3	255.7	0.002	21	1-2-4-6-7-8
8	Acetone	44.3	593.2	0.002	26s	1-2-3-4-5-7
9	Acetone	80.3	1027.3	0.002	21	1-2-4-6-7-8
10	Acetone	20.3	216.5	0.002	26s	1-2-3-4-5-7
11	Acetone	44.3	522.9	0.002	21	1-2-4-6-7-8
12	Acetone	80.3	918.5	0.002	26s	1-2-3-4-5-7
13	W&G	20.3	148.9	0.022	21	1-2-4-6-7-8
14	W&G	44.3	357.3	0.022	26s	1-2-3-4-5-7
15	W&G	80.3	647.0	0.021	21	1-2-4-6-7-8
16	W&G	20.3	87.4	0.029	26s	1-2-3-4-5-7
17	W&G	44.3	174.2	0.031	21	1-2-4-6-7-8
18	W&G	80.3	317.5	0.032	26s	1-2-3-4-5-7

3.2.2 Suspended meshes

In the second configuration, a portion of the mesh was suspended using initially 2 clamped rings with a 20 mm inner diameter, side dimensions of 5x5 cm and thickness of 5 mm. The rings are characterised by an aperture of 10 mm which allows to visualise and record the process with the camera as it is shown in **Fig. 50**.

Fig. 50 Steel rings with 1 cm aperture

The mesh was compressed between the 2 clamped rings with a screw per corner to maintain the adhesion of the mesh and reduce the vertical movement. It was observed that at higher impact velocities a small vertical movement of the mesh occurred after the impact of the droplet. The amplitude of the oscillation increases with the impact velocity but decreases with the wire diameter . To verify if the amplitude of the oscillation can influence the final outcome, some of the experiments were repeated using other 2 rings with diameters of 15 mm and 25 mm respectively, which offered smaller and larger unclamped area for the suspended mesh compared to the original case. For this set-up the camera was located parallel respect to the horizontal plane (Fig. 51).

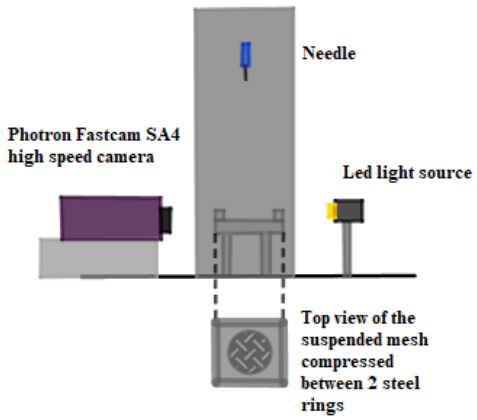

Fig. 51 Optical set-up configuration suspended meshes

Table 5 shows in the details the experiment groups and the combinations of different initial parameter done for the suspended mesh set-up.

Table 5 Experiments group-suspended meshes

Test Group N°	Liquid	Height of Release (cm)	We	Oh	Needle Gauge	Mesh sample
1	Water	20.3	129.2	0.002	21	1-2-4-5-6-7-8
2	Water	44.3	282.6	0.002	26s	1-2-4-5-6-7-8
3	Water	80.3	475.0	0.002	21	1-2-4-5-6-7-8
4	Water	20.3	89.7	0.003	26s	1-2-4-5-6-7-8
5	Water	44.3	209.7	0.003	21	1-2-4-5-6-7-8
6	Water	80.3	359.9	0.003	26s	1-2-4-5-6-7-8
7	Acetone	20.3	244.1	0.002	21	1-2-4-5-6-7-8
8	Acetone	44.3	513.7	0.002	26s	1-2-4-5-6-7-8
9	Acetone	80.3	830.4	0.002	21	1-2-4-5-6-7-8
10	Acetone	20.3	190.7	0.002	26s	1-2-4-5-6-7-8
11	Acetone	44.3	396.7	0.002	21	1-2-4-5-6-7-8
12	Acetone	80.3	641.1	0.002	26s	1-2-4-5-6-7-8
13	W&G	20.3	163.6	0.022	21	1-2-4-5-6-7-8
14	W&G	44.3	323.4	0.022	26s	1-2-4-5-6-7-8
15	W&G	80.3	550.3	0.023	21	1-2-4-5-6-7-8
16	W&G	20.3	121.9	0.024	26s	1-2-4-5-6-7-8
17	W&G	44.3	272.5	0.024	21	1-2-4-5-6-7-8
18	W&G	80.3	462.3	0.024	26s	1-2-4-5-6-7-8

3.3 Image Analysis

The pixel size and corresponding physical dimension was calibrated with the Photron Fastcam video processor, knowing the size of the aperture on the steel ring (10 mm). 1 pixel has the dimension of 0.0658 mm. After the calibration, the length of the 1 cm aperture was measured 5 times giving the result shown in **Fig. 52**.

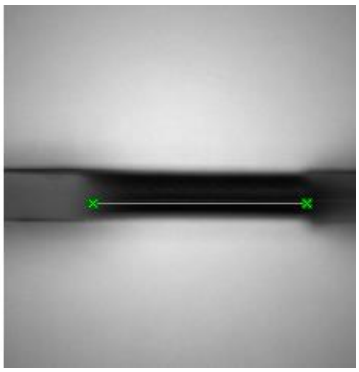

Test N°	Aperture length (mm)
Test 1	9.34±0.13
Test 2	9.73±0.13
Test 3	10.00±0.13
Test 4	9.73±0.13
Test 5	10.06±0.13

Fig. 53 Pixel/mm calibration with the Photron Fastcam video processor

A purpose-built image processing algorithm was developed using MATLAB to measure the droplet initial diameter and the maximum spreading area of the impact. Impact velocity was also determined by measuring the rate of displacement of the droplet's centre of mass from the video images Fig. 54 and Fig. 55 show an example of the image analysis for the measurement of the falling drop's diameter. The image processing algorithm follows the droplet fall for a certain number of frames. The measure of the droplet diameter is given by the average of all the measurements taken in each frame. Following the trajectory of the droplet centre of mass and taking in account the tilted angle of the camera, the code is capable to compute the impact velocity the droplet.

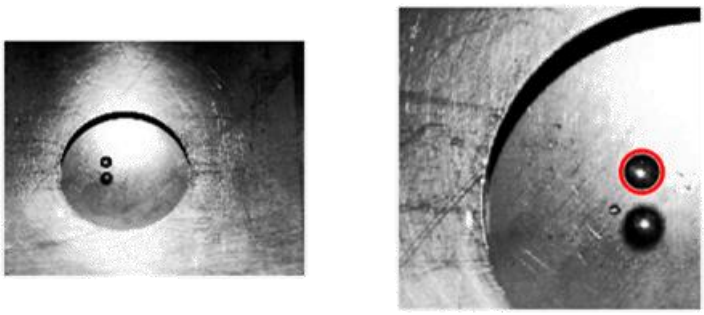

Fig. 54 MATLAB Image analysis flat meshes

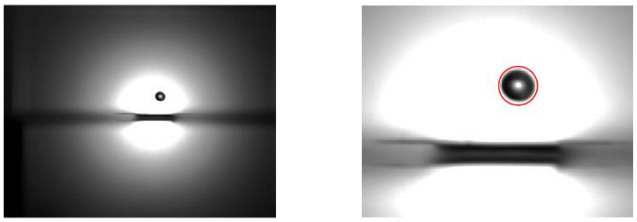

Fig. 55 MATLAB Image analysis suspended meshes

The MATLAB code, which operates thanks to a contour detection with threshold on grey level gradient, was validated by repeating the impact using a glass marble having a diameter of 3 mm. Realising the marble from a high of 22 cm and repeating the impact for 5 times, we obtained the results in **Table 6** which prove the accuracy of the code. The uncertainty on the measure is given by the pixel/mm calibration.

Table 6

Set of 5 typical measurements to validate the MATLAB code for a glass marble with a dimeter of 3 mm

Case N°	Velocity (m/s)	Marble Diameter (mm)
1	1.80	2.9±0.13
2	1.77	2.8±0.13
3	1.87	2.9±0.13
4	1.78	2.9±0.13
5	1.80	2.9±0.13

In the case of the suspended mesh, an estimation of the liquid penetration is given, computing the volume of the single droplet ejected from the surface after the impact or subtracting the volume of the remaining cap above the mesh from the initial volume Fig. 56 (a-b).

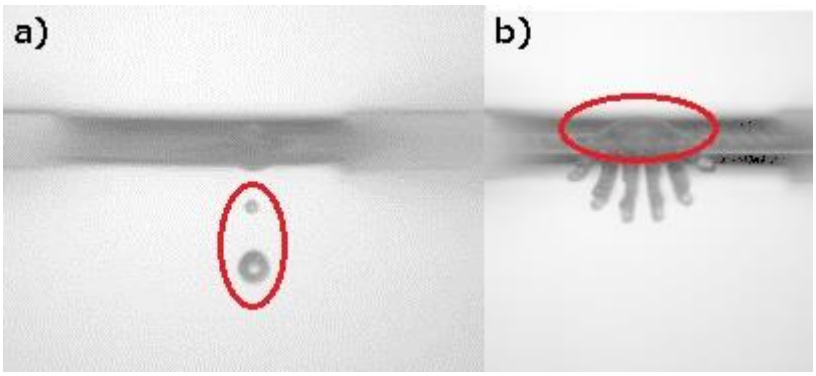

Fig. 56 Liquid penetration on the suspended mesh.

The initial volume of the droplet is calculated from the droplet radius, assuming that the droplet has a perfectly spherical shape. Consequently, in the case shown in Fig. 56 (a), the liquid penetration will be given by

$$V_{penetration} = \sum_{i=1}^{n} \frac{3}{4}\pi r_i^3 \qquad 3.1$$

Which corresponds to the sum of all the single droplets ejected below the mesh. In the case of Fig. 56 (b), due to the complexity of the outcome, it is not possible to calculate the volume of the droplets ejected below the mesh therefor the liquid penetration will be given by

$$V_{penetration} = V_i - V_{cap} = \frac{3}{4}\pi r^3 - \pi h^2 (r_c - \frac{h}{3}) \qquad 3.2$$

Where V_i and V_{cap} are respectively the initial volume of the droplet and the volume of the cap left above the mesh, and r_c and h , the radius and the height of the cap.

3.4 Error Analysis

Both in the case of the flat mesh and the suspended mesh, each experiment was repeated 5 times to have a statistical approach and avoid human error. The following analysis shows the error given by the measurement of droplet diameter and impact velocity.

3.4.1 Attached meshes error analysis

Table 7 shows in detail the standard deviation (σ) of the impact velocity, We and Oh numbers for the case of the attached meshes, considering the three liquids, the different needles and the height of release**.**

Table 7

Error analysis of impact velocity for water, acetone and water & glycerol

Height of Release (cm)	Needle Gauge	Liquid	Mean Velocity (m/s)	σ Velocity (m/s)	σ We	σ Oh
20.3	21	Water	1.8	0.17	24.26	0.00003
44.3	21	Water	2.9	0.11	25.22	0.00004
80.3	21	Water	3.9	0.16	59.20	0.00004
20.3	26s	Water	1.9	0.11	10.64	0.00005
44.3	26s	Water	2.9	0.14	28.17	0.00007
80.3	26s	Water	3.9	0.16	39.12	0.00004
20.3	21	Acetone	1.9	0.13	33.07	0.00005
44.3	21	Acetone	2.9	0.17	96.72	0.00005
80.3	21	Acetone	3.9	0.17	110.05	0.00003
20.3	26s	Acetone	1.9	0.13	33.50	0.00003
44.3	26s	Acetone	2.9	0.17	70.11	0.00004
80.3	26s	Acetone	3.7	0.20	123.33	0.00007
20.3	21	W&G	1.8	0.07	11.61	0.00011
44.3	21	W&G	2.7	0.10	30.55	0.00027
80.3	21	W&G	3.7	0.07	28.10	0.00025
20.3	26s	W&G	1.8	0.12	12.85	0.00113
44.3	26s	W&G	2.7	0.15	19.47	0.00136
80.3	26s	W&G	3.8	0.11	40.84	0.00182

Table 8 shows in detail the error analyses on the droplet diameter dimension for the first group of experiments. The height of release is not taken into account because it does not influence the droplet dimension.

Table 8

Error analysis of initial diameter for water, acetone and W&G

Needle Gauge No.	Liquid	Mean Diameter (mm)	σ (mm)
21	Water	3.0	0.12
26 s	Water	1.9	0.09
21	Acetone	2.0	0.11

26 s	Acetone	1.7	0.10
21	W&G	2.9	0.06
26 s	W&G	1.5	0.18

To further confirm the repeatability of the experiments, Table 9-Table 11 show an example of a typical set of 5 measurements for water, acetone and water & glycerol, given the same initial condition.

Table 9

Set of 5 typical measurements to confirm the repeatability for water with gauge No. 21 and high of release equal to 44.3 cm

Case N°	Velocity (m/s)	Droplet Diameter (mm)	We	Oh
1	2.86	2.9	330.85	0.0022
2	3.00	3.0	369.31	0.0021
3	2.71	3.0	308.24	0.0021
4	2.81	2.9	320.29	0.0021
5	2.70	2.9	296.26	0.0022

Table 10

Set of 5 typical measurements to confirm the repeatability for acetone with gauge No. 21 and high of release equal to 44.3 cm

Case N°	Velocity (m/s)	Droplet Diameter (mm)	We	Oh
1	2.83	1.78	490.63	0.0017
2	2.72	1.96	498.20	0.0016
3	2.74	1.95	507.67	0.0016
4	3.15	1.86	634.57	0.0016
5	2.76	1.86	488.71	0.0016

Table 11

Set of 5 typical measurements to confirm the repeatability for water & glycerol with gauge No. 21 and high of release equal to 44.3 cm

Case N°	Velocity (m/s)	Droplet Diameter (mm)	We	Oh
1	2.96	2.88	421.39	0.0017
2	2.95	2.95	427.64	0.0016
3	2.73	2.88	358.52	0.0016
4	3.00	3.08	461.98	0.0016
5	3.06	2.86	447.30	0.0016

3.4.2 Suspended meshes error analysis (ring 20 mm inner diameter)

The same analysis was done for the case of the suspended meshes. Table 12 and Table 13 show respectively the error given on the impact velocity and drop diameter. In the first set of the experiments, a portion of the mesh was suspended using a ring with a 20 mm inner diameter.

Table 12

Error analysis of impact velocity for water, acetone and water & glycerol suspended meshes

Height of Release (cm)	Needle Gauge	Liquid	Mean Velocity (m/s)	σ (m/s)	σ We	σ Oh
20.3	21	Water	1.86	0.03	4.9	0.00002
44.3	21	Water	2.76	0.03	6.9	0.00001
80.3	21	Water	3.59	0.06	30.2	0.00005
20.3	26s	Water	1.78	0.03	4.5	0.00003
44.3	26s	Water	2.70	0.04	5.9	0.00000
80.3	26s	Water	3.53	0.06	12.0	0.00000
20.3	21	Acetone	1.83	0.01	4.4	0.00001
44.3	21	Acetone	2.66	0.08	30.9	0.00000
80.3	21	Acetone	3.39	0.06	37.3	0.00002
20.3	26s	Acetone	1.80	0.08	19.6	0.00002
44.3	26s	Acetone	2.61	0.06	15.2	0.00002
80.3	26s	Acetone	3.33	0.10	40.3	0.00003
20.3	21	W&G	1.86	0.01	3.1	0.00013
44.3	21	W&G	2.71	0.02	8.7	0.00023
80.3	21	W&G	3.57	0.03	11.9	0.00007
20.3	26s	W&G	1.81	0.01	6.6	0.00063
44.3	26s	W&G	2.67	0.02	6.5	0.00019
80.3	26s	W&G	3.49	0.04	12.8	0.00006

Table 13 Error analysis of initial diameter for water, acetone and W&G, suspended meshes

Needle Gauge No.	Liquid	Mean Diameter (mm)	σ (mm)
21	Water	2.72	0.07
26 s	Water	2.10	0.04
21	Acetone	2.10	0.03
26 s	Acetone	1.69	0.04
21	W&G	2.66	0.08
26 s	W&G	2.27	0.06

To further confirm the repeatability of the experiments, Table 14- Table 16 show an example of a typical set of 5 measurements for water, acetone and water & glycerol, given the same initial condition.

Table 14

Set of 5 typical measurements to confirm the repeatability for water with gauge No. 21 and high of release equal to 44.3 cm

Case N°	Velocity (m/s)	Droplet Diameter (mm)	We	Oh
1	2.75	2.92	300.64	0.0022
2	2.74	2.71	277.24	0.0023
3	2.76	2.71	282.06	0.0023
4	2.72	2.72	273.45	0.0023
5	2.72	2.71	274.29	0.0023

Table 15

Set of 5 typical measurements to confirm the repeatability for acetone with gauge No. 21 and high of release equal to 44.3 cm

Case N°	Velocity (m/s)	Droplet Diameter (mm)	We	Oh
1	2.65	2.12	509.82	0.0015
2	2.60	2.11	492.36	0.0015
3	2.66	2.12	515.97	0.0015
4	2.66	2.13	514.50	0.0015
5	2.61	2.11	494.64	0.0015

Table 16

Set of 5 typical measurements to confirm the repeatability for water & glycerol with gauge No. 21 and high of release equal to 44.3 cm

Case N°	Velocity (m/s)	Droplet Diameter (mm)	We	Oh
1	2.71	2.73	334.69	0.0221
2	2.70	2.70	328.97	0.0222
3	2.70	2.71	331.13	0.0222
4	2.72	2.73	336.05	0.0221
5	2.72	2.71	335.27	0.0222

3.4.3 Spreading analysis

Measurements of droplet spreading diameters we made (d) as a function of time t. The dimensionless diameter and time are defined as [21].

$$d(t)^* = \frac{d(t)}{d_o} \qquad 3.3$$

$$t^* = t \cdot \frac{v_i}{d} \qquad 3.4$$

Where d_o is the droplet initial diameter, d(t) the time-varying diameter after impact and v_i the impact velocity. The measurement of the spreading evolution was done for water droplets impacting on meshes with pore sizes equal of 25, 100 and 200 μm. Fig. 57 shows the spreading evolution of a droplet of water impacting on a mesh with pore size equal to 25 μm.

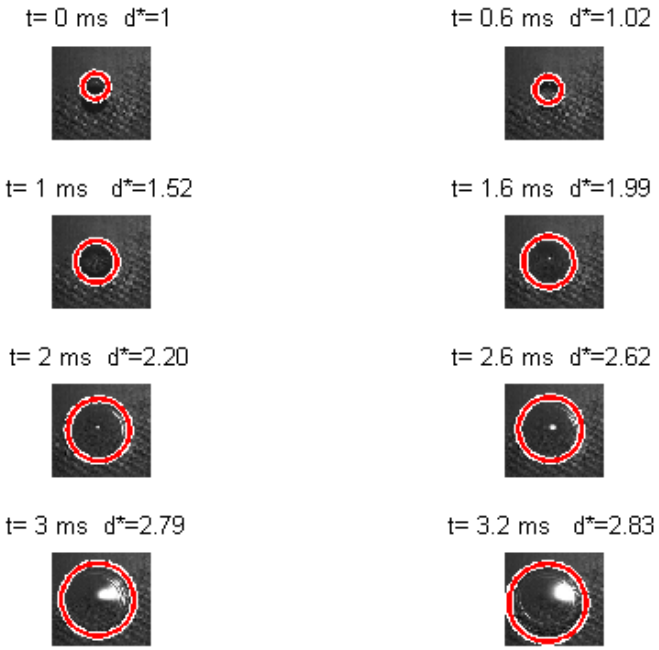

Fig. 57 Spreading analysis for water droplet impact at $d_i = 3.0mm$ and $v_i = 2.87\frac{m}{s}$ on a mesh with $D_p = 25\ \mu m$

The standard deviation on the maximum spreading for all the cases is about 4%.

4 Experiments and Results

A first attempt of the experiments in the case of attached meshes, shown the results reported in Fig. 58 and Fig. 59.

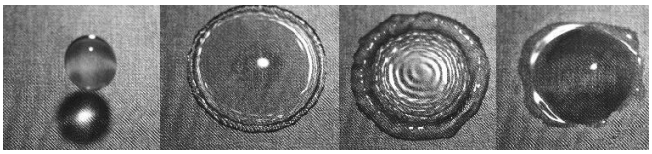

Fig. 58 Deposition outcome: d = 3,019 mm, v_i = 1,76 m/s, D_p = 25μm, D_w = 25μm

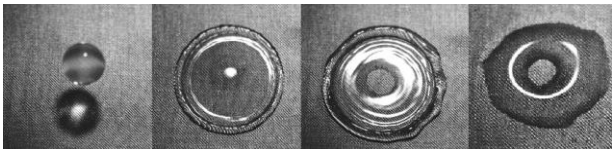

Fig. 59 Partial imbibition outcome: d = 3,065 mm, $\boldsymbol{v_i}$= 1,71 m/s, $D_p = D_w$ = 25μm. Same impact parameters, different outcome.

The experiments shown in Fig. 58 and in Fig. 59 were done using the same initial parameters in terms of impact velocity, liquid properties and mesh pore dimension. Nevertheless, a different outcome was observed. In the first sequence (Fig. 58), the droplet, after the impact, remains completely above the surface after the spreading and the recoiling. In Fig. 59 it is possible to observe that during the recoiling, part of the liquid penetrates below the surface. The penetration is possible due to the woven structure of the mesh that gives a pathway between the metallic mesh and the solid surface to whom it is attached, allowing part of the droplet to flow inside as it is shown in Fig. 60.

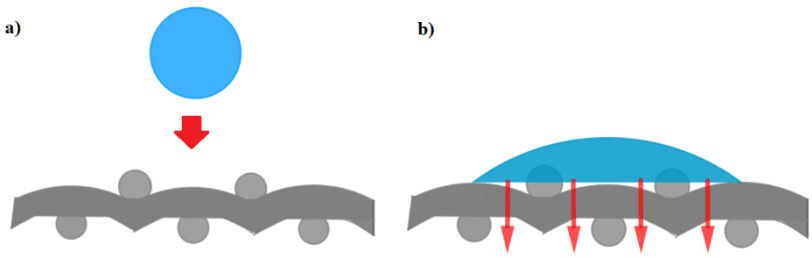

Fig. 61 a) Droplet impacting on the woven mesh b) Droplet penetrating below the mesh through the pathway left by the woven structure

The first results obtained show clearly that a more accurate description of the phenomenon is required to clarify for which condition it is possible to observe a specific outcome or a transition region between a deposition of the droplet above the surface or a partial penetration inside the pores.

4.1 Attached meshes

By observing the result of the experiments, it was possible to identify 6 different outcomes.

For a low velocity impact, these outcomes are a deposition, a partial imbibition and a penetration.

For a high velocity impact, the same outcomes are observable, but it is possible to have a transition to a splash, which is still characterised by a final deposition, partial imbibition and penetration.

Whereas for the deposition and the partial imbibition, both in the case of impact with splash or without splash, the time scale is about 20 ms, in the case of the penetration the process is much faster, with a duration of 4 ms.

It was also observed that the splash regime linked to the final deposition outcome is not very frequent, due to the fact that a higher impact velocity will enhance the probability of a penetration of the liquid below the mesh.

4.1.1 Regime definition

The main outcomes are shown in the video sequences below reported in Fig. 62.

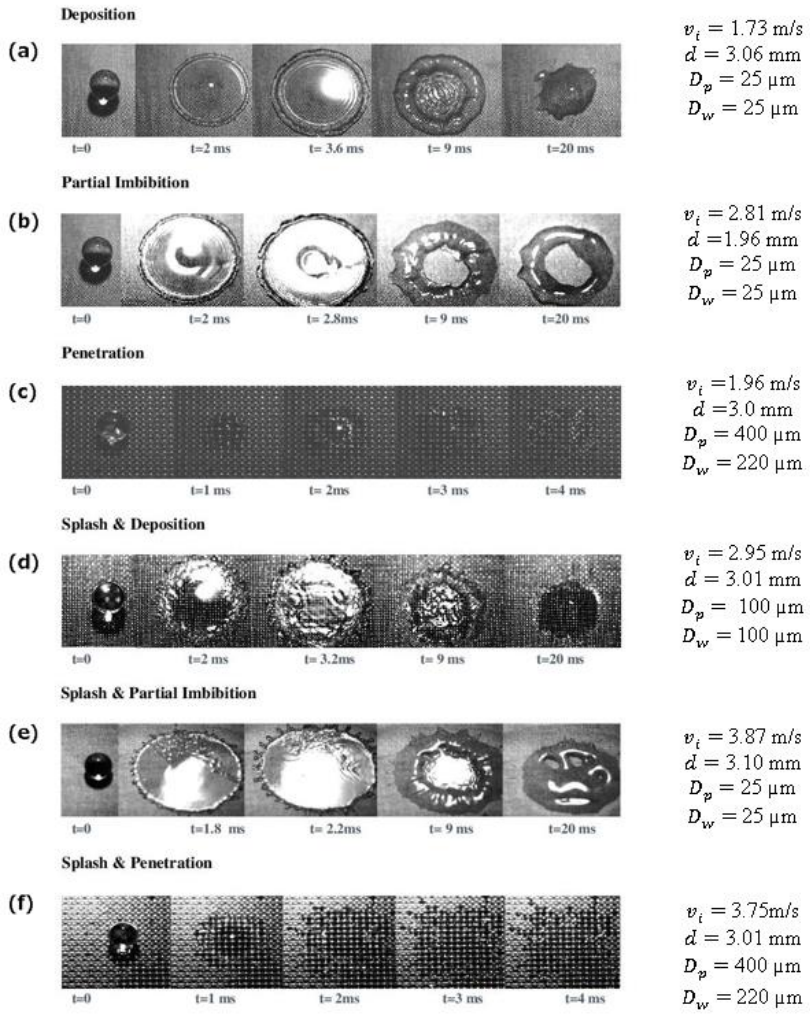

Fig. 62 Impact outcomes for water droplets. (a) Deposition: The droplet impacts on the substrate and after the spreading and recoiling the liquid remains deposited over the surface with no penetration. (b) Partial imbibition: The droplet impacts on the substrate. During the spreading and the recoiling part of the liquid penetrates below the surface. (c) Penetration: The droplet impacts on the substrates. Due to the larger dimension of the pores, no spreading occurs and the complete penetration process is almost instantaneous. (d) Splash & Deposition: The droplet impacts on the surface with a higher velocity, after the splash all the liquid remain deposited on the surface. (e) Splash & partial imbibition: The droplet impacts on the surface with a higher velocity, after the splash, part of the liquid penetrates below the surface. (f) Splash & Penetration: The droplet impacts on the surface with a higher velocity and due to the larger dimension of the pore, after the splash all the liquid penetrates below the surface.

In Fig. 62(a), the deposition outcome is characterised by the fact that, in a range of 15-20ms after the drop impacts on the substrate, and after the spreading and the

recoiling, it is still possible to observe a liquid pancake on the surface without a proper imbibition, and the droplet recoils in an asymmetrical shape.

At time t= 0 the droplet impacts on the surface and the spreading phase begins. At t= 3.6 ms, the droplet reaches the maximal spreading diameter having an almost perfect circular shape. The recoiling phase begins. At t=9 ms, during the recoiling it is still not possible to detect an imbibition of the liquid under the surface. At t=20 ms it is possible to observe the final liquid pancake having an asymmetrical shape. Removing the mesh to clean the substrate, no liquid is detected underneath which confirms that no penetration occurred.

The partial imbibition, in Fig. 62 (b), can be considered as a transition outcome in which starting from the spreading and mainly during the recoiling process after the impact, part of the liquid penetrates under the surface and part of the liquid is deposited on the substrate in a time range of 15-20 ms.

At time t= 0 the droplet impacts on the surface and the spreading phase begins. At t= 2.8 ms, the droplet reaches the maximal spreading diameter showing already a partial imbibition at the centre of the spreading. The recoiling phase begins. At t=9 ms, it is possible to observe clearly the formation of a crater at the centre of the droplet. At t=20 ms the recoil phase ends.

In the case of penetration, in Fig. 62(c), the liquid penetrates completely through the mesh pores after the impact (2-4 ms), consequently it is not possible to distinguish a spreading or a recoiling phase.

In Fig. 62 (d), at time t= 0 the droplet impacts on the surface and it is possible to detect a splash due to the higher impact velocity, the spreading phase begins. At t= 3.2 ms, the droplet reaches the maximal spreading diameter. The recoiling phase begins. At t=7.2 ms, during the recoiling it is still not possible to detect an imbibition of the liquid under the surface. At t=20 ms it is possible to observe the final liquid pancake.

In Fig. 62 (e), at time t= 0 the droplet impacts on the surface showing a splash outcome and the spreading phase begins. At t= 2.2 ms, the droplet reaches the maximal spreading diameter showing already a partial imbibition located at the upper part of the droplet. The recoiling phase begins. At t=9 ms, it is possible to observe the formation of a small craters in the upper part of the droplet. At t=20 ms the recoil phase ends.

Finally, in Fig. 62 (f), for the splash & penetration outcome, the liquid penetrates completely through the mesh pores after the impact in a range of time between 2 and 4 ms, consequently it is not possible to distinguish a spreading or a recoiling phase.

Focusing on the transition between deposition and partial imbibition and according to the study of Ryu et al. [78], the penetration dynamics of water droplet through a mesh can be explained with the balance between the penetration pressure and the resisting capillary force. This balance can be written as $C_0 \rho v_i^2 = p_c$ with C_0 being a proportional constant. From this balance they obtained the equation to find the velocity threshold for which imbibition occurs (C_0=2.87).

In Fig. 63, the threshold equation of Ryu et al. [78] is used to point out at the regime boundary and separate our results in two different regions. The attempt of using the equation to separate the two different regimes shows that there is still an overlap of the two different regions which leads to the conclusion that the results from Ryu et al. [78] are not in perfect agreement with ours. In the experiments of Ryu et al. [78], the meshes are suspended and not attached to another solid surface, as a results the threshold they described, cannot be perfectly adapt to our case.

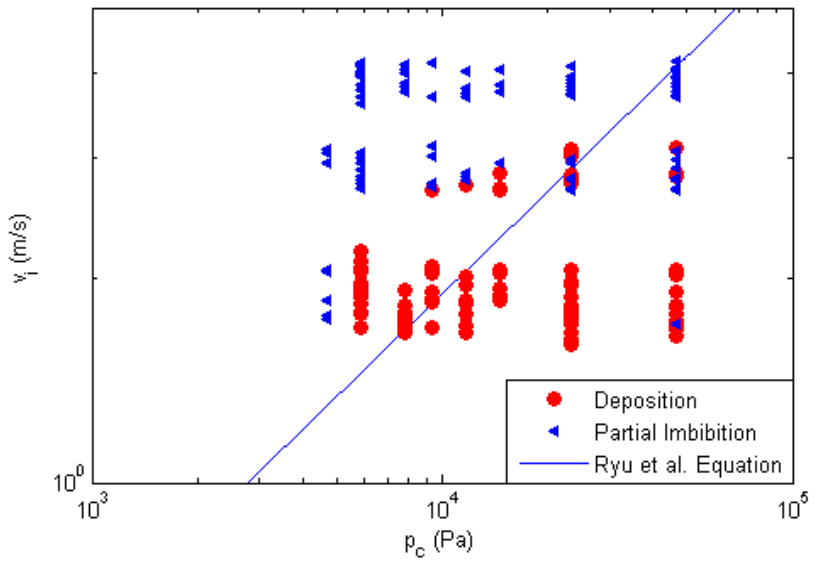

Fig. 63 Threshold velocity for deposition-imbibition (for water, d ranging between 1.5 and 3mm) : comparison with the equation of Ryu et al. [78]

Lorenceau et al. [73] studied the impact of a droplet on a surface pierced by a single hole, with varying diameters ranging from 0.13–0.45 mm, and identified a critical speed above which the droplet is not entirely captured by the plate but passes

through it after the impact. Their analysis compared the stagnation pressure in the droplet after impact to the capillary pressure and shear force opposing the movement of liquid through the pore.

Fig. 64 shows the graph pointing at the threshold velocity limit for which the droplet is captured by the surface or ejected. The thin line curve representing the velocity threshold for the droplet capture is given by the equation

$$Re^* = \frac{5.1We^*}{We^* - 3.6} \qquad 4.1$$

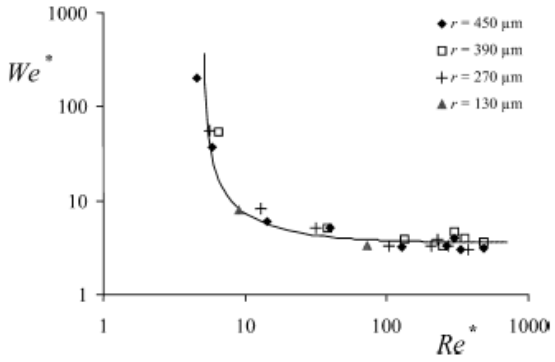

Fig. 64 Threshold velocity for capture [73]

It is possible to compare this result to our case, considering the regimes of the deposition and the partial imbibition. In fact, the range in which Lorenceau et al. [73] operated focuses only on the threshold for which part of the liquid droplet is not entirely captured by the plate but partially passes through it, without delimiting a region for a splash regime or a complete penetration of the droplet.

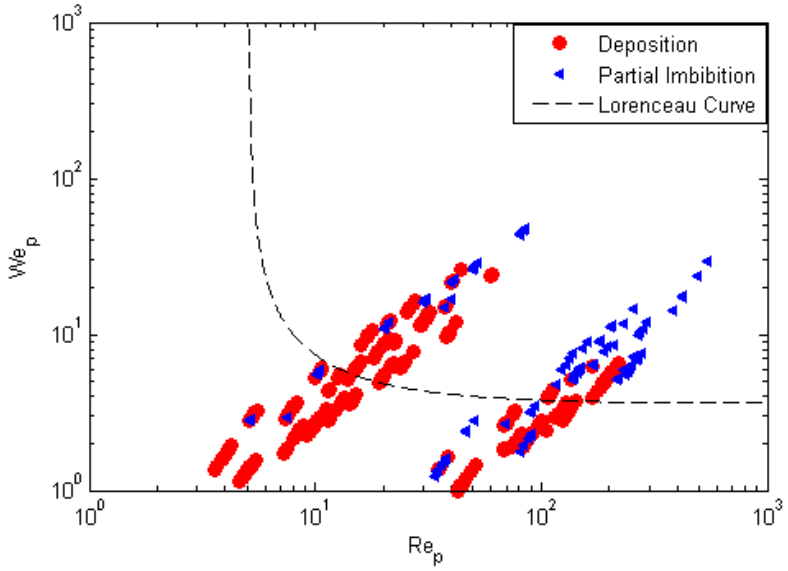

Fig. 65 Threshold velocity for capture (water, d ranging between 1.5 and 3mm): comparison with our results (attached meshes) [73]

The curve defined by Lorenceau et al. [73], fails to perfectly describe the separation between the regimes. The experiments of Lorenceau et al. [73], aims to analyse the impact of a droplet on a plate with a single hole, consequently the threshold they define to separate the regimes, predictabily cannot be perfectly applicable in our case.

Focusing again on our results which involve also the complete penetration phenomenon and higher impact velocities, we can make another consideration. The stagnation pressure when a droplet impacts on a solid surface is given by

$$P_s = \frac{1}{2}\rho v_i^2 \qquad 4.2$$

The capillary pressure resisting liquid penetration into a pore with opening size D_p is

$$P_c = \frac{2\sigma}{R_p} = \frac{4\sigma}{D_p} \qquad 4.3$$

While the viscous shear stress can be estimated as being of order of magnitude

$$\tau \sim \mu \frac{v_i}{D_p} \qquad 4.4$$

In the limit of low velocity ($v_i \to 0$) viscous forces are negligible and capillary forces dominate. For liquid to penetrate a pore we require $P_s \gg P_c$, or,

$$We_p = \frac{\rho v_i^2 D_p}{\sigma} \gg 8 \qquad 4.5$$

alternatively, if the pore diameter is small ($D_p \to 0$), or liquid viscosity is large, viscous forces dominate. In that case we require for liquid penetration to occur that $P_s \gg \tau$, or

$$Re_p = \frac{\rho V D_p}{\mu} \gg 50 \qquad 4.6$$

Re_p and We_p are the Reynolds and Weber numbers respectively, based on the mesh pore diameter as a length scale. These represent the lower limits on the value of Re_p and We_p required for liquid penetration to occur. Fig. 66 shows the values of Re_p and We_p, for the cases where either liquid deposition or penetration was observed. Based on our results, the limits of We_p>8 and Re_p >50 demarcate the boundary between deposition and penetration.

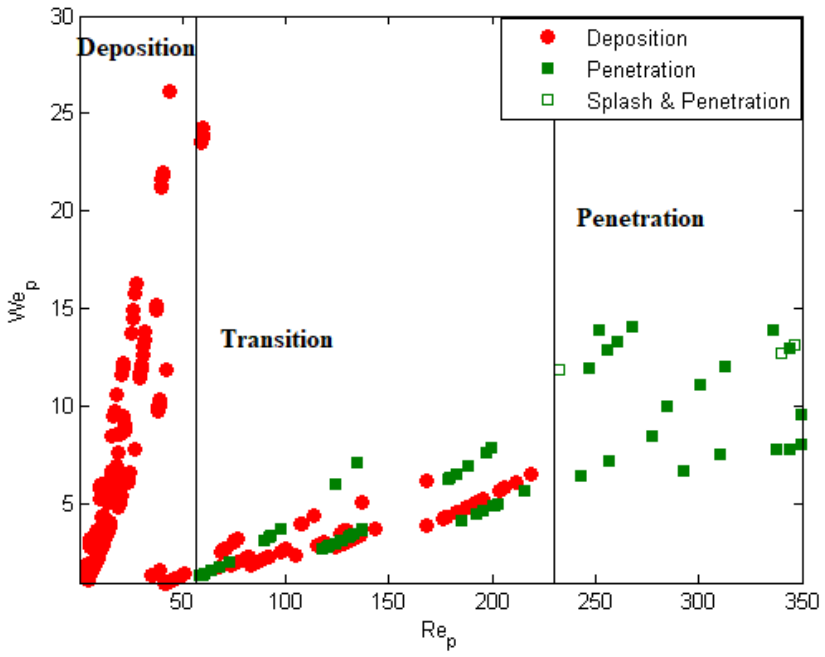

Fig. 66 Data distribution for water, acetone, water & glycerol (d ranging between 1.5 and 3mm) as a function of Re and We. Transition between deposition and penetration.

In the limit of small $Re_{p,}$ the dominant force is viscous shear so that droplets cannot penetrate into the pores and that the final outcome of impact is droplet deposition on the mesh. At larger Re_p (Re_p>50) viscous forces are no longer the dominant factor and penetration is controlled by a balance of capillary and inertial forces. For 50<Re_p<230, a transition region occurs in which both capillary and inertial forces may affect penetration. For $Re_p > 230$, the only observable outcome is the penetration and inertial forces are dominant.

This analysis is limited to the range of data achievable from the experimental conditions. For example, in the case of the transition region, there is no data for We_p>10 and it not possible to determine if the deposition or penetration domain could be extended also to this area.

Comparing our results to the study of Ryu et al. [78] and Lorenceau et al. [73] we have to remark that in the case of Ryu et al. [78] the threshold velocity is related to water droplet and in the case of Lorenceau et al. [73]. a lower range of impact velocity is taken in account. In both cases the complete penetration outcome and the splash regime are not observed. For this reason, it is suggested to find a different combination of parameter to define the regime separation for a more generic case.

4.1.1 Spreading analysis

Liquid penetration can also affect droplet spreading on top of the mesh. Impact dynamics were observed for droplets impacting on meshes with different pores dimensions (25, 100 and 200 μm) at three different impact velocities (1.8 m/s, 2.9 m/s and 3.9 m/s).

In order to plot the trend of the spreading in time, the dimensionless diameter D^* and time t^* were used. **Fig. 67**-**Fig. 74** show the spreading evolution calculated considering the average trend of 5 impact. The standard deviation value is round 4%.

Table 17-

Table 19 show the average measurement for the spreading evolution in time considering the different cases.

Table 17

Spreading evolution for water droplet $d = 3.00mm\ \ D_p = 25\mu m$

D_p	$v_i = 2\frac{m}{s}$		$v_i = 3\frac{m}{s}$		$v_i = 4\frac{m}{s}$	
$25\ \mu m$	d^*	t^*	d^*	t^*	d^*	t^*
	1.00±0.043	0.00	1.00±0.043	0.00	1.00±0.043	0.00
	1.01±0.043	0.12	1.03±0.043	0.19	1.04±0.043	0.26
	1.02±0.043	0.24	1.12±0.043	0.38	1.05±0.043	0.52
	1.15±0.043	0.37	1.24±0.043	0.57	1.71±0.043	0.78
	1.21±0.043	0.49	1.58±0.043	0.77	2.12±0.043	1.04
	1.43±0.043	0.61	1.84±0.043	0.96	2.58±0.043	1.30
	1.67±0.043	0.73	2.12±0.043	1.15	2.79±0.043	1.56
	1.84±0.043	0.85	2.39±0.043	1.34	3.07±0.043	1.82
	2.01±0.043	0.98	2.54±0.043	1.53	3.28±0.043	2.08
	2.13±0.043	1.10	2.91±0.043	1.72	3.41±0.043	2.34
	2.34±0.043	1.22	3.01±0.043	1.91	3.60±0.043	2.60
	2.52±0.043	1.34	3.12±0.043	2.10	3.71±0.043	2.86
	2.57±0.043	1.46	3.24±0.043	2.30		
	2.68±0.043	1.59	3.30±0.043	2.49		
	2.75±0.043	1.71				
	2.80±0.043	1.83				
	2.86±0.043	1.95				

Table 18

Spreading evolution for water droplet $d = 3.00mm\ \ D_p = 100\mu m$

D_p	$v_i = 2\frac{m}{s}$		$v_i = 3\frac{m}{s}$		$v_i = 4\frac{m}{s}$	
$100\ \mu m$	d^*	t^*	d^*	t^*	d^*	t^*
	1.01±0.043	0.00	1.00±0.043	0.00	1.00	0.00
	1.04±0.043	0.12	1.02±0.043	0.12	1.02	0.12
	1.06±0.043	0.24	1.36±0.043	0.24	1.22	0.24
	1.20±0.043	0.37	1.62±0.043	0.37	1.56	0.37
	1.28±0.043	0.49	1.90±0.043	0.49	1.91	0.49
	1.46±0.043	0.61	2.02±0.043	0.61	2.11	0.61
	1.86±0.043	0.73	2.07±0.043	0.73	2.21	0.73
	1.87±0.043	0.85	2.28±0.043	0.85	2.33	0.85
	1.97±0.043	0.98	2.71±0.043	0.98	2.39	0.98
	2.05±0.043	1.10	2.79±0.043	1.10	2.35	1.10
	2.23±0.043	1.22	2.88±0.043	1.22		
	2.32±0.043	1.34	2.85±0.043	1.34		
	2.31±0.043	1.46				

Table 19

Spreading evolution for water droplet $d = 3.00mm \;\; D_p = 200\mu m$

D_p	$v_i = 2\frac{m}{s}$		$v_i = 3\frac{m}{s}$		$v_i = 4\frac{m}{s}$	
$200\ \mu m$	d^*	t^*	d^*	t^*	d^*	t^*
	1.00	0.00	1.00	0.00	1.00	0.00
	1.07	0.12	1.05	0.12	1.05	0.12
	1.10	0.24	1.18	0.24	1.39	0.24
	1.22	0.37	1.35	0.37	1.60	0.37
	1.34	0.49	1.64	0.49	1.89	0.49
	1.47	0.61	1.88	0.61	2.20	0.61
	1.59	0.73	2.28	0.73	2.28	0.73
	1.82	0.85	2.42	0.85	2.26	0.85
	2.00	0.98	2.50	0.98		
	2.09	1.10	2.50	1.10		
	2.17	1.22				
	2.19	1.34				
	2.18	1.44				

Due to tilted angle of the camera, we can trace the spreading evolution just 4-6 ms after the impact. Looking at Fig. 67, it is possible to remark that given the same impact velocity, in the case of a porous surface with 100 µm porosity and above, the maximum spreading diameter will be lower.

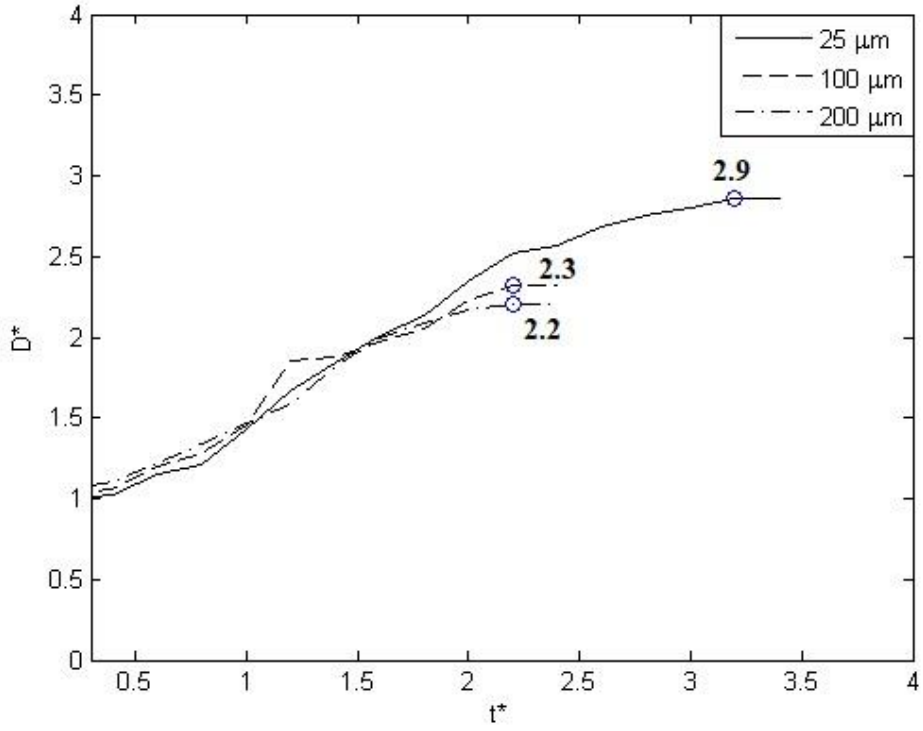

Fig. 67 Spreading analysis: Liquid: Water, Droplet initial diameter= 3 mm, Impact velocity= 1.87 m/s

This phenomenon can be explained assuming that with a larger pore size, the liquid will have more chances to get through the pores. Moreover, it is important to consider also the fact that at larger pore size, corresponds also a larger wire diameter. Consequently, there will be a higher energy loss during the spreading that will bring to a smaller maximum spreading diameter.

Sivakumar et al. [101] analysed water droplet impact on stainless steel structured surfaces. They focused on the evolution of the spreading diameter of the droplet on rough surfaces, comparing it to the evolution of the spreading diameter on a smooth surface. Fig. 68 shows a schematic of the structure they used for the experiments.

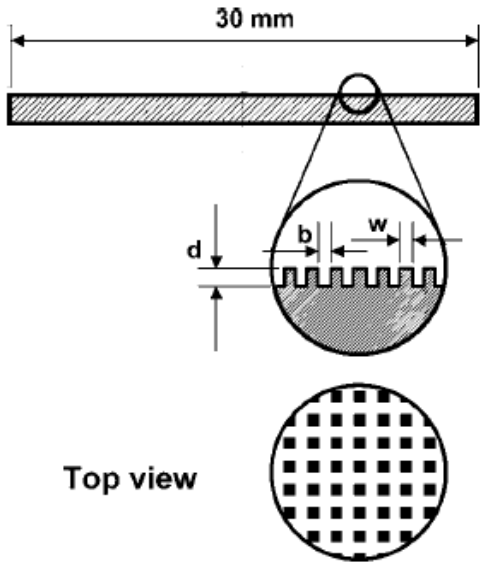

Fig. 68 Details of the geometrical parameters of the structured surface [101]

Looking at the surface geometry, they defined a roughness factor given by

$$r = 1 + \frac{4wd}{(w+b)^2} \qquad 4.7$$

Where d and w are respectively the height and the width of the square pillar and b the width of the groove. In the case of our research, the wire diameter can be considered as a roughness parameter, in fact it was observed that not only the pore dimension but also the wire diameter will affect the value of the maximum spreading diameter. Considering the roughness factor introduced by Sivakumar et al. [101], we can assume for our case that

$$d=w=D_w \qquad 4.8$$

where D_w is the wire diameter and

$$b=D_p \qquad 4.9$$

where D_p is the pore diameter.

As for our case, Sivakumar et al. [101], worked on water droplets with a diameter of 3 mm, impacting on a stainless steel surface. They observed that an increase of the value of d, and consequently of the roughness factor r, will lead to a smaller

spreading diameter. Fig. 69 shows the evolution of the spreading they obtained for different value of r, at We=80.2.

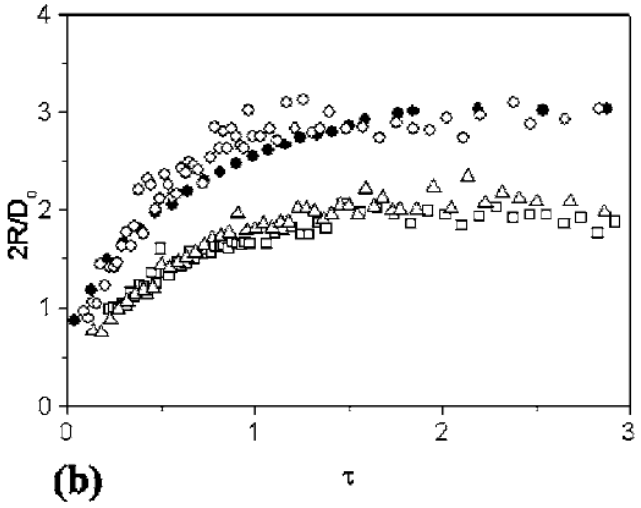

Fig. 69 Droplet spreading evolution. The open circles are for r= 1.33, the open triangles are for r= 2, the open squares are for r=2.67. The filled circles correspond to the spreading of a droplet on a smooth surface [101]

They also observed that, for the same roughness factor r, increasing the impact velocity (Weber number), the maximum spreading diameter will increase but it will always be lower respect to the case of droplet impact on a smoot surface. Their results are shown in Fig. 70.

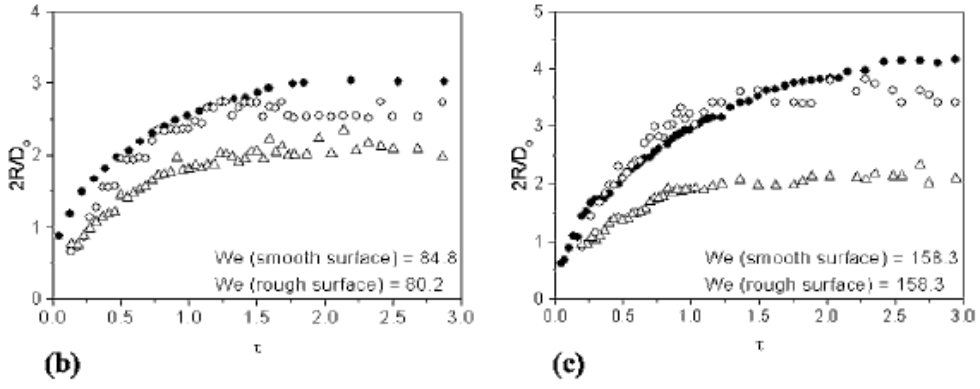

Fig. 70 Droplet spreading evolution for r=2. The open circles refer to the jet spreading and the open triangles refer to the lamella spreading. The filled circle correspond to the spreading of a droplet on a smooth surface[101]

We observed a similar behaviour in our results, in fact a higher value of r will lead to a smaller maximum spreading diameter as is shown in Fig. 71 .

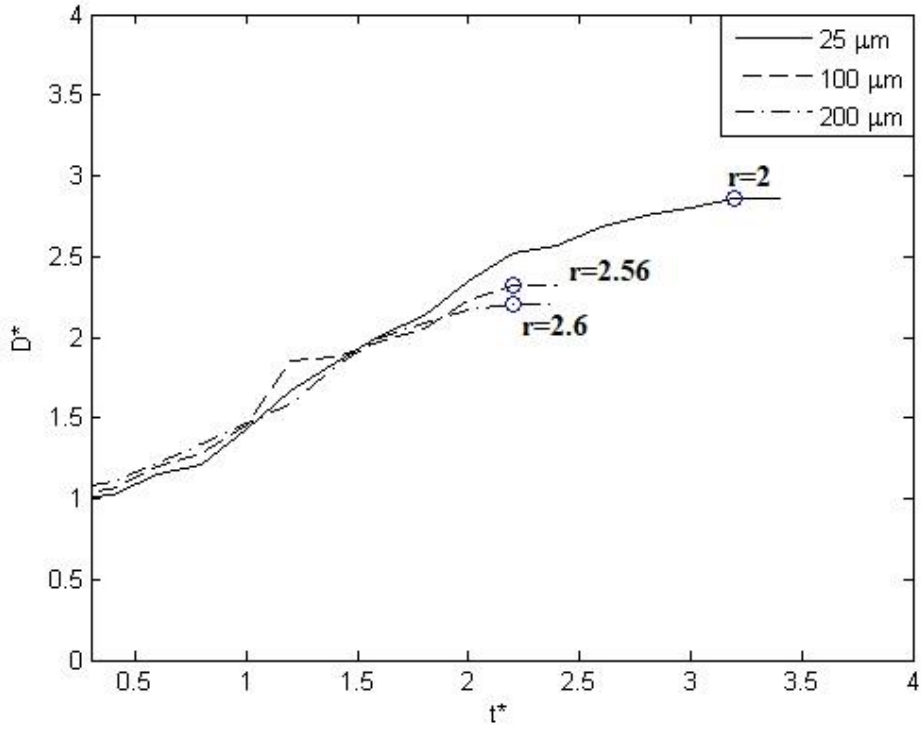

Fig. 71 Spreading analysis: liquid: water, droplet initial diameter= 3 mm, Impact velocity= 1.87 m/s at different values of r; We=140.8

Fig. 72 shows the spreading diameter for water droplets on a 25 µm mesh (r=2) at three different velocities. The spread factor increases with impact velocity, as is observed for droplet impact on a solid surface. For $v_i = 2\ m/s$, the maximum spread factor is about 2.7 whereas at $v_i = 4\ m/s$, the maximal spread factor is equal to 3.7. Table 20 lists the values of We_p for each of these velocities. For a 25 µm mesh We_p is always less than the critical value of 8, implying that there is no penetration into the mesh. Droplet impact dynamics are similar to those seen on an impermeable surface. The equation to describe the spreading evolution on a smooth surface is given by [24]

$$D_{max} = \frac{\sqrt{We+12}}{3(1-cos\theta_a)+4(\frac{We}{\sqrt{Re}})} \qquad 4.10$$

Were θ_a is the dynamic contact angle after the spread and D_{max} the maximum spreading diameter [24]. In this specific case, considering a water droplet of 3mm diameter and three impact velocities of 1.8; 2.9 and 3.9 m/s, the maximum spreading diameter on a smooth stainless-steel surface, would be given respectively

by 4, 4.6 and 5. The difference in maximum spreading diameter for a smooth surface and a porous surface will increase, increasing the size of the pores and the wire which will affect the roughness of the surface as well.

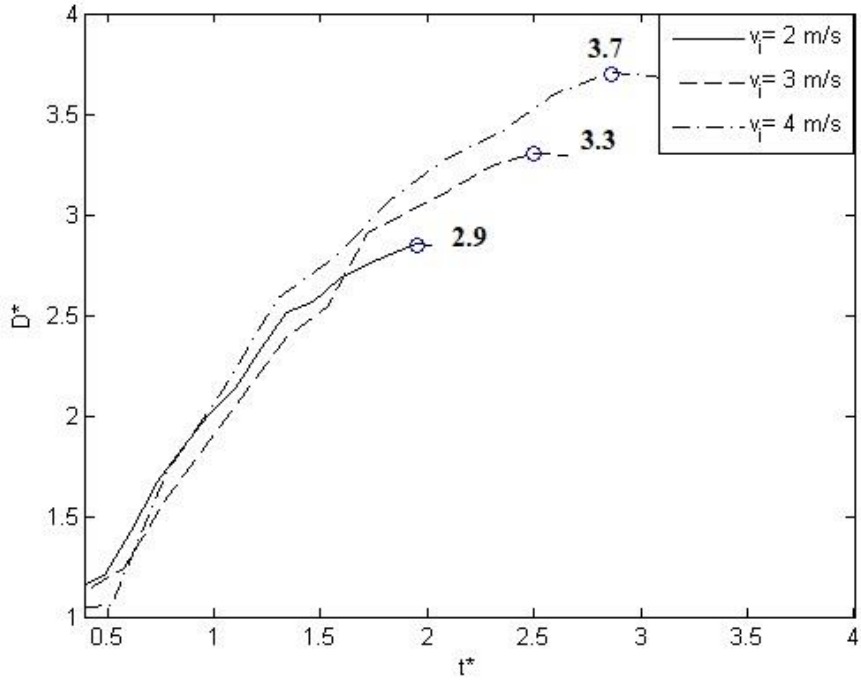

Fig. 72 Evolution of dimensionless spreading diameter with time for water droplets with $d = 3$ mm. $D_p = 25$ μm, $D_w = 25$ μm (r=2)

Fig. 73 and Fig. 74, show respectively droplet impact on a mesh with 100 μm and 200 μm pores.

In the case of droplet impact on a mesh of 100 μm, r=2.56 (Fig. 73), at the lowest velocity (1.8 m/s), the maximum spread factor is approximately 2.4. The spread factor is lower than it was on the 25 μm mesh as there will be a higher penetration of the liquid in the pores and the roughness factor is higher. At the same condition, in the case of droplet impact on a mesh of 200 μm (Fig. 74), the maximum spread factor is 2.2. As said, the weaker spread can be explained by two different reasons: (i) for a larger pore size, a higher percentage of liquid will penetrate below the surface leading to a lower spreading diameter; (ii) at a larger pore size corresponds also a larger wire diameter, consequently during the spreading, the greater "roughness" will enhance the viscous dissipation leading to a smaller spreading diameter.

In fact, the 200 μm pore size mesh in which case the maximum spreading diameter is lower, is characterized by a wire diameter of 125 μm , whereas the 25 μm pore size mesh has a wire diameter of only 25 μm.

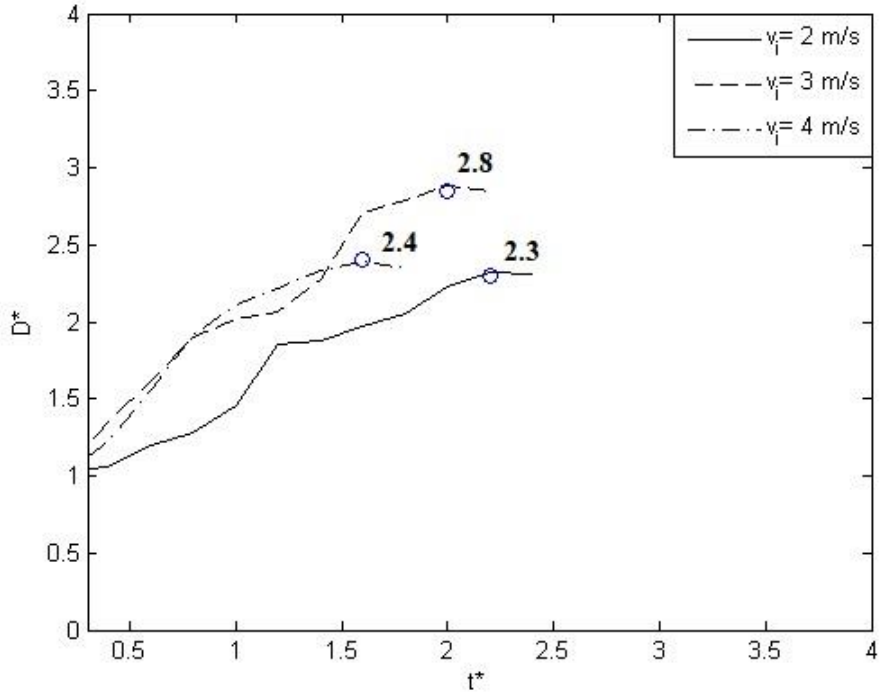

Fig. 73 Evolution of dimensionless spreading diameter with time for water droplets with $d = 3$ mm.$D_p = 100$ µm, $D_w = 65$ µm. (r=2.54)

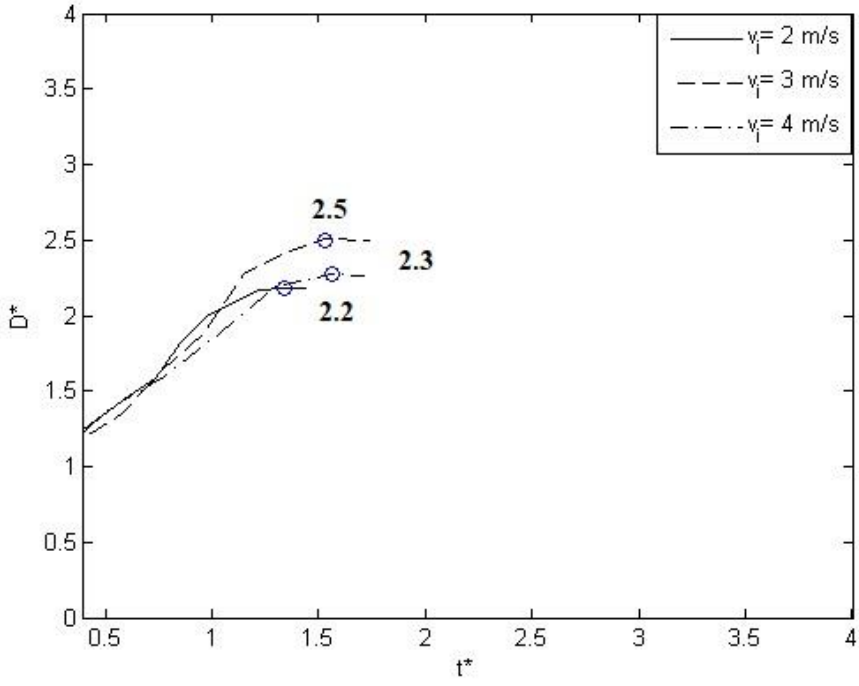

Fig. 74 Evolution of dimensionless spreading diameter with time for water droplets with $d = 3$ mm $D_p = 200$ µm, $D_w = 125$ µm. (r=2.6)

For a mesh with 200 µm pores and We_p= 9.1 at the lowest impact velocity, this is barely above the limit for penetration to occur. The reduced droplet spreading in this case is therefore most probably the result of surface roughness due to the larger wire diameter.

When the impact velocity is increased to 2.9 m/s the droplet spread increases, though it is less than it was on a 25 µm mesh (compare Fig. 72 and Fig. 74). For this case We_p= 22.5 (see Table 20), implying significant penetration of liquid into pores. A calculation of the volume of the voids in the mesh under the droplet at its maximum spread showed that it was approximately 48% of the initial droplet volume (Table 8), so a significant amount of liquid could have been trapped in pores. Increased loss of liquid in the pores would explain why less was left on the surface to spread. To determine if the volume of pores was sufficient to cause a significant loss of liquid volume of the voids in the mesh under the droplet at its maximum spread was calculated.

Table 20
Percentage of liquid penetration for water.

Experiment N	v_i (m/s)	We_p	D_{max} (mm)	D_w(mm)	D_p(mm)	Void volume %
1	1.8	1.1	8.6	0.025	0.025	12
2	2.9	2.8	9.8	0.025	0.025	16
3	3.9	5.2	10.8	0.025	0.025	20
4	1.8	4.6	6.4	0.065	0.1	20
5	2.9	11.2	7.7	0.065	0.1	29
6	3.9	20.8	7.0	0.065	0.1	24
7	1.8	9.1	6.2	0.125	0.2	36
8	2.9	22.5	7.2	0.125	0.2	48
9	3.9	41.5	6.4	0.125	0.2	38

Considering a droplet that has spread to its maximum extent (Fig. 75). The area covered by the spreading droplet is given by

$$A_{sp} = \left(\frac{D_{max}^2}{4}\pi\right) \qquad 4.11$$

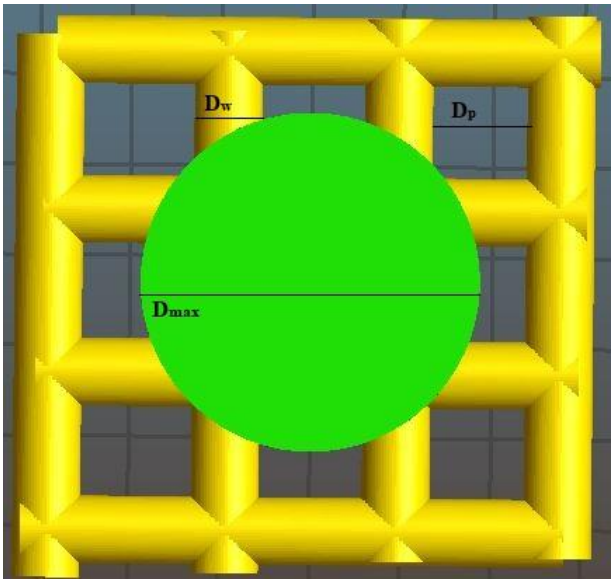

Fig. 75 Impact and spreading of the droplet on the porous surface

To estimate the number of pores (n) under the droplet it was assumed that there is a square of equal area (Fig. 76) with each side covering x pores and x+1wires so that

$$A_{sp} = A_{eq} = \left(D_p \cdot x + (x+1)D_w\right)^2$$

Where D_p and D_w are respectively pore and wire diameter

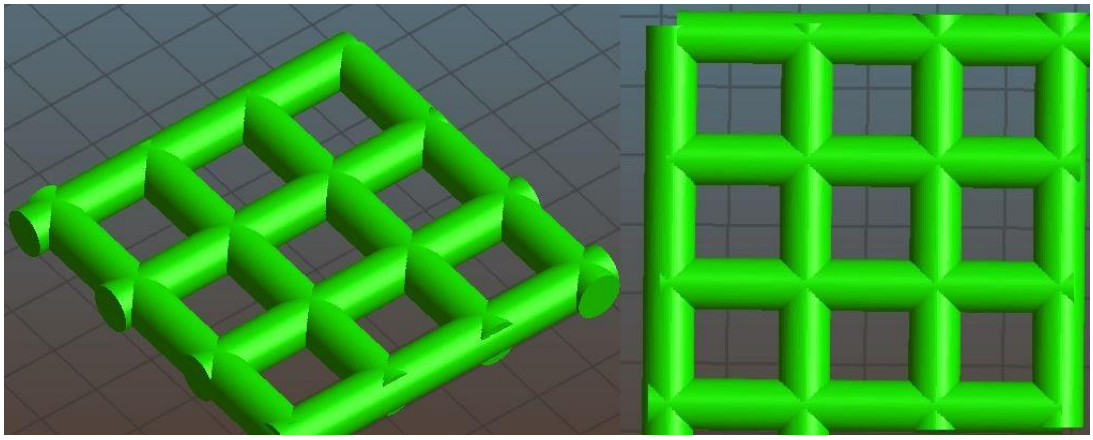

Fig. 76 Equivalent area for the spreading

Consequently, the total number of pores per side will be

$$n = x^2 = \left[\frac{\left(\sqrt{A_{sp}} - D_w\right)}{D_p + D_w}\right]^2$$

The void volume will be given by multiplying the volume of a single pore by the total number of covered pores.
Considering that the mesh consists of overlapped wires which have a cylindrical shape, the volume of the single pore will be given by

$$V_p = 2D_w \cdot \left(D_p + D_w\right)^2 - 2 \cdot \left(D_p + D_w\right) \cdot \frac{\pi \cdot D_w^2}{4}$$

Consequently, the entire void volume is

$$V_{void} = n \cdot V_p \qquad 4.12$$

Table 20 lists the void volume as a percentage of the liquid volume in a drop for different impact conditions and mesh sizes. At the highest impact velocity (3.9 m/s) on a mesh with 0.2 mm pores the void volume is very significant, being 38% of the drop volume. At a lower impact velocities the droplet spread is larger and therefore void volume is even greater, 48%.

4.1.2 Time scales

It was observed that in the case of full penetration, it is not possible to define a spreading of the droplet on the surface because the entire droplet penetrates inside the pores right after the impact. Considering the instant in which the droplet touches the surface, the time required for the first half of the spherical droplet to penetrate inside the surface will be given by

$$t_p = \frac{d}{2v_i} \qquad 4.13$$

Once that the first half of the droplet, completely penetrates inside the surface, no spreading is detectable, and penetration occurs. This leads to a dimensionless time equal to

$$t_p^* = \frac{t_p v_i}{d} = \frac{1}{2} = 0.5 \qquad 4.14$$

This result finds a good agreement with the spreading analysis in Fig. 67 in which the spreading evolution take part for dimensionless time larger than 0.5.
If $t^* < 0.5 = t_p^*$, after the droplet impacts on the surface, no spreading phase or recoiling phase are detectable because all the liquid will penetrate inside the surface.
If $t^* > 0.5 = t_p^*$, the spreading of the droplet will occur and, depending on the pore diameter, impact velocity and liquid properties, there will be a partial imbibition of the liquid inside the surface.

4.1.3 Regime distribution as a function of the initial parameter

To remark the influence that the liquid physical properties have on the final outcome, it is important to have a look at the evolution of the regimes for water, acetone and water & glycerol separately. Having a different time scale does not allow to represent the regimes in a unique graph, for which reason it was chosen to analyse separately the transition between deposition and partial imbibition and the transition between deposition and penetration. Fig. 77 and Fig. 78 show the regimes distribution for water respectively in the case of separation between deposition-penetration and deposition- partial imbibition. We can observe that in the case of water, an almost equal distribution of deposition, partial imbibition and penetration is achievable. Considering Fig. 77, for pores with a diameter larger than 0.2 mm the only dominant outcome is the penetration. This behaviour is due mainly to a larger dimension for the pores.

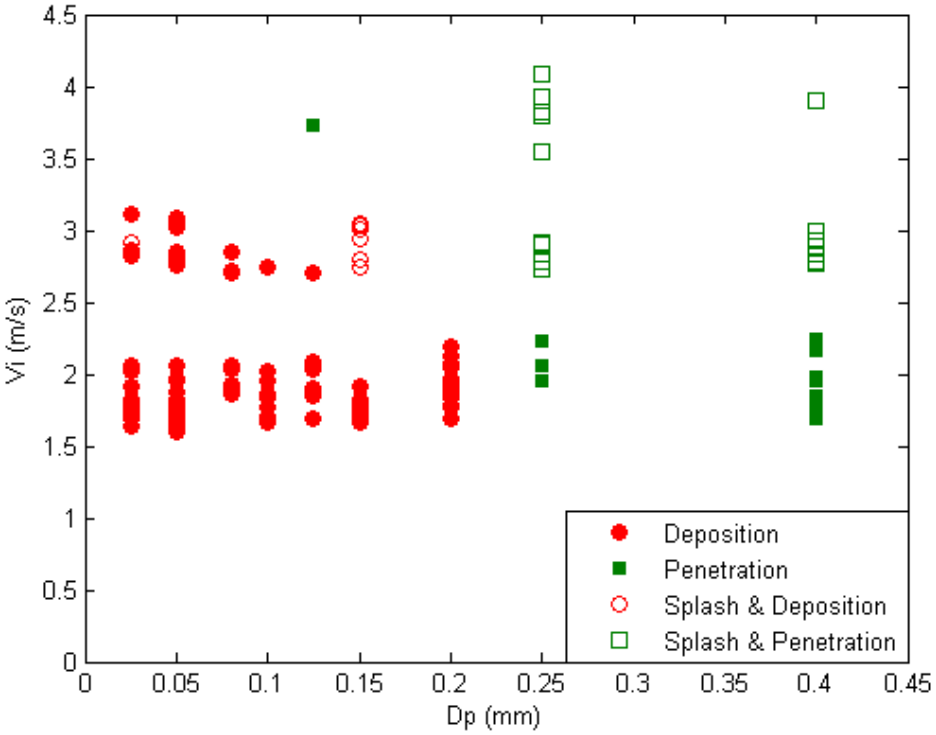

Fig. 77 Regime distribution for water (d ranging between 1.5 and 3mm) as a function of impact velocity and pore diameter, transition between deposition and penetration; $t^* < 0.5$

Considering Fig. 78, the separation between deposition and partial imbibition, we can observe that with increasing impact velocity a transition occurs between deposition and partial imbibition until a value of impact velocity higher than 3.5 m/s for which the partial imbibition is the only dominant outcome.

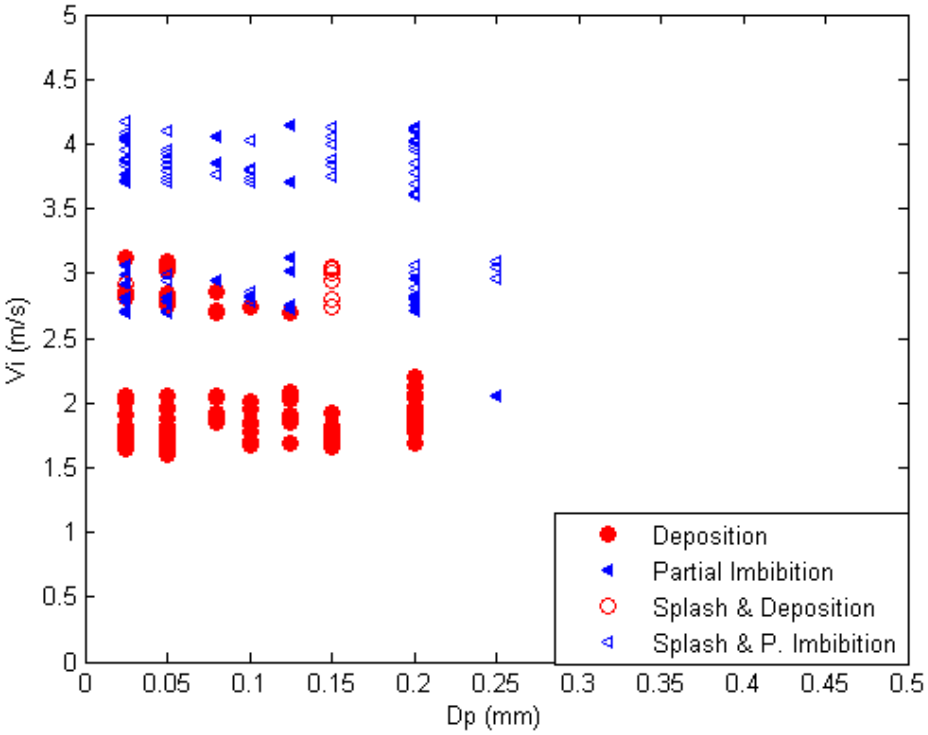

Fig. 78 Regime distribution for water (d ranging between 1.5 and 3mm) as a function of impact velocity and pore diameter, transition between deposition and partial imbibition; $t^* > 0.5$

In the case of water, it is consequently possible to achieve a clear distribution of the regime, considering only a geometrical characteristic of the mesh and the impact velocity.

On the contrary for the acetone, Fig. 79 and Fig. 80, due to the lower viscosity ad surface tension of the liquid, the dominant outcome is given by a penetration and deposition is almost absent.

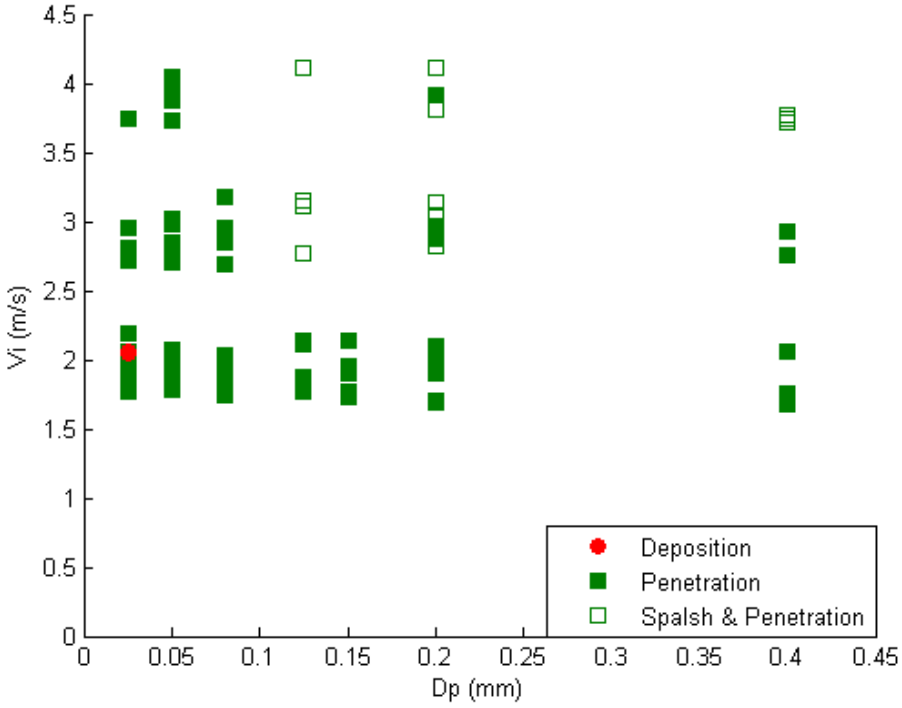

Fig. 79 Regime distribution for acetone (d ranging between 1.5 and 3mm) as a function of impact velocity and pore diameter, transition between deposition and penetration; $t^* < 0.5$

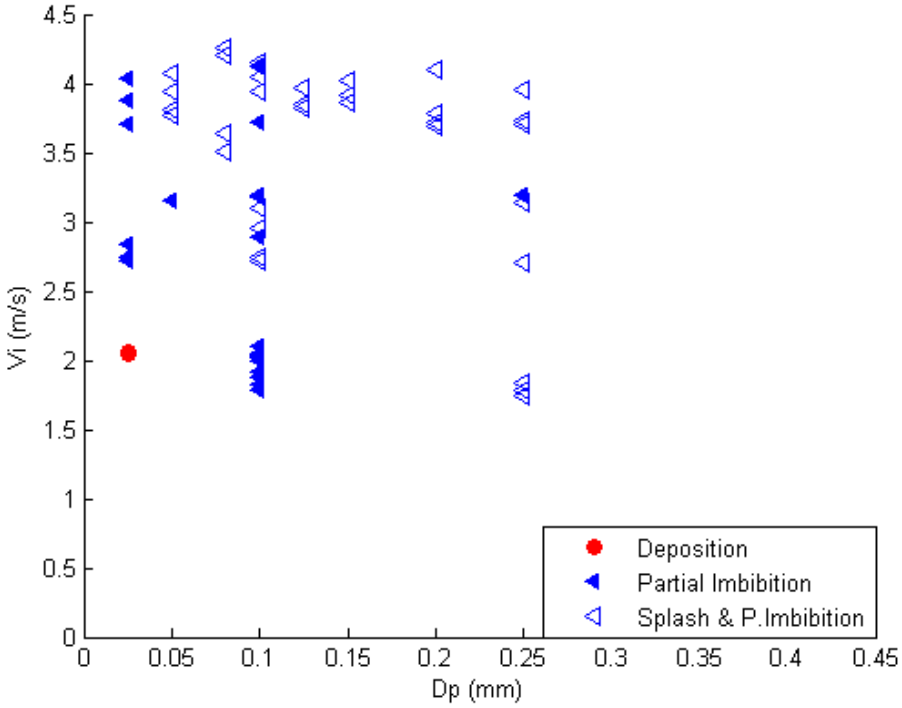

Fig. 80 Regime distribution for acetone (d ranging between 1.5 and 3mm) as a function of impact velocity and pore diameter, transition between deposition and partial imbibition. $t^* > 0.5$

On the opposite, for the solution composed by water and glycerol, Fig. 81, due to the higher viscosity of the liquid, the dominant outcome is given by the deposition and penetration does not occur. The partial imbibition occurs only for higher value of impact velocity.

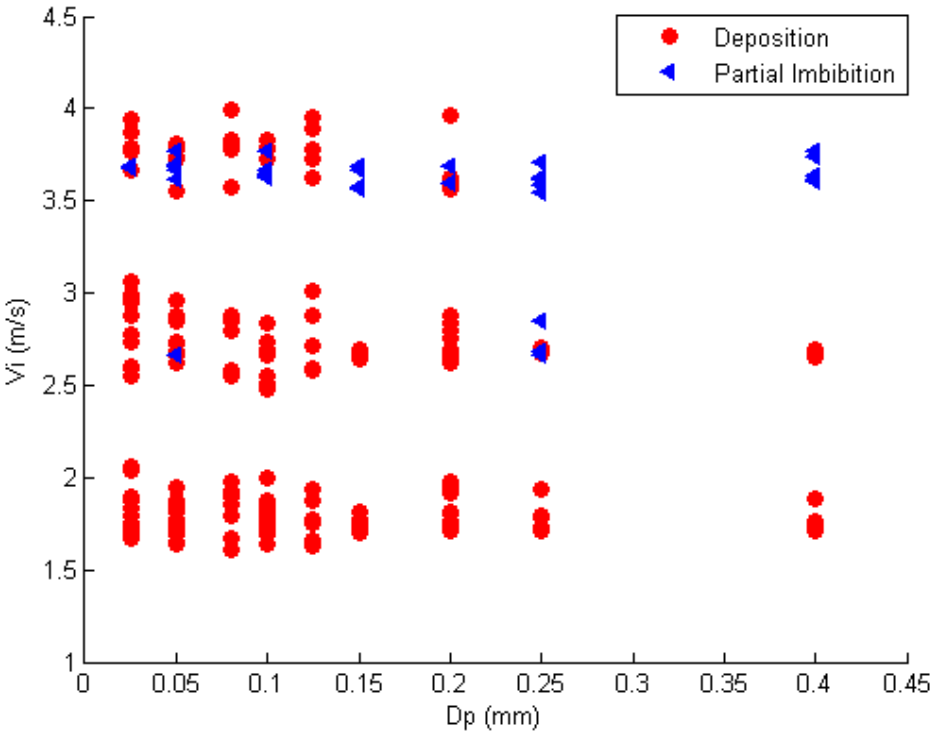

Fig. 81 Regime distribution for water & glycerol (d ranging between 1.5 and 3mm) as a function of impact velocity and pore radius, transition between deposition and partial imbibition. $t^* > 0.5$

According to Sahu et al. [69], who analysed the impact of nanoparticle suspension into porous filter membranes focusing on penetration given by the hydrodynamic effect, the penetration into porous medium is possible when the dynamic pressure is higher than the capillary pressure, but also when hydrodynamic focusing, that occurs when the drop diameter is much larger than pore diameter, is observed.
The dynamic and capillary pressure are given respectively by

$$p_d = \frac{1}{2}\,\rho v_i^2 \qquad 4.15$$

$$p_c = \frac{4\sigma}{D_p} \qquad 4.16$$

where ρ is the density of the droplet, vi the impact velocity, σ the surface tension and D_p the mean pore diameter.

Fig. 82 and Fig. 83, show the regime distribution of the results obtained for three different liquids, considering capillary and dynamic pressure. We can observe that the results are in agreement with the conclusions from Sahu et al [69].

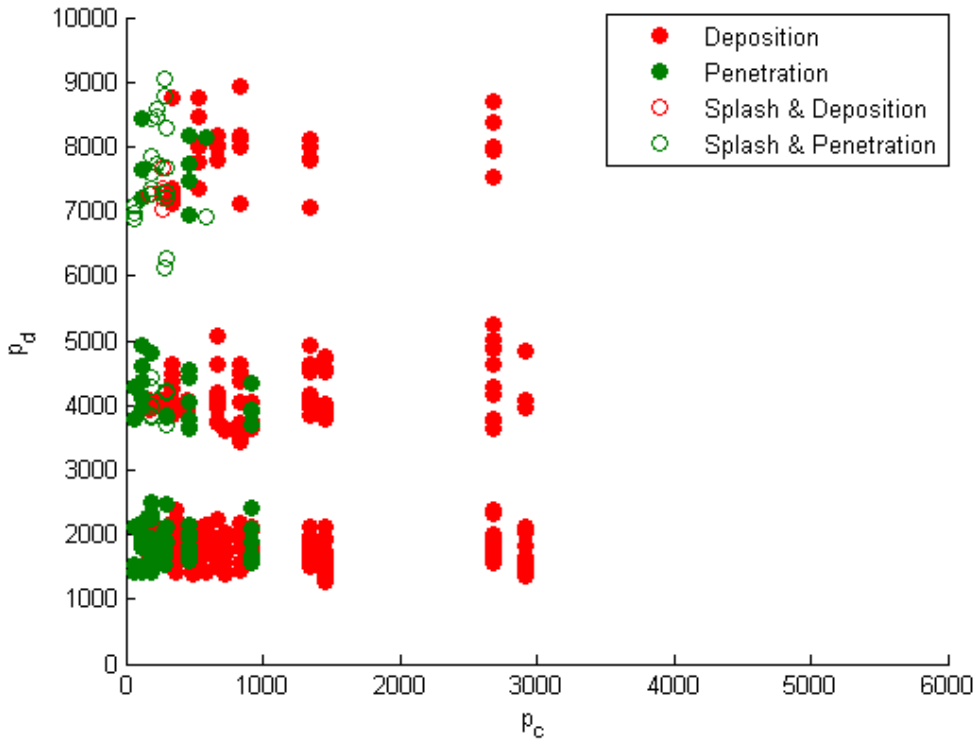

Fig. 82 Deposition- Penetration transition for water, acetone and water & glycerol (d ranging between 1.5 and 3mm) as a function of dynamic and capillary pressure $t^* < 0.5$

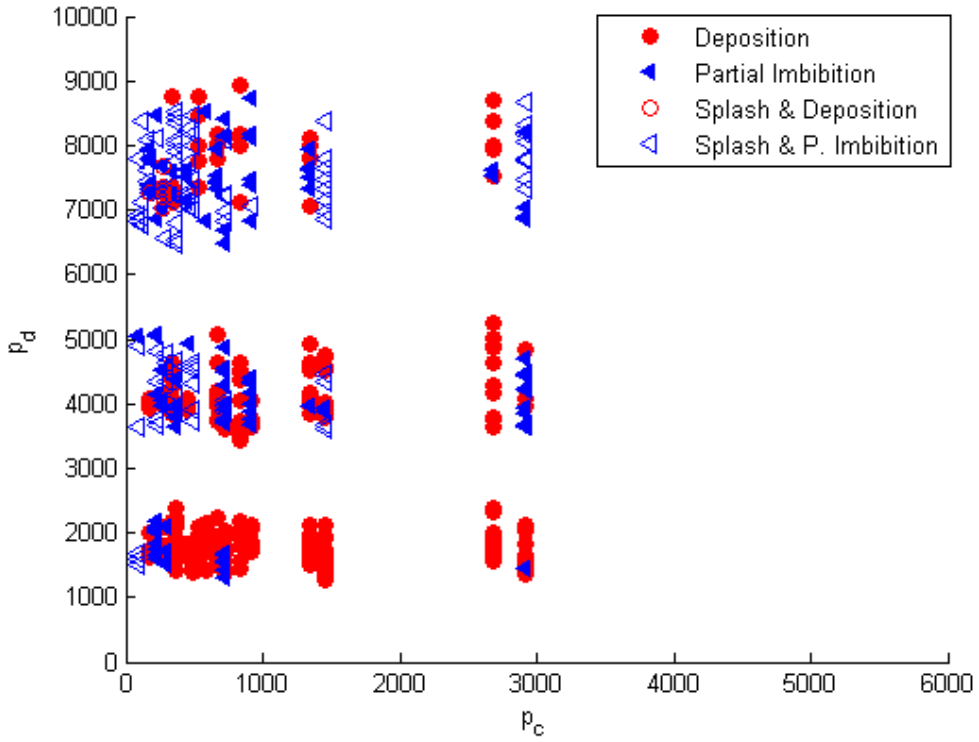

Fig. 83 Deposition- P. Imbibition transition for water, acetone and water & glycerol (d ranging between 1.5 and 3mm) as a function of dynamic and capillary pressure $t^* > 0.5$

The transition between deposition and penetration, Fig. 82 shows that for higher values of capillary pressure the only dominant outcome is the deposition. It is possible to observe a transition interval in which both outcomes are possible, for value of p_c in a range of 500-1000 Pa. Finally, for value of capillary pressure lower than 250 Pa, the only dominant outcome is the penetration.

In Fig. 83, consequently for the separation between deposition and partial imbibition, we can observe a transition between the two regimes increasing the value of the dynamic pressure. For lower values of the capillary pressure and higher values of dynamic pressure, the partial imbibition is the mainly diffused outcome and the effect of dynamic pressure is dominant. As Sahu et al. [69] observed, our results show that penetration will be mainly enhanced by higher value of dynamic pressure respect to the capillary pressure, $p_d \gg p_c$, but it will be influenced also by the hydrodynamic focusing, in fact in our case the size of the droplet diameter is much larger than the pore diameter, d$\gg D_p$.

4.1.4 Regime map

As said, it was observed that penetration and partial imbibition occur at different time-scales.

For this reason, it was chosen to define separately the transition between deposition and partial imbibition and the deposition and penetration in two regimes maps.

4.1.4.1 Dimensionless diameter

To distinguish the different outcome regimes, a first attempt was made, considering a dimensionless diameter given by the ratio between pore size and droplet size, β.

$$\beta = \frac{D_p}{d} \qquad 4.17$$

It was initially considered that there could be a dependence between the outcome and the ratio given by the pore size and the droplet diameter Fig. 84 shows the transition between deposition and penetration. Even if it is possible to observe that there is a correlation between the increasing of the Weber number and the transition from the deposition to the penetration, the distribution of the two regimes is still unclear and it is not possible to separate the two outcomes.

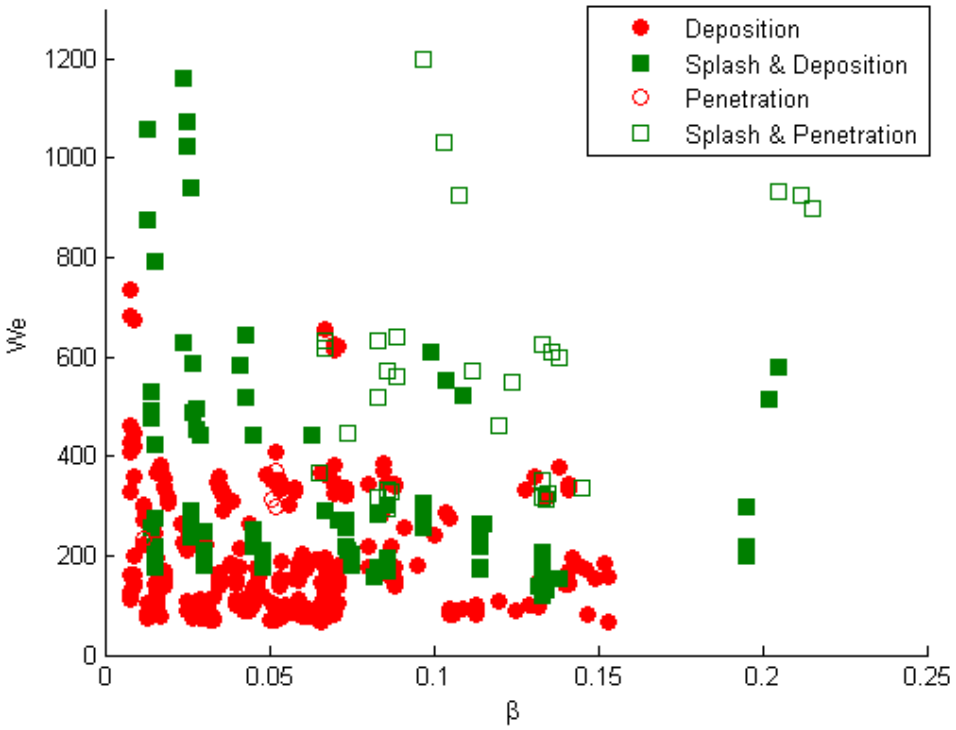

Fig. 84 Regime distribution for water, acetone, water & glycerol (d ranging between 1.5 and 3mm) as a function of β. Transition between deposition and penetration. $t^* < 0.5$

Fig. 85 shows the transition between deposition and partial imbibition. Even in this case for higher Weber number the dominant outcome is given by the partial imbibition, but the distribution for Weber number in a range between 200 and 400 is still unclear.

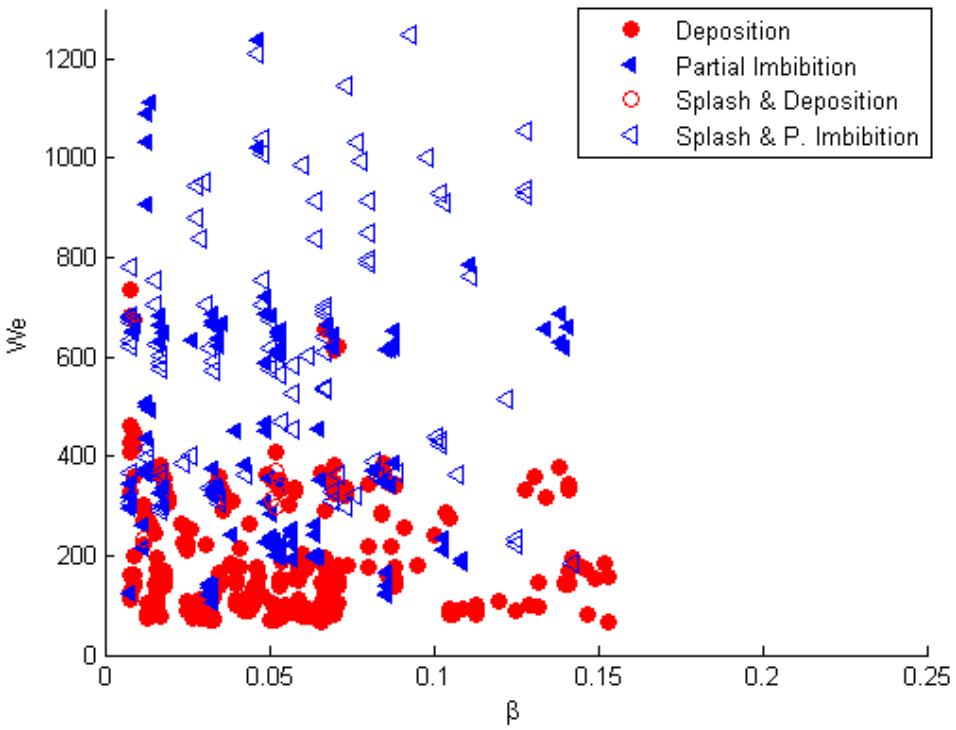

Fig. 85 Regime distribution for water, acetone, water & glycerol (d ranging between 1.5 and 3mm) as a function of β. Transition between deposition and partial imbibition. $t^* > 0.5$

It can be seen that the separation of the outcomes is not clearly defined and, consequently, β is not the best parameter to define the different outcome regions.

4.1.4.2 Mesh geometry

Considering the woven structure of the mesh, it was observed that the wire diameter also plays an important role in determining the evolution of the spreading of the droplet on the surface (conferring a surface roughness) and consequently the percentage of liquid penetration. For this reason, a second attempt was made, introducing a new geometrical parameter given by the ratio of the empty area over the full area of the mesh pore

$$\gamma = \left(1 + \frac{D_w}{D_p}\right)^2 \qquad 4.18$$

where D_w is the mesh wire diameter and D_p the pore diameter. This number was obtained considering that the ratio of the 2 areas can be written as

$$\gamma = \frac{A_{full}}{A_{empty}} = \frac{(D_p+D_w)^2}{D_p^2} = \frac{D_p^2+2D_pD_w+D_w^2}{D_p^2} = \frac{D_p^2\left(1+2\frac{D_w}{D_p}+\frac{D_w^2}{D_p^2}\right)}{D_p^2} = D_p^2 \cdot \frac{\left(1+\frac{D_w}{D_p}\right)^2}{D_p^2} = \left(1+\frac{D_w}{D_p}\right)^2$$

Fig. 86 shows schematically the interaction of the droplet with the mesh geometry.

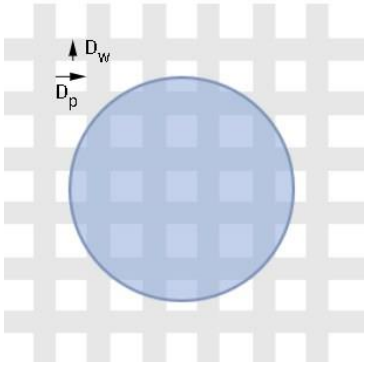

Fig. 86 Impact and spreading of the droplet on the porous surface.

Fig. **87** shows the distribution between deposition and penetration.

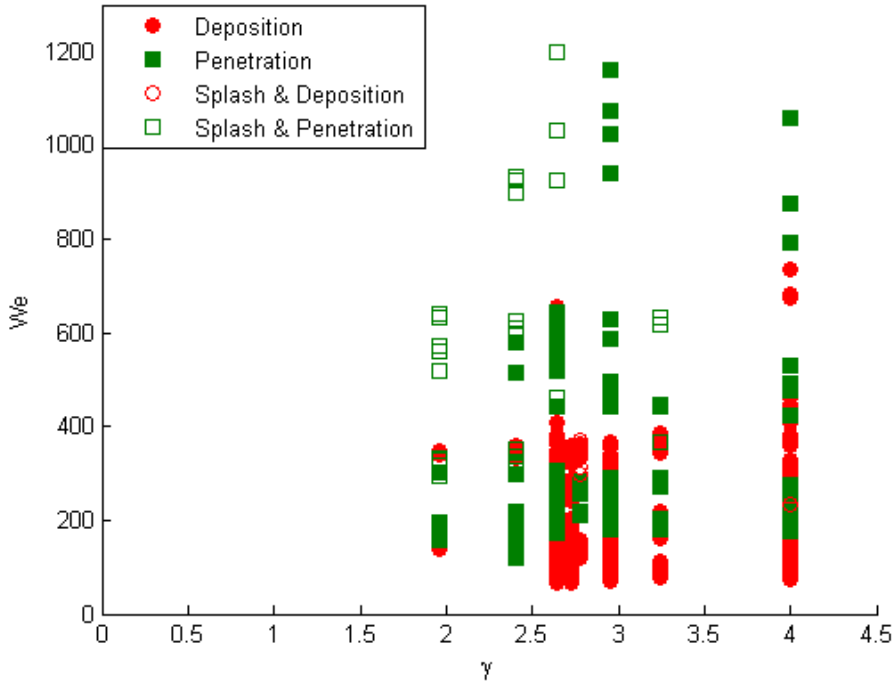

Fig. 87 Regime distribution for all the liquids (d ranging between 1.5 and 3mm) as a function of γ. Transition between deposition and penetration. It is shown that a clear distribution of the regions is still not achievable. $t^* < 0.5$

We can conclude that the use of γ eads to a better separation of the regimes but still, for Weber number in a range between 200 and 400 it is not possible to have a clear separation of the regimes. For lower Weber number values, the only dominant outcome is given by the deposition.

Fig. 88 shows the distribution between deposition and partial imbibition. In this case the distribution is still confused and in particular for lower Weber numbers values it is not possible to obtain a clear separation between the two regimes.

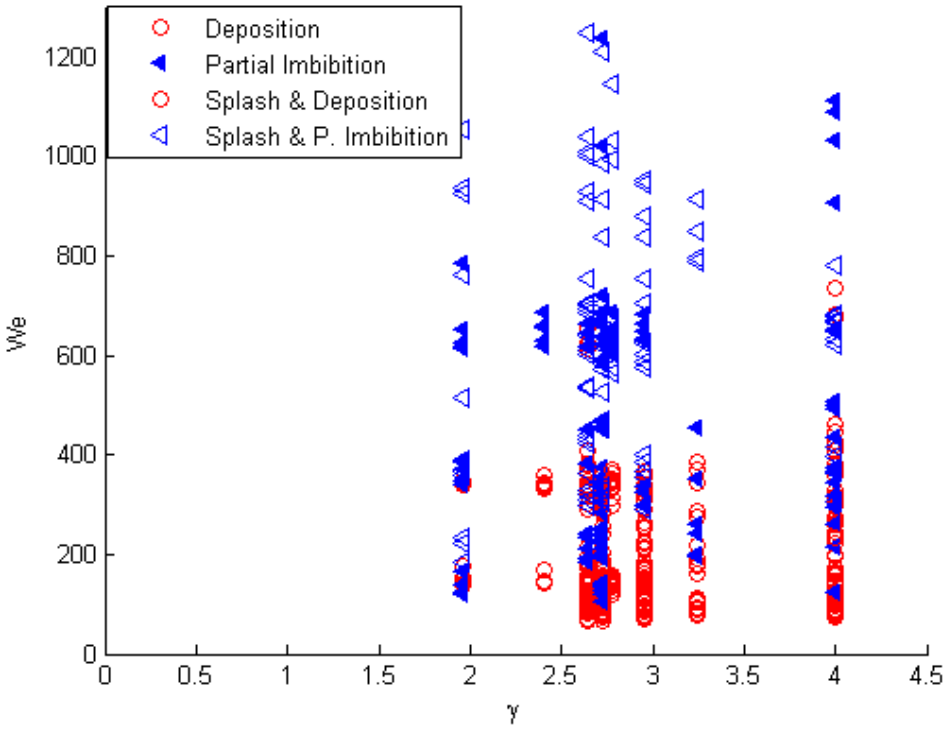

Fig. 88 Regime distribution for all the liquids (d ranging between 1.5 and 3mm) as a function of γ. Transition between deposition and partial imbibition. $t^* > 0.5$

From the graphs above, we can conclude that by using γ, a clearer distribution of the outcomes is achieved in the case of water and a solution of water and glycerol, but the case of acetone is still not clarified. It is still not possible to clearly define the regions of deposition -partial imbibition and deposition-penetration having liquids with different characteristics of physical properties. Therefore, it is necessary to modify the dimensionless numbers used to define the regime map

and find a better combination capable to take in account of all the effects that can influence the impact outcome.

4.1.4.3 Final regime distribution

By looking at the previous results, we can notice that γ leads to an improvement of the separation of the regimes distribution. In fact, the mesh is characterised by two parameters which are pore diameter, D_p and wire diameter, D_w. The previous analysis remarks that both of these geometrical measures influence the outcome of the impact. This is proved for example considering the spreading evolution, in which a higher pore dimension and wire diameter, leads to a higher penetration of the liquid below the mesh.
We can conclude that γ could be the best choice in terms of geometrical parameters to obtain a separation of the regimes.
On the opposite, the Weber number does not allow a good separation. This is because there are multiple liquids properties that influence the nature of the outcome. Considering for example the W&G solution which is characterised by a very high viscosity, the dominant outcome is the deposition and the penetration is almost absent. On the opposite, in the case of acetone, the dominant outcome is given by the penetration which is driven by a lower surface tension which will lead to an easier penetration of the droplet inside the pores. Consequently, we can assume that both viscosity and surface tension must be taken in consideration as well to define the regime distribution. The splash region is mainly influenced by a higher impact velocity and a lower viscosity.
Finally, considering again the fact that penetration and partial imbibition are caused by different physical processes, we can conclude that an attempt to describe the transition between the deposition and partial imbibition and deposition penetration, using the same physical parameter does not lead to a satisfactory result. Therefore, it was chosen to represent the data introducing different dimensionless numbers.

For dimensionless times lower than t_p^*, drop penetration may occur. The regime map in Fig. 89 shows the separation between deposition and penetration.

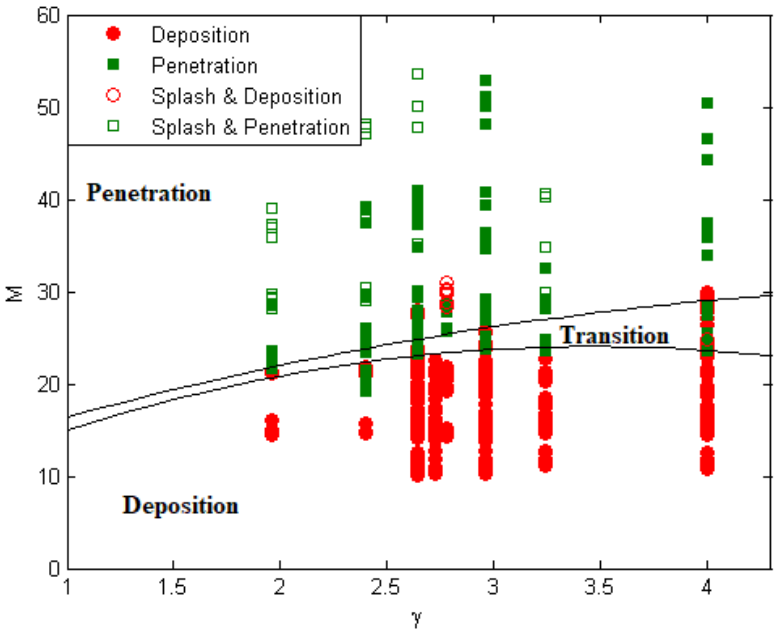

Fig. 89 Regime distribution for all the liquids (d ranging between 1.5 and 3mm) as a function of $\boldsymbol{\gamma}$ and M, transition between deposition and penetration.

The Weber number alone was not sufficient to obtain a satisfactory description of outcome distribution. Therefore, the Weber was coupled with the Reynolds number, to capture the viscosity effects. The best choice of the parameter on y-axis was evaluated by:

$$M = Re^{0.8}We^{2.1} \qquad 4.19$$

The transition with the penetration regime begins at M>20 for γ<2.5 and at M>25 for γ> 2.5 until penetration becomes the only dominant outcome for M>35. The two curves delimiting the deposition-transition-penetration regimes are given by interpolating the points on the lower value of penetration outcome for each value of $\boldsymbol{\gamma}$ and the higher value of deposition outcome for each value of $\boldsymbol{\gamma}$. We can observe that for lower value of γ the penetration is more likely to occurs for lower values of M. This is because at lower value of γ corresponds a larger pore diameter which will influence the penetration threshold.

The best couple of exponentials characterising the number M, were defined using a MATLAB code which maximises the average distance of each point from the points of the other regime and minimises the average distance of each point respect to the points of the same regime.

The code attempts to maximize the average distance between points belonging to different regimes while minimising the average distance between points in the same regime. Four matrices of distance were constructed, listing the distance of each data point in a particular domain from all the other points belonging to the same domain, and from all points of the other domain. From the matrices it was possible to determine average distance vectors. If a given data point was on average closer to points belonging to the other domain than those of the same domain, it was classified as an error, and the best exponential values were those that led to the smallest number of errors. Finally, the code analysed the distance between the orthocentres of the two domains to select exponentials that maximised the distance between the orthocentres and consequently led to better separation between the domains.

For $t^* > 0.5$, we can observe the spreading of the droplet on the surface and consequently the complete penetration does not occur. Viscosity plays a major role to describe the deposition/partial-imbibition transition for which reason the parameter on the y axis is exclusively given by the Reynolds number in Fig. 90. In fact, in contrast with the findings of Lorenceau et al. [73], in our case the geometry of the mesh is the dominant factor compared to the Weber number when defining the different regimes area. Increasing the viscosity and for lower Reynolds number, the dominant outcome is deposition. The transition between deposition and partial imbibition will be mainly influenced by a higher velocity or a lower viscosity (higher Reynolds number) and $\boldsymbol{\gamma}$ will have a less relevant role. Higher values of Re (Re>10000) lead to a splash outcome.

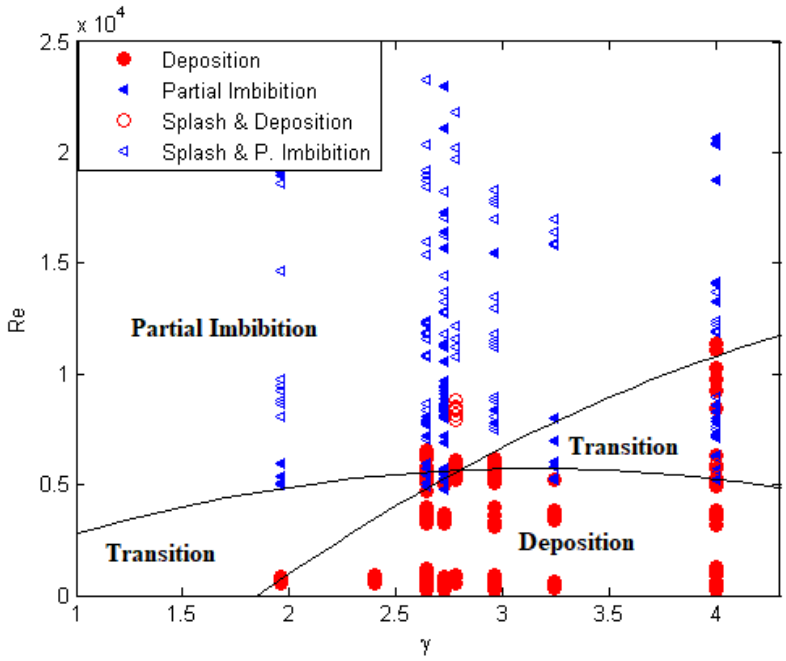

Fig. 90 Regime distribution for all the liquids (d ranging between 1.5 and 3mm) as a function of γ and Re with the transition between deposition and imbibition

The two curves delimiting the deposition-transition-penetration regimes are given by interpolating the points on the lower values of partial imbibition outcome for each value of $\boldsymbol{\gamma}$ and the higher values of deposition outcome for each value of $\boldsymbol{\gamma}$.

4.1.5 Attached mesh results

Our results show that, in contradiction to the findings of Roisman et al. [35], the two most important parameters to describe the impact of droplets on a porous material may not be the Weber number and a ratio given by considering the geometrical roughness. The present results show a good agreement with those of Sahu et al. [69]. In fact, our results show that penetration will be mainly enhanced by larger value of dynamic pressure respect to the capillary pressure, $p_d \gg p_c$, but it will be influenced also by the hydrodynamic focusing where the dimension of the droplet diameter is much larger than the pore diameter, $d \gg D_p$.

In analysing the spreading evolution of the droplets after the impact, it was found that the roughness factor r introduced by Sivakumar et al. [101] also well described the spreading on the porous metallic mesh, considering the wire diameter as a measure of roughness. However in contrast with the results shown by Sivakumar et al. [101] for a rough surface, in the case of porous membranes, increasing the value of r, it was observed that at higher Weber number values, the maximum spreading diameter will not increase. This is due to the fact that the percentage of liquid penetration below the surface will be enhanced by the inertial forces.

Our results are no completely in agreement with the research of Lorenceau et al. [73], describing the threshold between the capture of the droplet above the surface, and its partial ejection below the surface. The study of Lorenceau et al. [73], is focused on the penetration of a droplet on a plate with a single hole which will have a different influence on the phenomena respect to a mesh with multiple pores. The research of Ryu et al. [78] partially agrees with our results since it describes the threshold between deposition and partial imbibition in the case of water. However, considering a wider range of liquids properties and outcome which also include the complete penetration of the droplet into the pores and a splash, to obtain a more defined transition between the regimes at different time scale, two different regimes map were proposed. The initial phase, t<0.5, defines the separation between deposition and the complete penetration of the droplet inside the surface. For t>0.5, a second regime map is proposed, defining the transition between deposition and partial imbibition. In both cases it was observed that a higher impact velocity leads also to a splash outcome and that it is necessary to define a geometrical parameter

which considers both the mesh pore size and mesh wire diameter to have a clearer regime distribution. The results are summarised in Table 21.

Table 21
Attached meshes, results summary.

Work	Research topic	Main findings	Comparison with our work
Roisman et al. [35]	Analysis of different regimes of splash threshold focusing on substrate roughness and randomly porous surfaces.	The impact of droplets on a porous material can be described by Weber number and a ratio given by considering the geometrical roughness. In the case of porous substrates, drops deposition without splash is more probable because of the penetration of the drops inside the substrate.	Given the dimensionless numbers M and γ, our results show that, in contradiction to the findings of Roisman et al. [35], the two most important parameters to describe the impact of droplets on a porous material may not be just the Weber number and a ratio given by considering the geometrical roughness.
Sahu et al. [69]	Impact of nanoparticle suspension into porous filter membranes focusing on penetration given by the hydrodynamic effect.	The penetration of the droplet into the pore is enhanced if the dynamic pressure is higher than the capillary pressure, but also when hydrodynamic focusing is observed.	In Agreement with Sahu et al. [69]our results show that penetration will be mainly enhanced by larger value of dynamic pressure respect to the capillary pressure, $p_d \gg p_c$, but it will be influenced also by the hydrodynamic focusing where the dimension of the droplet diameter is much larger than the pore diameter, $d \gg D_p$.
Sivakumar et al. [101]	Water droplet impact and spreading on stainless steel structured surfaces.	An increase of the value of d (height of square pillar), and consequently of the roughness factor r, leads to a smaller spreading diameter.	The work of Sivakumar et al. [101], well described also the spreading on the metallic porous mesh, considering the wire diameter as a measure of roughness. However in contrast with the results shown by Sivakumar et al. [101] for a rough surface, in the case of porous membranes, increasing the value of r, it was observed that at higher Weber number, the maximum spreading diameter will not necessarily increase.

Lorenceau et al. [73]	Impact of droplet against thin plates pierced with small holes.	Definition of a velocity threshold curve for which penetration of the liquids occurs.	Our results find a good agreement with the research of Lorenceau et al. [73]describing the threshold between the capture of the droplet above the surface, and its partial ejection below the surface However, considering a wider range of outcome which also include the complete penetration of the droplet into the pores and a splash, to obtain a more defined transition between the regimes at different time scale, two different regimes map were proposed.
Ryu et al. [78]	Water droplet impact on meshes with submillimetre pores, focusing on different surface wettability.	Definition of a velocity threshold for which penetration of the liquids occurs. (balance between capillary pressure and dynamic pressure)	Our results find a good agreement with the research of Ryu et al. [78] describing the threshold between deposition and partial imbibition in the case of water. However, considering a wider range of liquids properties , to obtain a more defined transition between the regimes at different time scale, two different regimes map were proposed.

4.2 Suspended meshes

4.2.1 Regime Definition

The second configuration of the suspended meshes, leads to similar outcomes compared to the ones of the attached meshes. The outcomes are shown in Fig. 91. In the sequence in Fig. 91 (a) it is possible to observe the impact of a droplet of a solution of glycerol and water, on a surface with pore size of 25 μm at an impact velocity of 1.8 m/s. Due to the high viscosity of the liquid, the small dimension of the pores and the low impact velocity, no penetration of the liquid occurs and the outcome is defined by the deposition. On the opposite in Fig. 91 (b-c), the sequences show a partial imbibition outcome. In both cases the impact is given by a droplet of water on a surface with porosity of 50 μm. Whereas in figure Fig. 91 (b), due to the lower velocity of 1.8 m/s, the liquid which penetrates below the surface separates from an initial liquid jet bringing to the formation of 2 droplets, in Fig. 91 (c), due to the higher velocity of 3.6 m/s, no liquid jet is observed and the liquid which penetrates below the surface forms a spray-cone composed by a high number of very small size droplets. A similar situation is observable in Fig. 91 (d-e). The sequences show the impact of a droplet of water on a surface of 400 μm porosity. In Fig. 91 (d) due to the lower velocity of 1.8 m/s, the outcome is given by a partial imbibition, in fact part of the liquid remains above the surface after the impact whereas in Fig. 91 (e) the outcome is given by a penetration, due to the higher velocity of 3.6 m/s.

The penetration of the liquid after the impact is influenced by the impact velocity, as it is shown in Fig. 91 b-c or Fig. 91 d-e, in which, for the same pore size, a higher velocity leads to a different effect in terms of liquid penetration. In both cases, increasing the pore size or the impact velocity will result in a major number of daughter droplets generated below the surface. Pore size plays an important role as well, in fact comparing Fig. 91 (b) with Fig. 91 (d), it is possible to observe that, given the same impact velocity but increasing the pore size, a different effect is achieved and the percentage of liquid penetration will increase with the pore diameter.

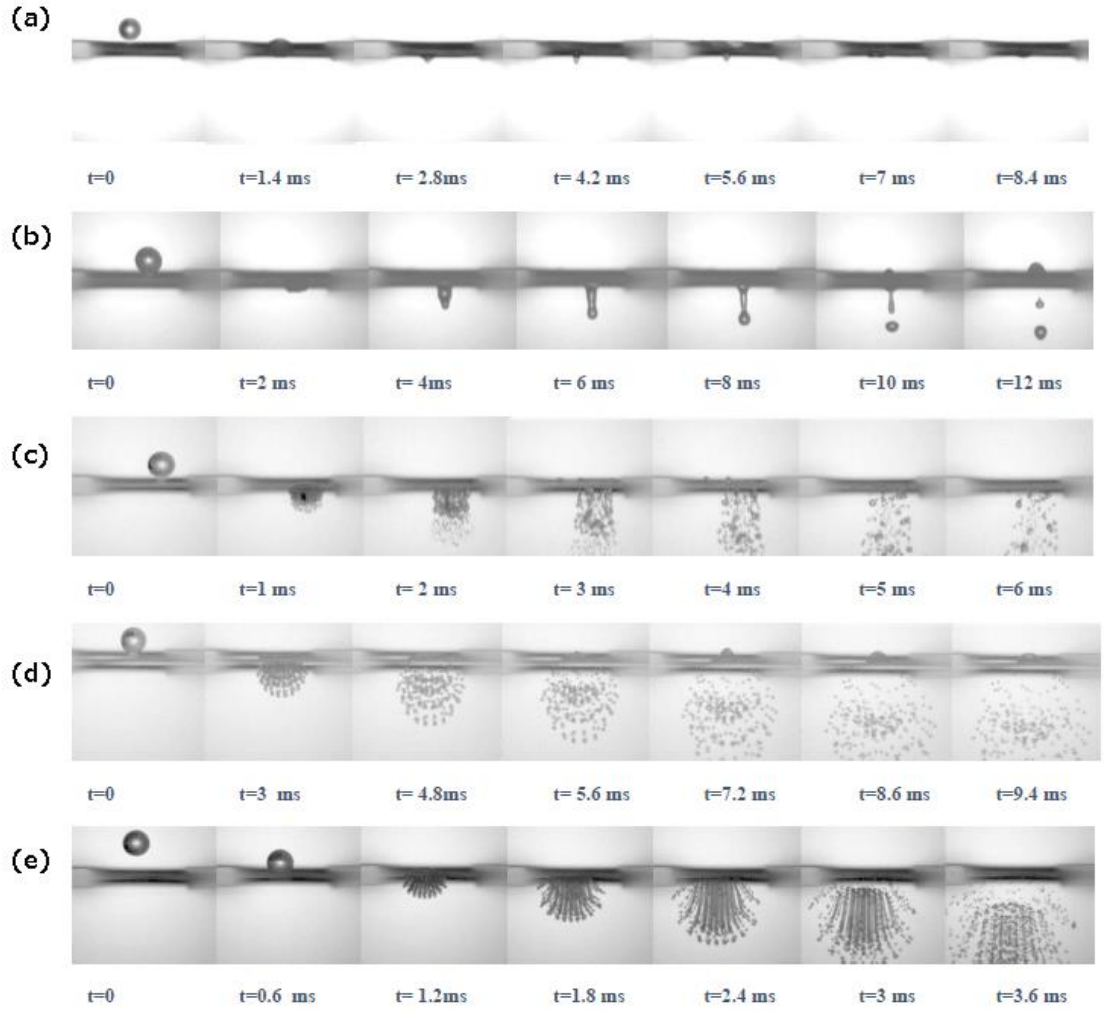

Fig. 91 (a) Deposition Outcome; Water & Glycerol, v_i= 1.8 m/s, d= 2.8 mm, D_p= 25µm, D_w= 25µm **(b)** Partial Imbibition Outcome. Water, v_i= 1.8 m/s, , d= 2.8 mm, D_p= 50µm, D_w= 60µm **(c)** Partial Imbibition Outcome; Water, v_i= 3.6 m/s, d= 3.0 mm, D_p= 50µm, D_w= 60µm **(d)** Partial Imbibition Outcome; Water, v_i= 1.8 m/s , d= 2.9 mm, D_p= 400µm, D_w= 220 µm **(e)** Penetration Outcome; Water, v_i=3.6 m/s, , d= 2.9 mm, D_p= 400µm, D_w= 220 µm

4.2.2 Percentage of liquid penetration

An estimation of the liquid penetration is given, computing the volume of the single droplets ejected from the surface after the impact (case of Fig. 91 b) or subtracting the volume of the remaining cap above the mesh from the initial volume (case of Fig. 91 a-c-d). The initial volume of the droplet is calculated from the droplet radius, assuming that the droplet has a perfectly spherical shape.

The general trend of liquid penetration for the three liquids with the associated error bar, as a function of pore size, liquid properties and impact velocity it is shown in Fig. 92, Fig. 93 & Fig. 94. For all the liquids it is shown that increasing the pore size will increase the percentage of liquid penetration. At the same time, given the same pore size but increasing the impact velocity, the percentage of liquid penetration will be higher.

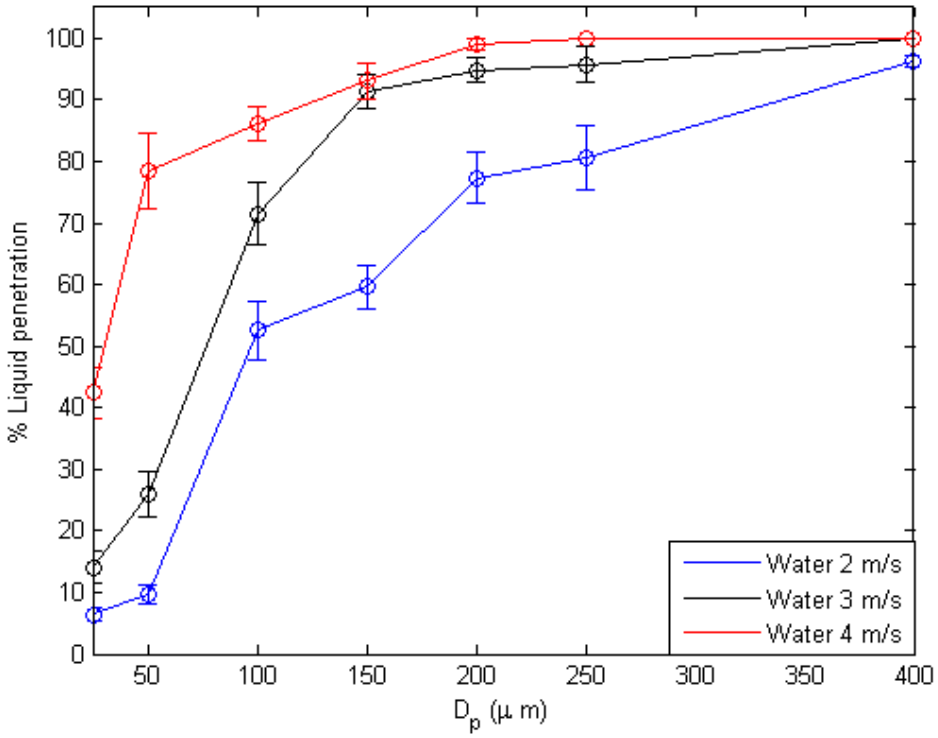

Fig. 92 Percentage of liquid penetration of water as a function of pore size given different range of impact velocity

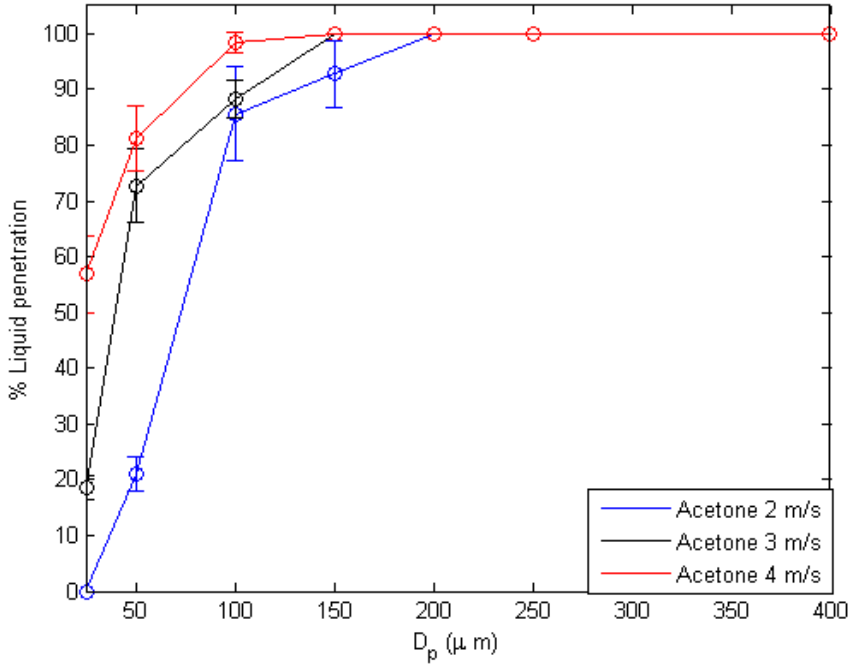

Fig. 93 Percentage of liquid penetration of acetone as a function of pore size given different range of impact velocity

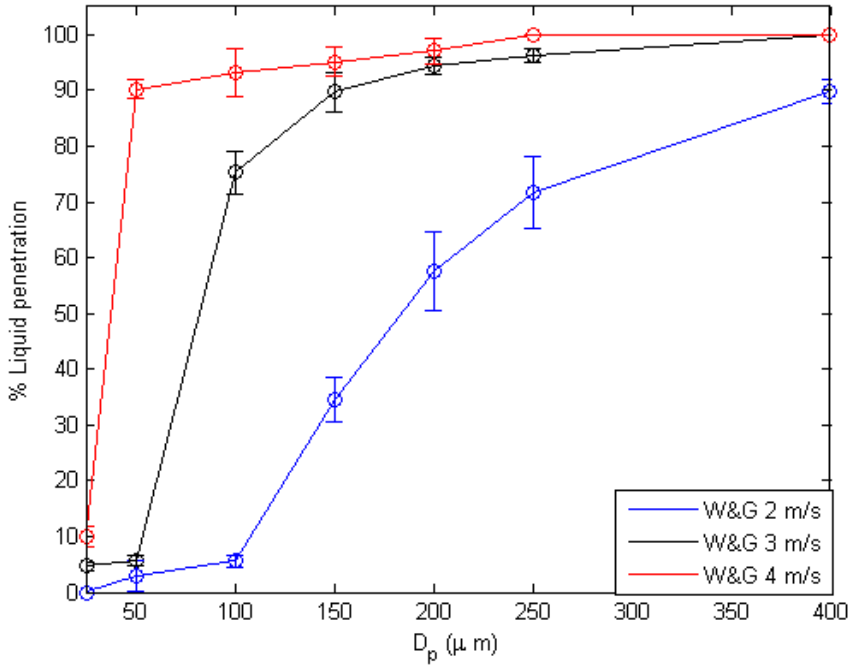

Fig. 94 Percentage of liquid penetration of W&G as a function of pore size given different range of impact velocity

Table 22, Table 23 and Table 24 show the average percentage of liquid penetration and standard deviation respectively for water, acetone and water and glycerol at different impact velocities. Each measurement is taken for 5 different cases.

Table 22 Percentage liquid penetration water

Pore size	$v_i = 2m/s$		$v_i = 3m/s$ (%)		$v_i = 4m/s$ (%)	
(μm)	%	σ	%	σ	%	σ
25.0	6.4	1.1	14.1	2.7	42.4	4.2
50.0	9.7	1.4	26.0	3.7	78.4	6.2
100.0	52.5	4.7	71.4	5.1	86.1	2.7
150.0	59.6	3.5	91.4	2.8	93.0	2.9
200.0	77.4	4.2	94.9	1.9	99.0	1.0
250.0	80.5	5.3	95.8	3.0	100.0	0.0
400.0	96.2	0.8	100.0	0.0	100.0	0.0

Table 23 Percentage liquid penetration acetone

Pore size	$v_i = 2m/s$		$v_i = 3m/s$ (%)		$v_i = 4m/s$ (%)	
(μm)	%	σ	%	σ	%	σ
25.0	0.0	0.0	18.6	2.1	56.9	6.9
50.0	21.0	3.0	72.8	6.5	81.2	5.9
100.0	85.6	8.4	88.1	3.4	98.4	1.8
150.0	92.8	6.0	100.0	0.0	100.0	0.0
200.0	100.0	0.0	100.0	0.0	100.0	0.0
250.0	100.0	0.0	100.0	0.0	100.0	0.0
400.0	100.0	0.0	100.0	0.0	100.0	0.0

Table 24 Percentage liquid penetration W&G

Pore size	$v_i = 2m/s$		$v_i = 3m/s$ (%)		$v_i = 4m/s$ (%)	
(μm)	%	σ	%	σ	%	σ
25.0	0.0	0.0	4.7	0.7	4.7	1.9
50.0	2.9	2.8	5.7	1.0	5.7	1.7
100.0	5.6	1.1	75.3	12.1	75.3	4.3
150.0	34.6	4.0	89.7	3.5	89.7	2.6
200.0	57.6	7.1	94.4	1.6	94.4	2.3
250.0	71.8	6.4	96.3	1.2	96.3	0.0
400.0	89.9	2.1	100.0	0.0	100.0	0.0

To verify if the vertical movement of the mesh due to the impact can have an influence on the percentage of penetration or the outcome, some of the experiments were repeated using a 21-gauge needle with water, acetone and W&G on surfaces with pore sizes of 25, 200 and 400 μm. To suspend a portion of the mesh two different ring size were used, respectively with a diameter dimension of 15 mm and 25 mm to verify if the amplitude of the oscillation can influence the outcome.

No significant difference was observed in terms of outcome and percentage penetration for any of the considered liquid (Table 25, Table 26 & Table 27). It is possible to conclude that the movement of the mesh has no relevant effect on the nature of the outcome.

Table 25 Percentage of liquid penetration Water for different ring size

Pore size (μm)	Impact velocity (m/s)	% Liquid penetration ring size (1.5cm)	% Liquid penetration ring size (2 cm)	% Liquid penetration ring size (2.5cm)
25	2	7	10	7
25	3	13	11	14
25	4	46	42	43
200	2	79	76	77
200	3	90	88	95
200	4	100	98	99
400	2	96	94	96
400	3	100	100	100
400	4	100	100	100

Table 26 Percentage of liquid penetration Acetone different ring size

Pore size (μm)	Impact velocity (m/s)	% Liquid penetration ring size (1.5cm)	% Liquid penetration ring size (2 cm)	% Liquid penetration ring size (2.5cm)
25	2	0	0	0
25	3	21.13	18.6	19.4
25	4	51.2	56.9	54.3
200	2	100	100	100
200	3	100	100	100
200	4	100	100	100
400	2	100	100	100
400	3	100	100	100
400	4	100	100	100

Table 27 Percentage of liquid penetration W&G for different ring size

Pore size (μm)	Impact velocity (m/s)	% Liquid penetration ring size (1.5cm)	% Liquid penetration ring size (2 cm)	% Liquid penetration ring size (2.5cm)
25	2	0	0	0
25	3	0	4.7	0
25	4	0	10	0
200	2	58.41	57.6	59.95
200	3	91.2	94.4	87.27
200	4	95.4	97.1	97.6
400	2	86.4	89.9	83.27
400	3	100	100	100
400	4	100	100	100

Fig. 95, Fig. 96 & Fig. 97 show the trend of liquid penetration for the three liquids at the same impact velocity.

In Fig. 95 which corresponds to an impact velocity of 2 m/s, it is shown that given the same pore size and velocity, increasing the viscosity, the liquid penetration will

be lower. At the same time, for a lower surface tension, as for the case of acetone, given the same pore size and velocity, the percentage of penetration will be higher.

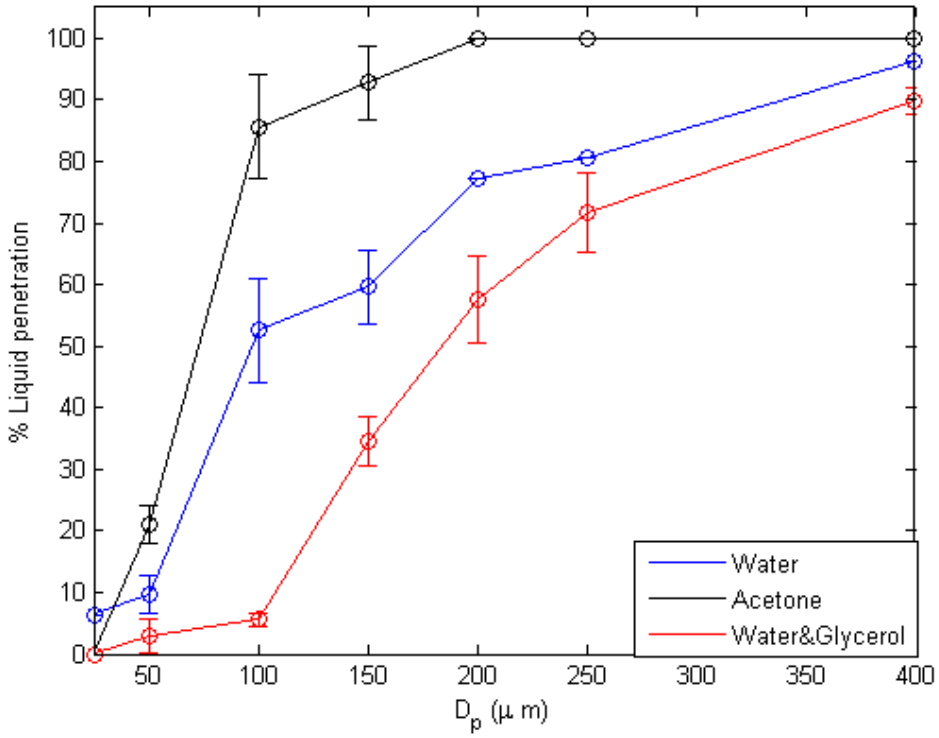

Fig. 95 Percentage of liquid penetration of water, acetone, water & glycerol at 2 m/s as a function of pore size.

The effect of liquid properties becomes less critical with increasing impact velocity. In fact, observing Fig. 96 and Fig. 97 which corresponds respectively to a impact velocity of 3 m/s and 4 m/s, the difference in percentage of liquid penetration of water, acetone and W&G is lower.

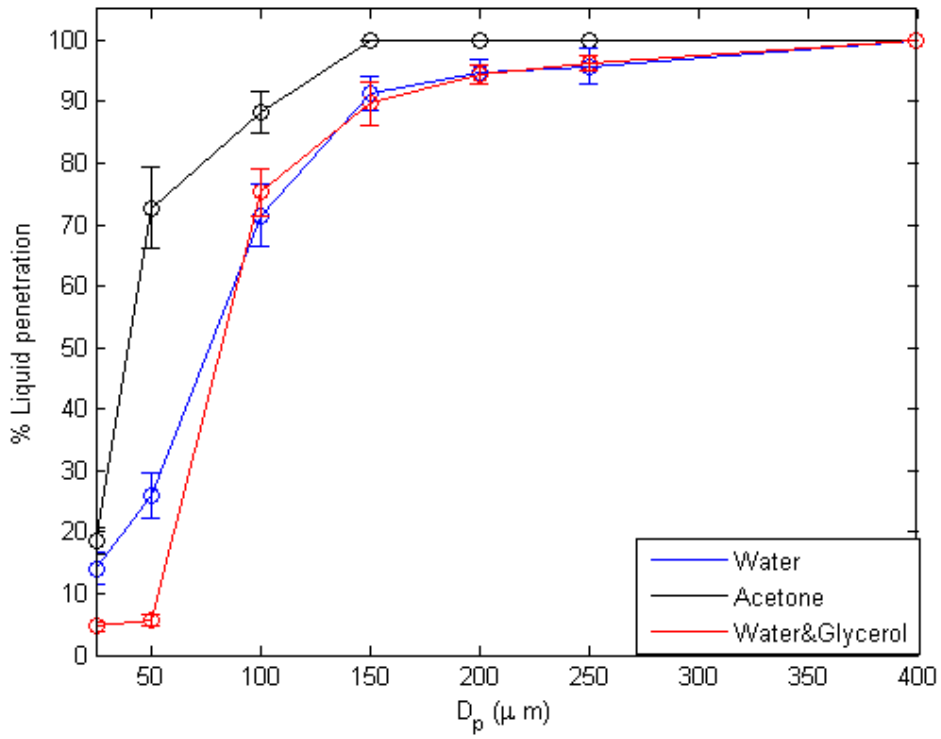

Fig. 96 Percentage of liquid penetration of water, acetone, water & glycerol at 3 m/s as a function of pore size.

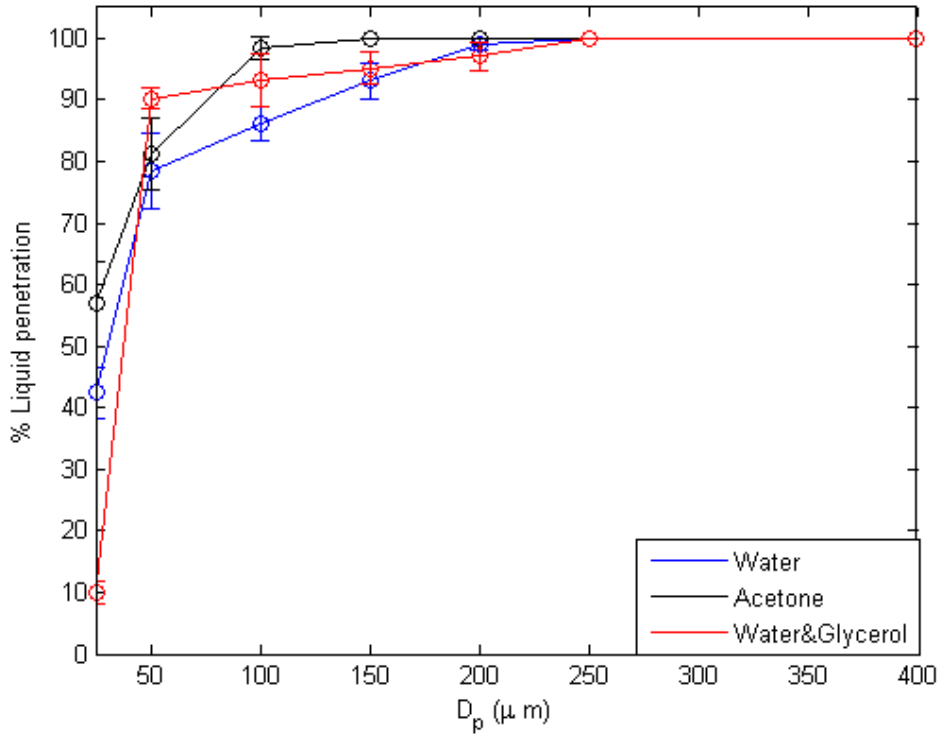

Fig. 97 Percentage of liquid penetration of water, acetone, water & glycerol at 4 m/s as a function of pore size.

Fig. 98 shows the trend of liquid penetration for a droplet of water, at the same impact velocity but with a different initial diameter. According to the study of Xu et al.[77], who analysed water droplet impact on meshes with different pores sizes, it is possible to define a number N given by the ratio of the shadow area of the droplet over the single pore area.

$$N = \frac{A_s}{A_u} = \frac{\pi D^2}{4} \cdot \frac{1}{(D_p + D_w)^2} \qquad 4.20$$

Increasing the value of N, the value of the impact velocity, necessary to eject part of the droplet below the surface, will be lower. In our experiments, it is shown that, given the same impact velocity, the percentage of liquid penetration of a droplet with a mean diameter equal to 3 mm will be higher than the one for a droplet of 2.1 mm, which means that for a smaller droplet of water, the impact velocity necessary to get the same liquid through the pore must be higher. However, increasing the size of the pore, in the specific for a pore diameter larger than 100 µm, the percentage of liquid penetration at lower velocity will be higher in the case of droplets of water with a smaller diameter (Fig. 98).

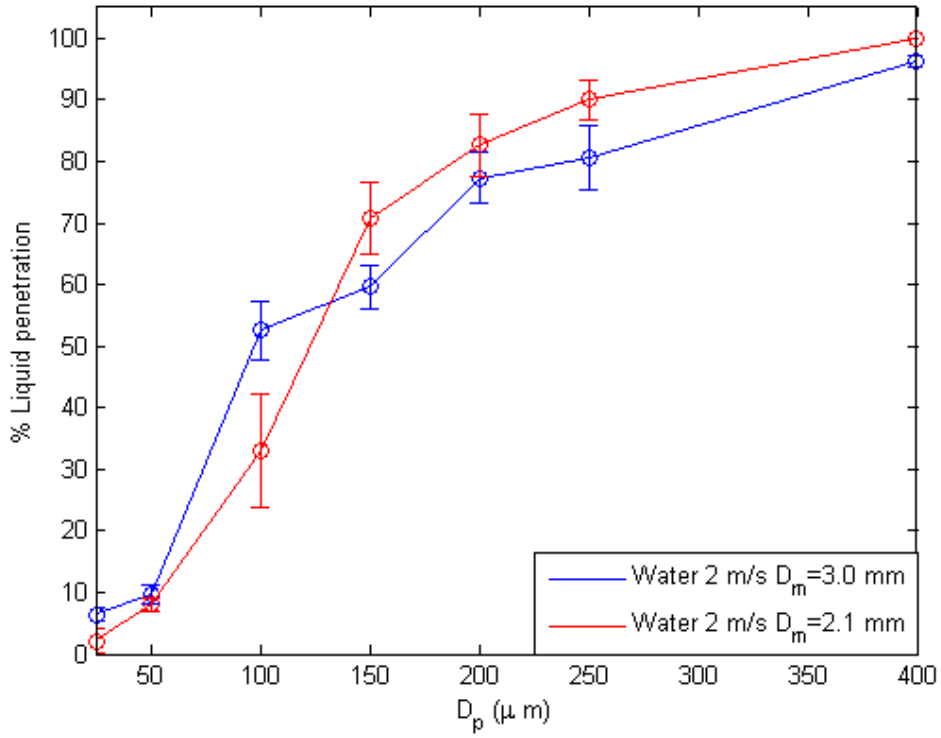

Fig. 98 $v_i = \frac{2m}{s}$ Percentage of liquid penetration of droplet of water with a different initial diameter.

Increasing the impact velocity, the difference in percentage of liquid penetration for droplet with larger or smaller diameter, will be lower (Fig. 99).

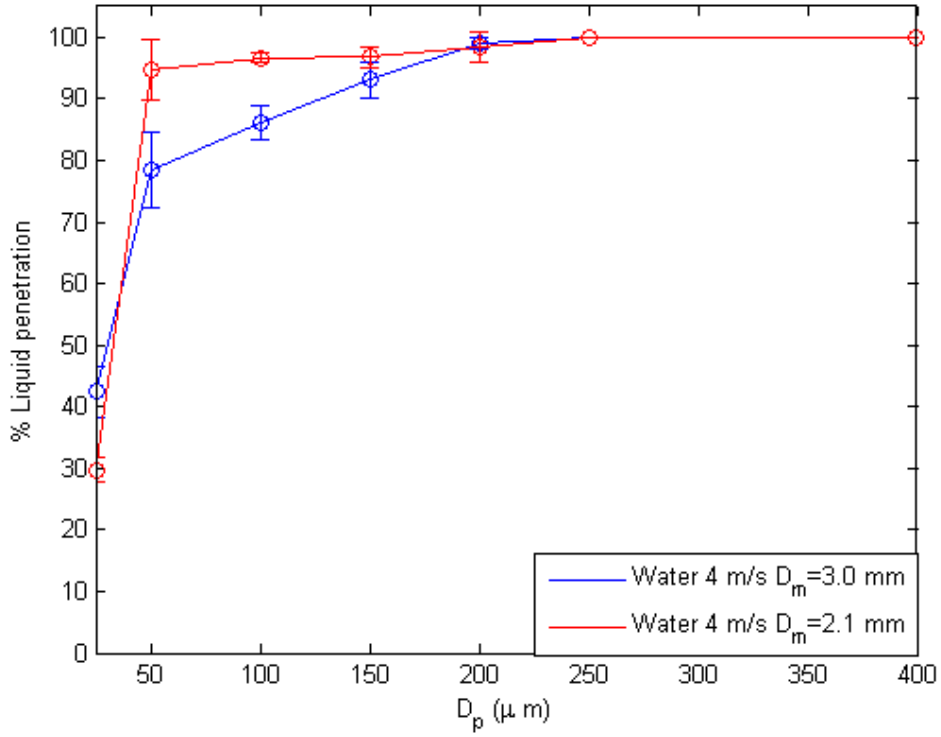

Fig. 99 $v_i = \frac{4m}{s}$ Percentage of liquid penetration of droplet of water with a different initial diameter.

Xu et al. [77] pointed out that, for a wide range of pore dimension, it is not appropriate to refer to a constant coefficient to predict the impact velocity for which penetration will occur. The assumption it is possible just considering a single mesh geometry and without varying liquid properties. In fact, our research shows that varying liquid properties, for example in the case of water and W&G, given the same droplet initial diameter and mesh geometry, penetration will occur at a different impact velocity. Consequently, the coefficient N is not accurate enough to estimate the velocity for which penetration will occur.

Comparing again our results in the case of suspended meshes to the study of Lorenceau et al. [73], it is possible to observe that, the threshold velocity for which

the droplet is partially ejected through the pores, captures the deposition regime in a better way with respect to the case of the attached mesh. In our case, working in a velocity range between 2-4 m/s, which is higher than the range in which Lorenceau et al. [73] operated, the deposition will be mainly influenced by the high viscosity of the liquid.

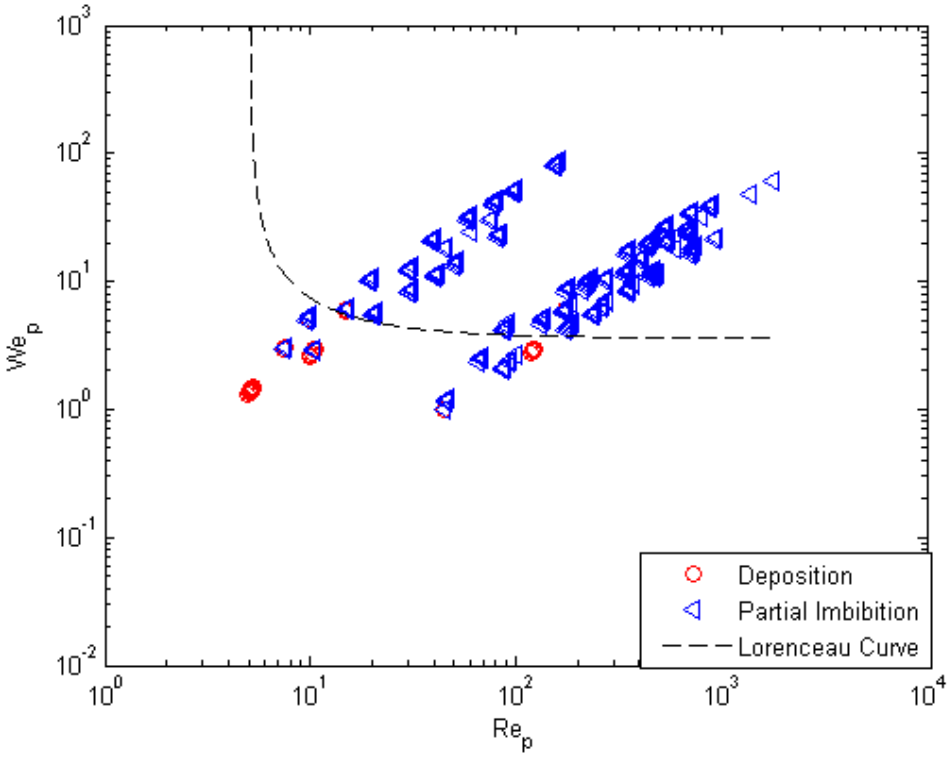

Fig. 100 Threshold velocity for capture: comparison with our results (suspended meshes) [73]

4.2.3 Conclusions

For the case of a suspended mesh, 3 regimes were defined which are deposition, partial imbibition and penetration. The splash outcome is not observable, due to the fastest penetration of the liquid below the meshes right after the impact. This is in agreement with Roisman et al.[35] who pointed out that the upper deposition limit for the splash is influenced by porosity, because of the penetration of the drops inside the substrate.

The result presents a good agreement with Lorenceau et al.[73], in fact, given the same pore dimension but increasing the velocity a transition occurs between an outcome for which the liquid is captured by the surface or partially penetrate inside the pore. However even in this case, the comparison cannot be perfect as the experiments of Lorenceau et al.[73], are based on the impact of droplets on a suspended plate with a single hole which will have a difference influence on the phenomena respect to the mesh with multiple pores.

Considering the work of Brunet et al. [79] also in our case, it is possible to find a correlation between the dimension and number of the daughter droplets eject below the meshes respect to the dimension of the pore and the value of the impact velocity. A higher impact velocity will lead to the formation of a higher number of droplets after the impact.

As Xu et al. [77] pointed out already, it is not possible to define a dimensionless number N, to determine the impact velocity for which the liquid penetration below the mesh will occur. In fact, using a wide range of pore size and, in our case, different liquid properties, the value of the critical impact velocity for which penetration will occur, will not be influenced only from the initial diameter of the droplet and mesh geometry. The results are summarised in Table 28

Table 28
Suspended meshes, results summary.

Work	Research topic	Main findings	Comparison with our work
Roisman et al. [35]	Analysis of different regimes of splash threshold focusing on substrate roughness and randomly porous surfaces.	The impact of droplets on a porous material can be described by Weber number and a ratio given by considering the geometrical roughness. In the case of porous substrates, drops deposition without splash is more probable because of the penetration of the drops inside the substrate.	For the case of a suspended mesh, 3 regimes were defined which are deposition, partial imbibition and penetration. The splash outcome is not observable, due to the fastest penetration of the liquid below the meshes right after the impact. This is in agreement with Roisman et al.[35] who pointed out that the upper deposition limit for the splash is influenced by porosity, because of the penetration of the drops inside the substrate.
Lorenceau et al.[73]	Impact of droplet against thin plates pierced with small holes.	Definition of a velocity threshold for which penetration of the liquids occurs.	In agreement with Lorenceau et al [73], our results show that given the same pore dimension but increasing the velocity a transition occurs between an outcome for which the liquid is captured by the surface or partially penetrate inside the pore.
Brunet et al. [79]	Water droplet impact on hydrophobic microgrid with trapezoidal pores.	Above a threshold speed, liquid emerges on the other side of the grid forming microdroplets and proposed a model to produce monodisperse spray. The general trend shows an increase of droplets number at larger We.	Considering the work of Brunet et al. [77] also in our case, it is possible to find a correlation between the dimension and number of the daughter droplets ejected below the meshes respect to the dimension of the pore and the value of the impact velocity. A higher impact velocity will lead to the formation of a higher number of droplets after the impact.
Xu et al. [77]	Impact of droplet on mesh membrane which are a	Their analysis shows that the liquid penetration is related to the number of	As Xu et al. [75] pointed out already, it is not possible to define a dimensionless number N, to determine the impact velocity for which the liquid penetration below the mesh will occur. In fact, using a wide

	functional material for gas-water or oil-water separation.	mesh pores within drop project area, N. A higher value of N will lead to a smaller critical velocity for which the penetration occurs.	range of pore size and, in our case, different liquid properties, the value of the critical impact velocity for which penetration will occur, will not be influenced only from the initial diameter of the droplet and mesh geometry.

5 Conclusion

This study focused on the investigation of droplet impact on metallic meshes with a wide range of pore sizes. Two main configurations were chosen to analyse separately the effect of porosity and point out the impregnation properties of the mesh and how it is influenced by liquid properties.

The experiments were performed with three different liquids to investigate the effect of the fluids' physical properties: water, acetone and a solution of water and glycerol. The mesh pore dimension and wire diameter have a range of respectively 25-400 μm and 25-220 μm. To obtain a range of impact velocity between 2 m/s and 4 m/s, the height of release was varied between 20 cm and 80 cm. The droplet was released from the needle exclusively thanks to gravity force. Two different needle sizes, 21 gauge, (0.82 mm OD, 0.51 mm ID) and 26s gauge (0.47 mm OD, 0.13 mm ID) were used to vary the drop diameter in a range of 1.5-3.0 mm.

5.1 Attached meshes: main findings

In the first part of the experiments, the meshes were carefully attached on a stainless-steel surface, to reduce the movement of the mesh. In this way it was possible to isolate the effect of porosity without needing to account for the influence of elasticity and surface displacement.

By observing the result of the experiments, 6 different outcomes were defined.

For low velocity impacts, these outcomes are: deposition, partial imbibition and mesh penetration.

For high velocity impacts, the same outcomes were observed, but with possible transition to a splash regime, which is still characterised by a final deposition, a partial imbibition and a penetration.

In the case of the deposition, the droplet, after the impact, remains completely above the surface after the spreading and the recoiling. For the partial imbibition, part of the liquid penetrates below the surface during the recoiling.

On the other side the penetration is an instantaneous process and no spreading is detected because all the liquid penetrates under the surface right after the impact.

As mentioned earlier, in the case of full penetration, no spreading occurs, consequently a dimensionless time was defined to separate the events that occur in the initial phase from the events which occur after.

In the case of complete penetration, considering the instant the droplet touches the surface, the time required for the first half of the spherical droplet to penetrate inside the surface will be given by

$$t_p = \frac{d}{2v_i}$$

This time leads to dimensionless value equal to

$$t_p^* = \frac{t_p v_i}{d} = \frac{1}{2} = 0.5$$

The initial phase, $t^*<0.5$, defines the separation between deposition and the complete penetration of the droplet inside the surface. For $t^*>0.5$, a second regime map is proposed, defining the transition between deposition and partial imbibition. The attempt to represent the different outcome regimes without a geometrical parameter referring to mesh wire diameter was not satisfactory to obtain a proper identification of regimes. In addition, to distinctly discriminate between the deposition and penetration impact regimes, it is essential to refer to a dimensionless number that accounts for the liquid's physical properties, specifically, the viscosity and the surface tension. To achieve this, we have introduced two new dimensionless parameters, $\boldsymbol{M}$ and γ, which provides some prediction of impact outcomes for our range of experimental conditions. $\boldsymbol{M}$ and γ, are respectively defined as

$$M = Re^{0.8} We^{2.1}$$

$$\gamma = \left(1 + \frac{D_w}{D_p}\right)^2$$

where Re and We are respectively the Reynolds and Weber numbers and D_w and D_p the wire and pore diameter.

Given these dimensionless numbers, our results show that, in contradiction to the findings of Roisman et al. [35], the two most important parameters to describe the impact of droplets on a porous material may not be just the Weber number and a ratio given by considering the geometrical roughness. This difference could be explained by the fact that the surfaces used by Roisman et al. [35] present an irregular porosity that could affect the final outcome.

Our results show a good agreement with Sahu et al.[69] who pointed out that the penetration of the liquid into the pores will occur if the dynamics pressure is higher than the capillary pressure ($p_d \gg p_c$), but also in the case of hydrodynamics phenomena for which the penetration of the droplet into the pores is enhanced if the diameter of the droplet is larger than the pore diameter ($d \gg D_p$). Considering the dimension of the droplets, much bigger than the pores as for the case of our experiments and observing the penetration outcome we can conclude that the hydrodynamics phenomena plays a major role.

It was found that the roughness factor r introduced by Sivakumar et al. [101], well described also the spreading on the metallic porous mesh, considering the wire diameter as a measure of roughness.

The deposition-penetration threshold defined by Lorenceau et al. [73], cannot perfectly describe the separation of our regimes because the set up presented by them is different from the one used in our experiments. Having a plate with a single hole will affect in a different way the outcome of the experiments.

Summarising the results, it is possible to point out the following findings:

- The effect of porosity on droplet impact was analysed, considering a wide range of pore size and wire diameter.
    - Pore dimension: given the same impact velocity and liquid properties, a larger pore size will enhance liquid penetration.
    - Impact velocity: given the same pore dimension and liquid properties, a higher impact velocity will enhance liquid penetration.
    - Higher viscosity: given the same pore dimension and impact velocity, a higher viscosity will enhance the deposition outcome.
    - Lower surface tension: given the same pore dimension and impact velocity, a lower surface tension will lead to a higher penetration.
- The spreading analysis leads to an estimation of the percentage of liquid which penetrates below the mesh. It was pointed out that porosity will affect the spreading and the maximum spreading diameter will be lower for larger pore size, due to a larger percentage of liquid penetration.
- Two different maps were defined to separate the different regimes (Fig. 101 -Fig. 102).

- A characteristic time t_p^* was defined for which penetration occurs. Due to the different time scale it is necessary to analyse separately the regimes transition.

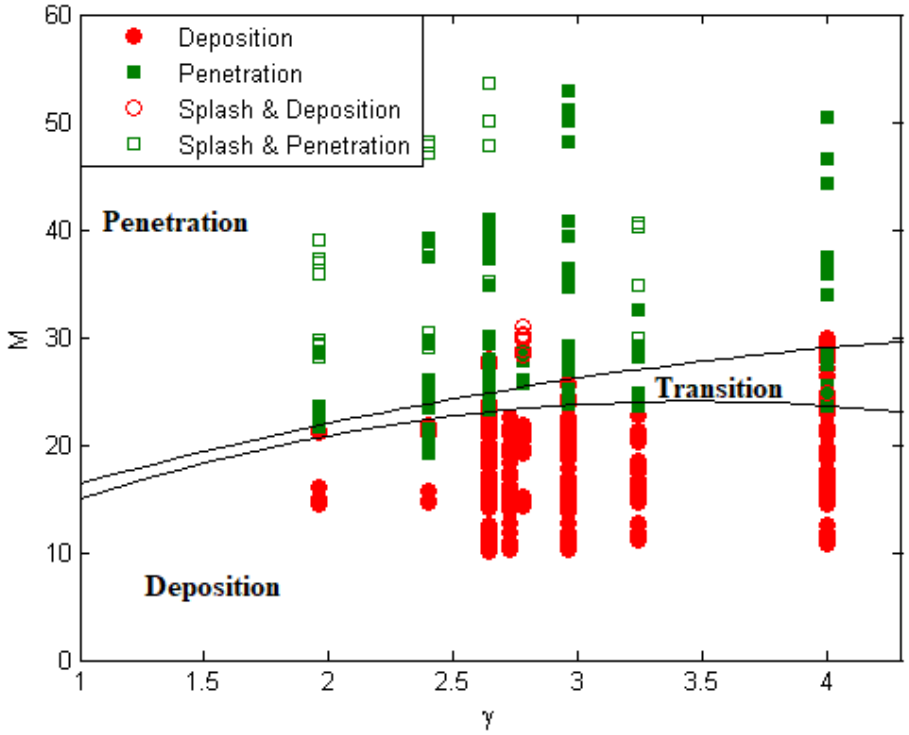

Fig. 101 Regime distribution for all the liquids as a function of γ and M, transition between deposition and penetration.

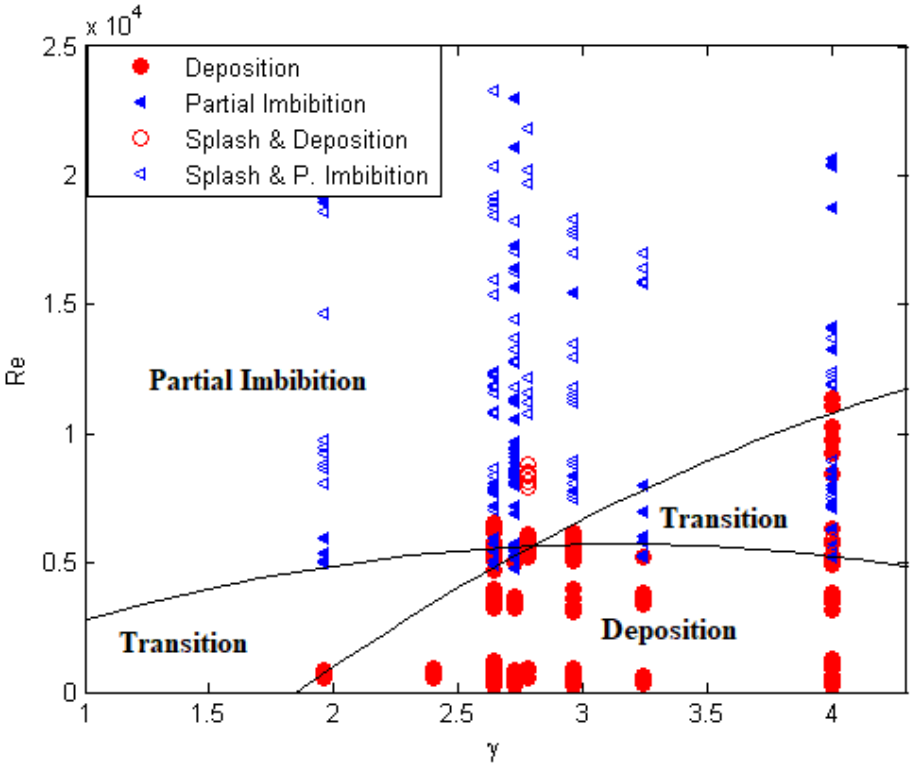

Fig. 102 Regime distribution for all the liquids as a function of γ and Re with the transition between deposition and imbibition

5.2 Suspended meshes: main findings

In the second configuration, a portion of the mesh was suspended using initially a ring with a 20 mm inner diameter to quantify better the impregnation properties of the surface and remark how it is influenced by mesh geometry, liquid properties and impact velocity. It was observed that at higher impact velocities a small vertical movement of the mesh occurred after the impact of the droplet. To verify if the amplitude of the oscillation can influence the outcome, some of the experiments were repeated using 2 more rings with diameters of 15 mm and 25 mm, which offered smaller and larger unclamped area for the suspended mesh compared to the original case. It was observed that there is no significant difference in terms of outcome and percentage penetration for any of the considered liquid. It is possible to conclude that the movement of the mesh has no relevant effect on the nature of the outcome.

No splash outcome was observed in the case of the suspended meshes. This is due to the fact that at higher impact velocities, which normally leads to splash, a higher percentage of liquid penetrates below the surface. This is in agreement with

Roisman et al. [35] who pointed out that the upper deposition limit for the splash is influenced by porosity, because of the penetration of the drops inside the substrate.

It was confirmed that the liquid properties and the geometry of the meshes play a role in the definition of the outcome. The results are partially in agreement with Lorenceau et al. [73], in fact, given the same pore dimension but increasing the velocity it is possible to observe a transition between an outcome for which the liquid is captured by the surface or partially penetrate inside the pore. However, the threshold velocity limit described by them cannot perfectly separates our results due to the different set up they used characterised by a plate with a single hole. As for the research of Xu et al. [77], it was shown that a number N, given by a ratio of the projected area of a droplet before the impact and the single pore area, does not always leads to a satisfactory estimation of the critical impact velocity for which penetration occurs. In fact, considering for example different liquid properties, it was shown that in the case of water and water and glycerol, given the same mesh geometrical dimension and droplet initial diameter, consequently the same N, because of the higher viscosity, penetration will occur for a higher impact velocity.

Summarising the results, it is possible to point out the following findings:

- The impregnation properties of the mesh were estimated.
    - Impact velocity: given the same pore dimension and liquid properties, a higher impact velocity will lead to a higher percentage of liquid penetration (Fig. 103)
    - Higher viscosity: given the same pore dimension and impact velocity, a higher viscosity will lead to a lower percentage of liquid penetration, enhancing the deposition outcome (Fig. 104)
    - Lower surface tension: given the same pore dimension and impact velocity, a lower surface tension will lead to a higher penetration enhancing the penetration outcome (Fig. 1058)
- A portion of the mesh was suspended using different ring sizes. It was shown that the vertical movement of the mesh doesn’t affect critically the outcome and the liquid penetration.

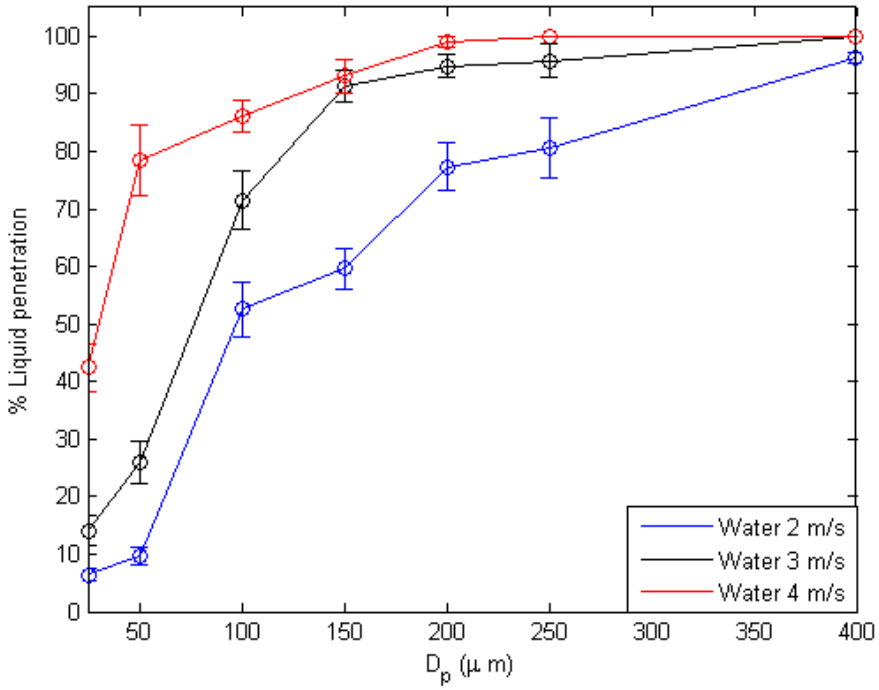

Fig. 97 Percentage of liquid penetration of water as a function of pore size given different range of impact velocity

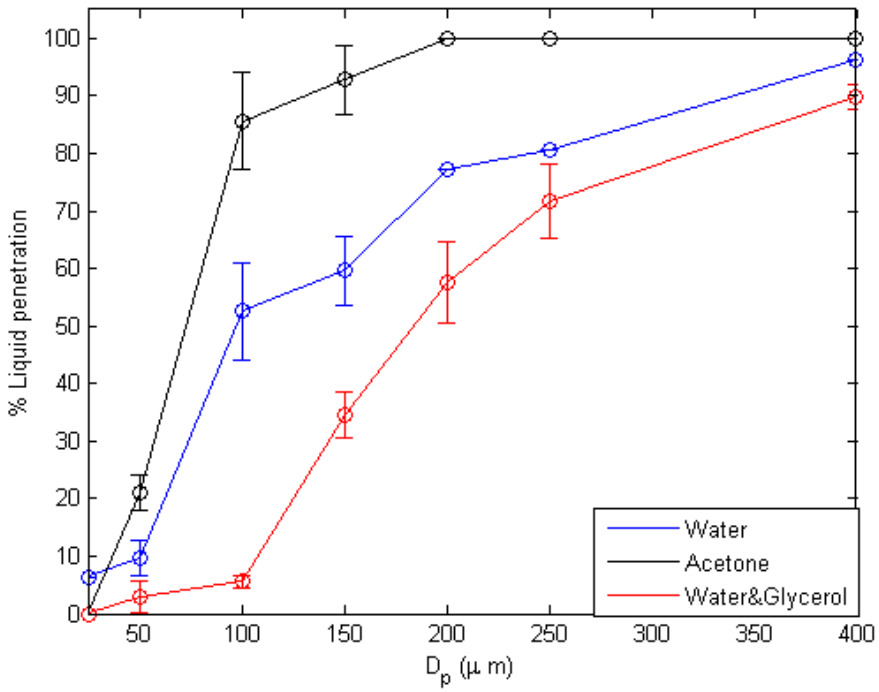

Fig. 98 Percentage of liquid penetration of water, acetone, water & glycerol at 2 m/s as a function of pore size.

It was shown that the impregnation properties of the mesh, which also gives an estimation of the percentage of liquid that is maintained above the surface without ejection, can vary under specific condition of mesh geometry or physical parameter. The experiments show that the complete deposition of the liquid above the surface is more probable for smaller pores size, higher viscosity, lower impact velocity and smaller initial droplet diameter.

5.3 Future works

Considering the medical field, the literature shows that several studies were done in the tissue engineering field analysing tissue ingrown process on meshes and scaffolds with different geometrical and physical properties. A better understanding of which is the combination in terms of best pore dimension and liquid physical properties to enhance cells and tissue proliferation, has a critical importance for the development of tissue engineering technology to repairing damaged dermis. Moreover, considering a medical application, to analyse the interaction between a spray with a skin, a deeper study should be done considering droplets with a diameter of an order of magnitude more similar to pores dimension. A different kind of outcomes could be expected in this case. It is also advice to perform a numerical study of droplet impact on metallic mesh, in particular in the case of the suspended mesh. A numerical study would allow to have a better understanding of the percentage of liquid penetration in time and the influence that the vertical movement of the mesh may have on the impact outcome. In the case of the attached meshes, a numerical study could allow a better understanding of the air entrainment effect.

Appendix

The code operates defining two different domains, one for deposition, one for penetration with a certain number of elements. 4 matrices of distance are defined, considering the distance of each element from all the other elements of the same domain, and each element from all the other elements of the different domain. From the matrices it is possible to determine the vector of average distance of each element respect to all the other elements of the same domain and all the other elements of the different domain. If a given element is in average closer to elements of the different domain respect to the elements of the same domain, it is evaluated as an error, as it should belong to the other domain. The best group of exponential values is the one that leads to a smaller number of errors (points that should belong to the other domain).

Finally, the code analyses the distance between the orthocentre of the 2 domains to select the couple of exponentials that will maximise the distance between the orthocentres and consequently will lead to a better separation between the 2 domains.

1) Definition of 2 domains for Deposition **d** and Penetration **p** with **k** and **m** elements respectively.

$$d(k,2) = \left(x_j, y_j\right)^d$$

$$p(m,2) = \left(x_j, y_j\right)^p$$

2) Definition of 4 matrix of distance.

Matrix 1→ Distance of each element of domain d, respect to all the other elements of domain d

$$D_1^{d\to d}[k \text{ x } k] = d_{j,n}^{d\to d} = \sqrt{\left(x_j^d - x_n^d\right)^2 + \left(y_j^d - y_n^d\right)^2} =$$

$$\begin{bmatrix} d_{11}^{d\to d} = 0 & d_{21}^{d\to d} \cdots & d_{k1}^{d\to d} \\ d_{12}^{d\to d} & d_{22}^{d\to d} = 0 & \vdots \\ d_{1k}^{d\to d} & \cdots & d_{kk}^{d\to d} = 0 \end{bmatrix}$$

Matrix 2→ Distance of each element of domain d, respect to all the other elements of domain p

$$D_2^{d\to p}[k \text{ x } m] = d_{j,n}^{d\to p} = \sqrt{\left(x_j^d - x_n^p\right)^2 + \left(y_j^d - y_n^p\right)^2} =$$

$$\begin{bmatrix} d_{11}^{d\to p} & d_{21}^{d\to p} \cdots & d_{k1}^{d\to p} \\ d_{12}^{d\to p} & d_{22}^{d\to p} & \vdots \\ d_{1m}^{d\to p} & \cdots & d_{km}^{d\to p} \end{bmatrix}$$

Matrix 3→ Distance of each element of domain p, respect to all the other elements of domain p

$$D_3^{p\to p}[m \text{ x } m] = d_{j,n}^{p\to p} = \sqrt{\left(x_j^p - x_n^p\right)^2 + \left(y_j^p - y_n^p\right)^2} =$$

$$\begin{bmatrix} d_{11}^{p\to p} = 0 & d_{21}^{p\to p} \cdots & d_{m1}^{p\to p} \\ d_{12}^{p\to p} & d_{22}^{p\to p} = 0 & \vdots \\ d_{1m}^{p\to p} & \cdots & d_{mm}^{p\to p} = 0 \end{bmatrix}$$

Matrix 4→ Distance of each element of domain p, respect to all the other elements of domain d

$$D_4^{p\to d}[m \text{ x } k] = d_{j,n}^{p\to d} = \sqrt{\left(x_j^p - x_n^d\right)^2 + \left(y_j^p - y_n^d\right)^2} =$$

$$\begin{bmatrix} d_{11}^{p\to d} & d_{21}^{p\to d} \cdots & d_{m1}^{p\to d} \\ d_{12}^{p\to d} & d_{22}^{p\to d} & \vdots \\ d_{1k}^{p\to d} & \cdots & d_{mk}^{p\to d} \end{bmatrix}$$

3) Definition of 4 vectors of mean distance

Definition of vectors of mean distance of each element of domain d respect to all the other elements of domain d

$$\overline{D_1}^{d\to d}(k) = \bar{d}_j^{d\to d} = \frac{1}{k}\sum\left(d_{j,n}^{d\to d}\right)$$

$$= \left[\frac{1}{k}\sum_{n=1}^{k}\left(d_{1,n}^{d\to d}\right) \quad \frac{1}{k}\sum_{n=1}^{k}\left(d_{2,n}^{d\to d}\right) \quad \ldots \frac{1}{k}\sum_{n=1}^{k}\left(d_{k,n}^{d\to d}\right)\right]$$

Definition of vectors of mean distance of each element of domain d respect to all the other elements of domain p

$$\overline{D_2}^{d\to p}(k) = \bar{d}_j^{d\to p} = \frac{1}{k}\sum\left(d_{j,n}^{d\to p}\right)$$

$$= [\frac{1}{k}\sum_{n=1}^{k}\left(d_{1,n}^{d\to p}\right) \quad \frac{1}{k}\sum_{n=1}^{k}\left(d_{2,n}^{d\to p}\right) \quad \ldots \frac{1}{k}\sum_{n=1}^{k}\left(d_{k,n}^{d\to p}\right)]$$

Definition of vectors of mean distance of each element of domain p respect to all the other elements of domain p.

$$\overline{D_3}^{p\to p}(m) = \bar{d}_j^{p\to p} = \frac{1}{m}\sum\left(d_{j,n}^{p\to p}\right)$$

$$= [\frac{1}{m}\sum_{n=1}^{m}\left(d_{1,n}^{p\to p}\right) \quad \frac{1}{m}\sum_{n=1}^{m}\left(d_{2,n}^{p\to p}\right) \quad \ldots \frac{1}{m}\sum_{n=1}^{m}\left(d_{m,n}^{p\to p}\right)]$$

Definition of vectors of mean distance of each element of domain p respect to all the other elements of domain d

$$\overline{D_4}^{p\to d}(m) = \bar{d}_j^{p\to d} = \frac{1}{m}\sum\left(d_{j,n}^{p\to d}\right)$$

$$= [\frac{1}{m}\sum_{n=1}^{m}\left(d_{1,n}^{p\to d}\right) \quad \frac{1}{m}\sum_{n=1}^{m}\left(d_{2,n}^{p\to d}\right) \quad \ldots \frac{1}{m}\sum_{n=1}^{m}\left(d_{m,n}^{p\to d}\right)]$$

4) Definition of vectors of difference between the mean distance vectors

Definition of vectors of difference between $\overline{D_1}^{d\to d}(k)$ and $\overline{D_2}^{d\to p}(k)$

$$Dif^{d}(k) = \overline{D_1}^{d\to d}(k) - \overline{D_2}^{d\to p}(k) = \frac{1}{k}\sum\left(d_{j,n}^{d\to d}\right) - \frac{1}{k}\sum\left(d_{j,n}^{d\to p}\right)$$

$$= [\frac{1}{k}\sum_{n=1}^{k}\left(d_{1,n}^{d\to d}\right) - \frac{1}{k}\sum_{n=1}^{k}\left(d_{1,n}^{d\to p}\right) \ldots \frac{1}{k}\sum_{n=1}^{k}\left(d_{k,n}^{d\to d}\right)$$

$$-\frac{1}{k}\sum_{n=1}^{k}\left(d_{k,n}^{d\to p}\right)] \quad = [dif_1^d \quad dif_2^d \quad \ldots . dif_k^d]$$

Definition of vectors of difference between $\overline{D_3}^{p\to p}(m)$ and $\overline{D_4}^{p\to d}(m)$

$$Dif^{p}(m) = \overline{D_3}^{p\to p}(m) - \overline{D_4}^{p\to d}(m) = \frac{1}{m}\sum\left(d_{j,n}^{p\to p}\right) - \frac{1}{m}\sum\left(d_{j,n}^{p\to d}\right)$$

$$= [\frac{1}{m}\sum_{n=1}^{m}\left(d_{1,n}^{p\to p}\right) - \frac{1}{m}\sum_{n=1}^{m}\left(\mathrm{d}_{1,\mathrm{n}}^{\mathrm{d}\to\mathrm{p}}\right) \ldots \frac{1}{\mathrm{m}}\sum_{\mathrm{n}=1}^{\mathrm{m}}\left(\mathrm{d}_{\mathrm{m,n}}^{\mathrm{d}\to\mathrm{d}}\right)$$

$$-\frac{1}{\mathrm{m}}\sum_{\mathrm{n}=1}^{\mathrm{m}}\left(\mathrm{d}_{\mathrm{m,n}}^{\mathrm{d}\to\mathrm{p}}\right)] \quad = [\mathrm{dif}_1^{\mathrm{p}} \quad \mathrm{dif}_2^{\mathrm{p}} \ldots . \mathrm{dif}_{\mathrm{k}}^{\mathrm{p}}]$$

5) Definition of the "theoretical" new regimes considering the element s in the wrong domain

If $\mathrm{dif}^{\mathrm{d}}(\mathrm{j}) > 0$, the j point in the deposition domain, is in average closer to the points of the penetration domain. The j point should belong to the penetration domain.
If $\mathrm{dif}^{\mathrm{p}}(\mathrm{j}) > 0$ the j point in the penetration domain, is in average closer to the points of the deposition domain. The j point should belong to the deposition domain.

$$\mathrm{dif}^{\mathrm{d}}(\mathrm{j}) > 0 \;\Rightarrow \left(\mathrm{x_j}, \mathrm{y_j}\right)^{\mathrm{d}} \in \mathrm{p}$$

$$\mathrm{dif}^{\mathrm{p}}(\mathrm{j}) > 0 \;\Rightarrow \left(\mathrm{x_j}, \mathrm{y_j}\right)^{\mathrm{p}} \in \mathrm{d}$$

The best group of exponential values is the one that leads to a smaller number of errors (points that should belong to the other domain).

6) Maximizing the distance of the orthocentre of the 2 domains.

Defining the orthocentre of the deposition domain.

$$\mathrm{d_o}(\mathrm{x}, \mathrm{y}) = \mathrm{d}(\frac{1}{\mathrm{k}}\sum_{\mathrm{j}=1}^{\mathrm{k}}\left(\mathrm{x_j}\right)^{\mathrm{d}}, \frac{1}{\mathrm{k}}\sum_{\mathrm{j}=1}^{\mathrm{k}}\left(\mathrm{y_j}\right)^{\mathrm{d}})$$

Defining the orthocentre of the penetration domain.

$$p_o(x,y) = d(\frac{1}{m}\sum_{j=1}^{m}(x_j)^p, \frac{1}{m}\sum_{j=1}^{m}(y_j)^p)$$

Defining the distance between the orthocentres of the two domains.

$$\text{distance}_o = \sqrt{(d_o(x) - p_o(x))^2 + (d_o(y) - p_o(y))^2}$$

The best couple of exponential values will maximise the distance between the orthocentres and consequently will lead to a better separation between the 2 domains.

Nomenclature

p_c	Capillary pressure [Pa]	
σ	Surface tension [N/m]	
ρ	Liquid density [kg/m^3]	
μ	Viscosity [Pa s]	
D_p	Pore diameter [m]	
D_w	Wire diameter [m]	
d	Droplet diameter [m]	
v_i	Impact velocity [m/s]	
t	Time [s]	
$d(t)^*$	$\frac{d(t)}{d}$	dimensionless diameter
t^*	$\frac{tv_i}{d(t)}$	
We	$\frac{\rho v_i^2 d}{\sigma}$	Weber number based on drop diameter
We_p	$\frac{\rho v_i^2 D_p}{\sigma}$	Weber number
Re	$\frac{\rho v_i d}{\mu}$	Reynolds number based on drop diameter
Re_p	$\frac{\rho v_i \ D_p}{\mu}$	Reynolds number
Ca	$\frac{We}{Re}$	Capillary number
Oh	$\frac{\sqrt{We}}{Re}$	Ohnesorge number
β	$\frac{D_p}{d}$	
γ	$\left(1+\frac{D_w}{D_p}\right)$	
M	$Re^{0.8}We^{2.1}$	

Bibliography

[1] F. Boyer, E. Sandoval-Nava, J. H. Snoeijer, J. F. Dijksman, and D. Lohse, "Drop impact of shear thickening liquids," *Phys. Rev. Fluids*, vol. 1, no. 1, pp. 1–9, 2016.

[2] M. Marengo, C. Antonini, I. V. Roisman, and C. Tropea, "Drop collisions with simple and complex surfaces," *Curr. Opin. Colloid Interface Sci.*, vol. 16, no. 4, pp. 292–302, 2011.

[3] C. Josserand and S. T. Thoroddsen, "Drop Impact on a Solid Surface," *Annu. Rev. Fluid Mech.*, vol. 48, no. 1, pp. 365–391, 2016.

[4] D. M. Harris, T. Liu, and J. W. M. Bush, "A low-cost, precise piezoelectric droplet-on-demand generator," *Exp. Fluids*, vol. 56, no. 4, pp. 1–7, 2015.

[5] V. Bertola, "Some Applications of Controlled Drop Deposition on Solid Surfaces," *Recent Patents Mech. Eng.*, vol. 1, no. 3, pp. 167–174, 2008.

[6] A. C. Wright, "A physically-based model of the dispersion of splash droplets ejected from a water drop impact," *Earth Surf. Process. Landforms*, vol. 11, no. 4, pp. 351–367, 1986.

[7] J. M. Gac, A. Jackiewicz, Ł. Werner, and S. Jakubiak, "Consecutive filtration of solid particles and droplets in fibrous filters," *Sep. Purif. Technol.*, vol. 170, pp. 234–240, 2016.

[8] J. Luo, W. Wang, W. Xiong, H. Shen, and L. Qi, "Formation of uniform metal traces using alternate droplet printing," *Int. J. Mach. Tools Manuf.*, vol. 122, no. December 2016, pp. 47–54, 2017.

[9] C. Guiot, P. P. Delsanto, and T. S. Deisboeck, "Morphological instability and cancer invasion: A 'splashing water drop' analogy," *Theor. Biol. Med. Model.*, vol. 4, 2007.

[10] "[46]Documentary Research of Human Respiratory Droplet Characteristics (PDF Download Available).pdf." .

[11] Y. Li, D. Guan, C. Wu, and C. Guo, "An Experimental Study on the Transmission of Respiratory Droplet Aerosol Using the Available Agent in an Enclosed Chamber," *Procedia Eng.*, vol. 205, pp. 2365–2369, 2017.

[12] C. Antonini, S. Jung, A. Wetzel, E. Heer, P. Schoch, A. M. Moqaddam, S. S. Chikatamarla, I. Karlin, M. Marengo, and D. Poulikakos, "Contactless

prompt tumbling rebound of drops from a sublimating slope," *Phys. Rev. Fluids*, vol. 1, no. 1, pp. 1–11, 2016.

[13] K. P. Gatne, M. A. Jog, and R. M. Manglik, "Surfactant-induced modification of low weber number droplet impact dynamics," *Langmuir*, vol. 25, no. 14, pp. 8122–8130, 2009.

[14] S. E. Bechtel, D. B. Bogy, and F. E. Talke, "Impact of a Liquid Drop Against a Flat Surface," *IBM J. Res. Dev.*, vol. 25, no. 6, pp. 963–971, 1981.

[15] R. Crooks, J. Cooper-White, and D. V. Boger, "The role of dynamic surface tension and elasticity on the dynamics of drop impact," *Chem. Eng. Sci.*, vol. 56, no. 19, pp. 5575–5592, 2001.

[16] C. Mundo, M. Sommerfeld, and C. Tropea, "Droplet-wall collisions: Experimental studies of the deformation and breakup process," *Int. J. Multiph. Flow*, vol. 21, no. 2, pp. 151–173, 1995.

[17] M. J. Wang, Y. L. Hung, F. H. Lin, and S. Y. Lin, "Dynamic behaviors of droplet impact and spreading: A universal relationship study of dimensionless wetting diameter and droplet height," *Exp. Therm. Fluid Sci.*, vol. 33, no. 7, pp. 1112–1118, 2009.

[18] C. Ukiwe and D. Y. Kwok, "On the maximum spreading diameter of impacting droplets on well-prepared solid surfaces," *Langmuir*, vol. 21, no. 2, pp. 666–673, 2005.

[19] S. M. An and S. Y. Lee, "Maximum spreading of a shear-thinning liquid drop impacting on dry solid surfaces," *Exp. Therm. Fluid Sci.*, vol. 38, pp. 140–148, 2012.

[20] A. Saïdi, C. Martin, and A. Magnin, "Influence of yield stress on the fluid droplet impact control," *J. Nonnewton. Fluid Mech.*, vol. 165, no. 11–12, pp. 596–606, 2010.

[21] R. Rioboo, M. Marengo, and C. Tropea, "Time evolution of liquid drop impact onto solid, dry surfaces," *Exp. Fluids*, vol. 33, no. 1, pp. 112–124, 2002.

[22] C. Lee, H. Kim, and Y. Nam, "Drop impact dynamics on oil-infused nanostructured surfaces," *Langmuir*, vol. 30, no. 28, pp. 8400–8407, 2014.

[23] S. R. L. Werner, J. R. Jones, A. H. J. Paterson, R. H. Archer, and D. L. Pearce, "Droplet impact and spreading: Droplet formulation effects," *Chem. Eng. Sci.*, vol. 62, no. 9, pp. 2336–2345, 2007.

[24] M. Pasandideh-Fard, Y. M. Qiao, S. Chandra, and J. Mostaghimi, “Capillary effects during droplet impact on a solid surface,” *Phys. Fluids*, vol. 8, no. 650, 1996.

[25] D. C. D. Roux and J. J. Cooper-White, “Dynamics of water spreading on a glass surface,” *J. Colloid Interface Sci.*, vol. 277, no. 2, pp. 424–436, 2004.

[26] M. Toivakka, “Numerical investigation of froplet impact spreading in spray coating of paper,” *2003 Spring Adv. Coat. Fundam. Symp.*, 2003.

[27] A. V. Mahulkar, G. B. Marin, and G. J. Heynderickx, “Droplet-wall interaction upon impingement of heavy hydrocarbon droplets on a heated wall,” *Chem. Eng. Sci.*, vol. 130, no. July, pp. 275–289, 2015.

[28] C. Tang, M. Qin, X. Weng, X. Zhang, P. Zhang, J. Li, and Z. Huang, “Dynamics of droplet impact on solid surface with different roughness,” *Int. J. Multiph. Flow*, vol. 96, pp. 56–69, 2017.

[29] T. Mao, T. Mao, D. C. S. Kuhn, and H. Tran, “Spread and Rebound of Liquid Droplets upon Impact on Flat Surfaces Spread and Rebound of Liquid Droplets upon Impact on Flat Surfaces,” vol. 4, no. August 2015, pp. 2169–2179, 1997.

[30] R. Rioboo, C. Tropea, and M. Marengo, “Outcomes From a Drop Impact on Solid Surfaces,” *At. Sprays*, vol. 11, no. 2, p. 12, 2001.

[31] J. Xie, J. Xu, W. Shang, and K. Zhang, “Mode selection between sliding and rolling for droplet on inclined surface : Effect of surface wettability International Journal of Heat and Mass Transfer Mode selection between sliding and rolling for droplet on inclined surface : Effect of surface wettability,” *Int. J. Heat Mass Transf.*, vol. 122, no. October, pp. 45–58, 2018.

[32] A. L. Yarin, “DROP IMPACT DYNAMICS: Splashing, Spreading, Receding, Bouncing…,” *Annu. Rev. Fluid Mech.*, vol. 38, no. 1, pp. 159–192, 2006.

[33] J. Palacios, P. Gómez, C. Zanzi, J. López, and J. Hernández, “Experimental study on the splash / deposition limit in drop impact onto solid surfaces,” *ILASS-Europe 2010, 23rd Annu. Conf. Liq. At. Spray Syst. Brno, Czech Repub.*, no. September, pp. 1–7, 2010.

[34] a Gipperich, an Lembach, I. Roisman, and C. Tropea, “On the splashing threshold of a single droplet impacting onto rough and porous surfaces,”

Proc. 23rd ILASS-2010, no. September, pp. 2–7, 2010.

[35] I. V. Roisman, A. Lembach, and C. Tropea, "Drop splashing induced by target roughness and porosity: The size plays no role," *Adv. Colloid Interface Sci.*, vol. 222, pp. 615–621, 2015.

[36] G. E. Cossali, A. Coghe, and M. Marengo, "The impact of a single drop on a wetted solid surface," *Exp. Fluids*, vol. 22, no. 6, pp. 463–472, 1997.

[37] C. Tropea and M. Marengo, "the Impact of Drops on Walls and Films," *Multiph. Sci. Technol.*, vol. 11, no. 1, pp. 19–36, 1999.

[38] W. S. Kim and S. Y. Lee, "Behavior of a water drop impinging on heated porous surfaces," *Exp. Therm. Fluid Sci.*, vol. 55, pp. 62–70, 2014.

[39] G. Cossali, G. Brunello, a. Coghe, and M. Marengo, "Impact of a single drop on a liquid film: experimental analysis and comparison with empirical models," *Ital. Congr. Thermofluid Dyn. UIT, Ferrara*, vol. 30, no. July, p. 12, 1999.

[40] M. Cheng and J. Lou, "A numerical study on splash of oblique drop impact on wet walls," *Comput. Fluids*, vol. 115, pp. 11–24, 2015.

[41] Z. Romdhani, A. Baffoun, M. Hamdaoui, and S. Roudesli, "Drop impact on textile material: Effect of fabric properties," *Autex Res. J.*, vol. 14, no. 3, pp. 145–151, 2014.

[42] R. Rioboo, M. Voué, H. Adão, J. Conti, A. Vaillant, D. Seveno, and J. De Coninck, "Drop impact on soft surfaces: Beyond the static contact angles," *Langmuir*, vol. 26, no. 7, pp. 4873–4879, 2010.

[43] C. Clanet, C. Béguin, D. Richard, and D. Quéré, "Maximal deformation of an impacting drop," *J. Fluid Mech.*, vol. 517, pp. 199–208, 2004.

[44] K. Y. Yeh, L. J. Chen, and J. Y. Chang, "Contact angle hysteresis on regular pillar-like hydrophobic surfaces," *Langmuir*, vol. 24, no. 1, pp. 245–251, 2008.

[45] I. Malgarinos, N. Nikolopoulos, M. Marengo, C. Antonini, and M. Gavaises, "VOF simulations of the contact angle dynamics during the drop spreading: Standard models and a new wetting force model," *Adv. Colloid Interface Sci.*, vol. 212, pp. 1–20, 2014.

[46] R. Zhang, S. Farokhirad, T. Lee, and J. Koplik, "Multiscale liquid drop impact on wettable and textured surfaces," *Phys. Fluids*, vol. 26, no. 8, 2014.

[47] X. Xu, Z. Z. Zhang, and J. Yang, "Study on the superhydrophobic

poly(methyl methacrylate)/silver thiolate composite coating with absorption of UVA light," *Colloids Surfaces A Physicochem. Eng. Asp.*, vol. 355, no. 1–3, pp. 163–166, 2010.

[48] X. H. Xu, Z. Z. Zhang, J. Yang, and X. T. Zhu, "Study of the corrosion resistance and loading capacity of superhydrophobic meshes fabricated by spraying method," *Colloids Surfaces A Physicochem. Eng. Asp.*, vol. 377, no. 1–3, pp. 70–75, 2011.

[49] H. J. Butt, I. V. Roisman, M. Brinkmann, P. Papadopoulos, D. Vollmer, and C. Semprebon, "Characterization of super liquid-repellent surfaces," *Curr. Opin. Colloid Interface Sci.*, vol. 19, no. 4, pp. 343–354, 2014.

[50] P. G. Pittoni, Y. Lin, and S. Lin, "Applied Surface Science The impalement of water drops impinging onto hydrophobic / superhydrophobic graphite surfaces : the role of dynamic pressure , hammer pressure and liquid penetration time," *Appl. Surf. Sci.*, vol. 301, pp. 515–524, 2014.

[51] S. Wang and L. Jiang, "Definition of superhydrophobic states," *Adv. Mater.*, vol. 19, no. 21, pp. 3423–3424, 2007.

[52] A. J. B. Milne and A. Amirfazli, "The Cassie equation: How it is meant to be used," *Adv. Colloid Interface Sci.*, vol. 170, no. 1–2, pp. 48–55, 2012.

[53] P. Tsai, S. Pacheco, C. Pirat, L. Lefferts, and D. Lohse, "Drop impact upon micro- and nanostructured superhydrophobic surfaces," 2009.

[54] C. Antonini, A. Amirfazli, and M. Marengo, "Drop impact and wettability: From hydrophilic to superhydrophobic surfaces," *Phys. Fluids*, vol. 24, no. 10, 2012.

[55] C. Antonini, F. Villa, and M. Marengo, "Oblique impacts of water drops onto hydrophobic and superhydrophobic surfaces: Outcomes, timing, and rebound maps," *Exp. Fluids*, vol. 55, no. 4, 2014.

[56] A. Mazloomi Moqaddam, S. S. Chikatamarla, and I. V. Karlin, *Drops bouncing off macro-Textured superhydrophobic surfaces*, vol. 824. 2017.

[57] Y. Liu, L. Moevius, X. Xu, T. Qian, J. M. Yeomans, and Z. Wang, "Pancake bouncing on superhydrophobic surfaces," *Nat. Phys.*, vol. 10, no. 7, pp. 515–519, 2014.

[58] A. Milionis, K. Ghokulla Krishnan, and E. Loth, "Hemolymph drop impact outcomes on surfaces with varying wettability," *Appl. Surf. Sci.*, vol. 345, pp. 36–43, 2015.

[59] T. Gambaryan-Roisman, “Liquids on porous layers: Wetting, imbibition and transport processes,” *Curr. Opin. Colloid Interface Sci.*, vol. 19, no. 4, pp. 320–335, 2014.

[60] P. J. Franks and D. J. Beerling, “Maximum leaf conductance driven by CO2 effects on stomatal size and density over geologic time,” *Proc. Natl. Acad. Sci.*, vol. 106, no. 25, pp. 10343–10347, 2009.

[61] M. Massinon and F. Lebeau, “Experimental method for the assessment of agricultural spray retention based on high-speed imaging of drop impact on a synthetic superhydrophobic surface,” *Biosyst. Eng.*, vol. 112, no. 1, pp. 56–64, 2012.

[62] N. De Cock, M. Massinon, S. O. T. Salah, and F. Lebeau, “Investigation on optimal spray properties for ground based agricultural applications using deposition and retention models,” *Biosyst. Eng.*, vol. 162, pp. 99–111, 2017.

[63] M. A. Mujeebu, M. Z. Abdullah, and A. A. Mohamad, “Development of energy efficient porous medium burners on surface and submerged combustion modes,” *Energy*, vol. 36, no. 8, pp. 5132–5139, 2011.

[64] M. Weclas, “Potential of Porous-Media Combustion Technology as Applied to Internal Combustion Engines,” *J. Thermodyn.*, vol. 2010, pp. 1–39, 2010.

[65] M. Kaplan and M. J. Hall, “The combustion of liquid fuels within a porous media radiant burner,” *Exp. Therm. Fluid Sci.*, vol. 11, no. 1, pp. 13–20, 1995.

[66] P. He, Y. Liu, and R. Qiao, “Fluid dynamics of the droplet impact processes in cell printing,” *Microfluid. Nanofluidics*, vol. 18, no. 4, pp. 569–585, 2015.

[67] S. Chandra and C. T. Avedisian, “Observations of droplet impingement on a ceramic porous surface,” *Int. J. Heat Mass Transf.*, vol. 35, no. 10, pp. 2377–2388, 1992.

[68] J. M. Gac and L. Gradoń, “Modeling of axial motion of small droplets deposited on smooth and rough fiber surfaces,” *Colloids Surfaces A Physicochem. Eng. Asp.*, vol. 414, pp. 259–266, 2012.

[69] R. P. Sahu, S. Sett, A. L. Yarin, and B. Pourdeyhimi, “Impact of aqueous suspension drops onto non-wettable porous membranes: Hydrodynamic focusing and penetration of nanoparticles,” *Colloids Surfaces A Physicochem. Eng. Asp.*, vol. 467, pp. 31–45, 2015.

[70] S. M. Kumar and A. P. Deshpande, “Dynamics of drop spreading on fibrous

porous media," *Colloids Surfaces A Physicochem. Eng. Asp.*, vol. 277, no. 1–3, pp. 157–163, 2006.

[71] J. O. Marston, J. E. Sprittles, Y. Zhu, E. Q. Li, I. U. Vakarelski, and S. T. Thoroddsen, "Drop spreading and penetration into pre-wetted powders," *Powder Technol.*, vol. 239, pp. 128–136, 2013.

[72] A. Clarke, T. D. Blake, K. Carruthers, and A. Woodward, "Surfaces," no. 9, pp. 2980–2984, 2002.

[73] É. Lorenceau and D. Quéré, "Drops impacting a sieve," *J. Colloid Interface Sci.*, vol. 263, no. 1, pp. 244–249, 2003.

[74] K. Piroird, C. Clanet, É. Lorenceau, and D. Quéré, "Drops impacting inclined fibers," *J. Colloid Interface Sci.*, vol. 334, no. 1, pp. 70–74, 2009.

[75] K. Yamamoto, H. Takezawa, and S. Ogata, "Droplet impact on textured surfaces composed of commercial stainless razor blades," *Colloids Surfaces A Physicochem. Eng. Asp.*, vol. 506, pp. 363–370, 2016.

[76] A. Delbos, E. Lorenceau, and O. Pitois, "Forced impregnation of a capillary tube with drop impact," *J. Colloid Interface Sci.*, vol. 341, no. 1, pp. 171–177, 2010.

[77] J. Xu, J. Xie, X. He, Y. Cheng, and Q. Liu, "Water drop impacts on a single-layer of mesh screen membrane: Effect of water hammer pressure and advancing contact angles," *Exp. Therm. Fluid Sci.*, vol. 82, pp. 83–93, 2017.

[78] S. Ryu, P. Sen, Y. Nam, and C. Lee, "Water Penetration through a Superhydrophobic Mesh during a Drop Impact," *Phys. Rev. Lett.*, vol. 118, no. 1, pp. 1–5, 2017.

[79] P. Brunet, F. Lapierre, F. Zoueshtiagh, V. Thomy, and A. Merlen, "To grate a liquid into tiny droplets by its impact on a hydrophobic microgrid," no. 1, pp. 94–96, 2009.

[80] A. Clarke, T. D. Blake, K. Carruthers, and A. Woodward, "Spreading and imbibition of liquid droplets on porous surfaces," *Langmuir*, vol. 18, no. 8, pp. 2980–2984, 2002.

[81] J. B. Lee, A. I. Radu, P. Vontobel, D. Derome, and J. Carmeliet, "Absorption of impinging water droplet in porous stones," *J. Colloid Interface Sci.*, vol. 471, pp. 59–70, 2016.

[82] G. Karapetsas, N. T. Chamakos, and A. G. Papathanasiou, "Efficient modelling of droplet dynamics on complex surfaces," *J. Phys. Condens.*

Matter, vol. 28, no. 8, 2016.

[83] P. D. Hicks and R. Purvis, “Gas-cushioned droplet impacts with a thin layer of porous media,” *J. Eng. Math.*, vol. 102, no. 1, pp. 65–87, 2017.

[84] M. Choi, G. Son, and W. Shim, “A level-set method for droplet impact and penetration into a porous medium,” *Comput. Fluids*, vol. 145, pp. 153–166, 2017.

[85] S. Derler and L. C. Gerhardt, “Tribology of skin: Review and analysis of experimental results for the friction coefficient of human skin,” *Tribol. Lett.*, vol. 45, no. 1, pp. 1–27, 2012.

[86] A. E. Kovalev, K. Dening, B. N. J. Persson, and S. N. Gorb, “Surface topography and contact mechanics of dry and wet human skin,” *Beilstein J. Nanotechnol.*, vol. 5, no. 1, pp. 1341–1348, 2014.

[87] V. Aguilella, K. Kontturi, L. Murtomaki, and P. Ramíres, “Estimation of the pore size and charge density in human cadaver skin,” *J. Control. …*, vol. 32, pp. 249–257, 1994.

[88] S. I. Alekseev, I. Szabo, and M. C. Ziskin, “Millimeter wave reflectivity used for measurement of skin hydration with different moisturizers,” *Ski. Res. Technol.*, vol. 14, no. 4, pp. 390–396, 2008.

[89] G. E. Flaten, Z. Palac, A. Engesland, J. Filipović-Grčić, Ž. Vanić, and N. Škalko-Basnet, “In vitro skin models as a tool in optimization of drug formulation,” *Eur. J. Pharm. Sci.*, vol. 75, pp. 10–24, 2015.

[90] B. O. M. I. LEE, S. AN, S.-Y. KIM, H. J. O. O. HAN, Y.-J. JEONG, K.-R. LEE, N. A. M. K. ROH, K. Y. U. J. AHN, I.-S. AN, and H. W. A. J. U. N. CHA, “Topical application of a cleanser containing extracts of Diospyros kaki folium, Polygonum cuspidatum and Castanea crenata var. dulcis reduces skin oil content and pore size in human skin.,” *Biomed. Reports*, vol. 3, no. 3, pp. 343–346, 2015.

[91] T. Goswami, B. R. Jasti, and X. Li, “Estimation of the theoretical pore sizes of the porcine oral mucosa for permeation of hydrophilic permeants,” *Arch. Oral Biol.*, vol. 54, no. 6, pp. 577–582, 2009.

[92] J. B. Lee, S. Dos Santos, and C. Antonini, “Water Touch-and-Bounce from a Soft Viscoelastic Substrate: Wetting, Dewetting, and Rebound on Bitumen,” *Langmuir*, vol. 32, no. 32, pp. 8245–8254, 2016.

[93] P. B. Weisensee, J. Tian, N. Miljkovic, and W. P. King, “Water droplet

impact on elastic superhydrophobic surfaces," *Sci. Rep.*, vol. 6, no. March, pp. 1–9, 2016.

[94] J. Dias, V. F. Diakonis, M. Lorenzo, F. Gonzalez, K. Porras, S. Douglas, M. Avila, S. H. Yoo, and N. M. Ziebarth, "Corneal stromal elasticity and viscoelasticity assessed by atomic force microscopy after different cross linking protocols," *Exp. Eye Res.*, vol. 138, pp. 1–5, 2015.

[95] M. Matsusaki, K. Fujimoto, Y. Shirakata, S. Hirakawa, K. Hashimoto, and M. Akashi, "Development of full-thickness human skin equivalents with blood and lymph-like capillary networks by cell coating technology," *Ski. Permeat. Dispos. Ther. Cosmeceutical Compd.*, pp. 345–362, 2017.

[96] K. P. Prashanth and H. G. Hanumantharaju, "Characterization and Analysis of Polymers Used as Artificial Skin," *Mater. Today Proc.*, vol. 5, no. 1, pp. 2488–2495, 2018.

[97] F. H. Zulkifli, F. S. J. Hussain, S. S. Zeyohannes, M. S. B. A. Rasad, and M. M. Yusuff, "A facile synthesis method of hydroxyethyl cellulose-silver nanoparticle scaffolds for skin tissue engineering applications," *Mater. Sci. Eng. C*, vol. 79, pp. 151–160, 2017.

[98] X. Zhang, C. Jia, X. Qiao, T. Liu, and K. Sun, "Silk fibroin microfibers and chitosan modified poly (glycerol sebacate) composite scaffolds for skin tissue engineering," *Polym. Test.*, vol. 62, pp. 88–95, 2017.

[99] L. Zhao, Y. Wu, S. Chen, and T. Xing, "Preparation and characterization of cross-linked carboxymethyl chitin porous membrane scaffold for biomedical applications," *Carbohydr. Polym.*, vol. 126, pp. 150–155, 2015.

[100] S. P. Lake, S. Ray, A. M. Zihni, D. M. Thompson, J. Gluckstein, and C. R. Deeken, "Pore size and pore shape - but not mesh density - alter the mechanical strength of tissue ingrowth and host tissue response to synthetic mesh materials in a porcine model of ventral hernia repair," *J. Mech. Behav. Biomed. Mater.*, vol. 42, pp. 186–197, 2015.

[101] D. Sivakumar, K. Katagiri, T. Sato, and H. Nishiyama, "Spreading behavior of an impacting drop on a structured rough surface," *Phys. Fluids*, vol. 17, no. 10, 2005.